2004

Morphological evolution and instabilities of solid thin films and wires

Wanxi Kan
Louisiana State University and Agricultural and Mechanical College

MORPHOLOGICAL EVOLUTION AND INSTABILITIES OF SOLID THIN FILMS AND WIRES

A Dissertation

Submitted to the Graduate Faculty of the
Louisiana State University and
Agriculture and Mechanical College
in partial fulfillment of the
requirements for the degree of
Doctor of Philosophy

In

The Interdepartmental Program
In Engineering Science

by
Wanxi Kan
B. S., University of Science and Technology Beijing, 1997
M. S., University of Science and Technology Beijing, 2000
December, 2004

ACKNOWLEDGMENTS

The author would like to thank his major professor Dr. Harris Wong, for his devoted guidance, continuous encouragement, and constructive suggestions throughout the research and preparation of this thesis.

The author particularly likes to thank Dr. Pratul K. Ajmera, Dr. Glenn Sinclair and Dr. John M. Tyler for their time and energy to serve on his examination committee. The author also wishes to acknowledge his office mates Donghong Min, Qingfang Wu ,Tinghui Xin and Jin Zhang for their helpful discussions.

TABLE OF CONTENTS

CHAPTER 1. INTRODUCTION

A solid thin film is built up on a substrate either directly by a physical process or through a chemical or electrochemical reaction. Thin films formed by different materials are extensively used in electronic and opto-electronic industries [1]. For example, semiconductor devices such as transistors or solid-state lasers are produced by growing thin films on semiconductor substrates. Lasers are made by sandwitching films between different semiconductor layers. The thickness of thin films usually ranges from 1 nanometer to 1 micron.

Since thin films have large surface-to-volume ratio and non-equilibrium micro-structure, they have unique properties which are significant different from the bulk material of the same kind. Thin film technology plays a very important role in the evolution of integrated circuits and opto-electronics. To improve the manufacturing process of solid film products for microelectronic devices, it is essential to understand the micro-structure and the stability of thin films at micro-scale.

Solid-state diffusion between thin films occurs in many industrial applications. For example, the assembly of micro electronic devices is often heated to high temperatures during the process of electronic materials, so atoms in a film will diffuse into adjacent films. Such interdiffusion is undesirable because it can destroy the function of the microelectronic device. This kind of interdiffusion can be prevented by interposing a barrier layer of a different material to separate the original films so that the intermixing of the original films is suppressed [1,2].

Therefore, to properly choose a diffusion barrier, it is important to predict the transport rate of atoms in the original films to cross the barrier layer. Solid-state diffusion also plays a very important role in the synthesis of materials from multilayer thin films of alternating components. Such multilayer films provide a large interfacial area to facilitate interfacial reactions. Multilayers have also been used to synthesize high temperature materials by solid-state reactions [3, 4]. The atoms in multilayers diffuse and react at moderate temperature to form compounds which can withstand high temperatures. In such applications, the synthesis rate depends on the interdiffusion of atoms between thin films, so the rate of interdiffusion needs to be analyzed.

Uniform films which are used in microelectronic and opto-electronic devices do not extend indefinitely but terminate at boundaries. A uniform film of infinite extent is at a local minimum of surface energy and is stable to infinitesimal disturbances [5]. However, the surface free energy of a bounded uniform film is not minimal. It will tend to alter its morphology to minimize the surface free energy [6]. The morphology evolution starts from the boundary of the thin film. The evolution is driven by capillarity and carried out by surface diffusion. After the diffusion takes place, the solid thin film will change shape and become discontinuous, which lead to malfunctioning of microelectronic and opto-electronic devices. As the size of the sold film products decreases, this boundary induced morphological evolution becomes more important.

Our interests of solid thin films lie in two aspect: the diffusion controlled growth of multi-layer compound in thin-film binary diffusion couples which is

discussed in Chapter 2 and the boundary induced instability of solid thin film which are presented in Chapter 3.

Solid thin wires appear often in integrated circuit technology. For example, electrical connections between circuit elements are made by thin metal films patterned into micron-wide wires. Further development of integrated circuit technology needs reduction of the size of thin wires. As a wire becomes smaller, the surface to volume ratio is higher and the capillary force stronger. Since the same surface displacement has more effect on the structural integrity of a smaller wire, morphological evolution and instability of thin wires are becoming more important. To improve the manufacturing process of solid wire products for microelectronic devices, it is very important to make clear the micro-structure and the stability of thin wires at micro-scale. We are interested in solid thin wires' instability at temperatures lower than the melting temperature. This is studied in Chapter 4.

Nanowires with radius down to 1 nm have been formed in a scanning tunneling microscope and studied by a high resolution electron microscope [7]. Their mechanical, thermal, optical and electrical properties have been extensively investigated due to interests in low dimensional physics and applications in nano-technology [8-16]. Our interest in nanowires lies in their instability which are studied by a classical molecular simulation method and presented in Chapter 5. This dissertation is concluded in Chapter 6.

CHAPTER 2. SELF-SIMILAR GROWTH OF MULTIPLE COMPOUND LAYERS IN BINARY DIFFUSION COUPLES WITH APPLICATION TO THE "MULTI-FOIL" METHOD

2.1. Introduction

When material A is in contact with material B at high temperature, atoms of A can diffuse into B and vice versa to form compound phases at the interface. This interdiffusion may be desirable, as in the synthesis of materials using multiplayer thin films [4, 18, 19, 20, 21], or undesirable, as in the manufacturing of micro electronic devices where interdiffusion between thin films can damage their functions and is prevented by diffusion barriers [1, 2]. In either case, it is important to predict the growth rate of compound phases. Diffusion-controlled growth is commonly studied using binary diffusion couples. An end member of predetermined composition is brought in contact with another end member of different composition, and interdiffusion is promoted by heating. In general, several compound phases form and grow with time. By measuring the thickness of the compound layers as functions of time and the concentration profiles within the layers, the diffusion coefficients can be inferred [23].

Recently, Zhang and Wong [17] studied the diffusion-controlled growth of a single compound phase $A_{n_1}B$ between material A and B with the nonlinear Kirkendall effect included. The nonlinear, time-dependent diffusion equation with two free boundaries is reduced by a self-similar transformation to a nonlinear ordinary differential equation, which is solved numerically. They found that the intrinsic diffusion coefficients of A and B in $A_{n_1}B$ can be determined from the

positions of the interfaces without using the concentration profile. Therefore, their proposed method of measuring intrinsic diffusion coefficients is simpler.

This chapter extends Zhang and Wong's analysis to arbitrary N compound layers. At time t = 0, material A and B come into contact (Figure 2.1(a)). At t > 0, N product layers form between A and B by interdiffusion. Figure 2.1(b) shows the situation of two compound layers $A_{n_1}B$ and $A_{n_2}B$. It is assumed that at the interfaces the concentrations are constant and follow the equilibrium values. The thickness of compound-layer $A_{n_1}B$ and $A_{n_2}B$ grows with time as atoms of A and B diffuse into $A_{n_1}B$ and $A_{n_2}B$. Similar to the one-layer case, the interdiffusion coefficients depend on the concentrations because of the Kirkendall effect. Thus, the diffusion equations are nonlinear. These equations are coupled through the interfaces, the locations of which are unknown. Hence, this is a free-boundary problem and the boundary locations must be determined as part of the solution. Although multi-phase diffusional growth has been studied extensively [23, 24, 25, 26, 27, 28], this coupled, nonlinear, free-boundary problem does not seem to have been solved.

One of the commonly used techniques for studying diffusion-controlled growth of compound phases is the "multi-foil" method [29, 30, 31, 32]. In this method, a binary diffusion couple is formed with each end member composed of several foils. Inert markers are inserted between the foils. Upon heating at a temperature of interest, the markers move following the Kirkendall velocity. The displacement of the markers is measured as a function of initial marker position.

From the displacement curve, the intrinsic diffusion coefficients can be inferred by comparison with a model.

Previous models of the “multi-foil” method do not solve the nonlinear diffusion equation, and thus require additional information beside the displacement curve. For example, van Dal et al [32] presented an expression for the ratio of the intrinsic diffusion coefficients that depends on the Kirkendall velocity, the concentration gradient, and the interdiffusion coefficient. The Kirkendall velocity can be determined from the displacement curve. However, the concentration gradient and the interdiffusion coefficient must be found by other measurements.

Zhang and Wong [17] derived an asymptotic solution of the nonlinear diffusion equation in the limit of zero composition variation. Their analytic solution can determine the intrinsic diffusion coefficients from only the displacement curve. In fact, only two points on the displacement curve are needed, as shown in section 2.7.

This chapter is organized as follows. The governing equations and boundary conditions for two product phases are presented in section 2.2. The partial differential equations are reduced to ordinary differential equations by a self-similar transformation (section 2.3). These equations are solved by a shooting method. The solutions are verified in two special cases and presented in section 2.4. Two applications of the two-layer solutions can be found in section 2.5. In section 2.6, the analysis is extended to N-compound layers. In section 2.7, the asymptotic solution of Zhang and Wong is applied to the “multi-foil” diffusion

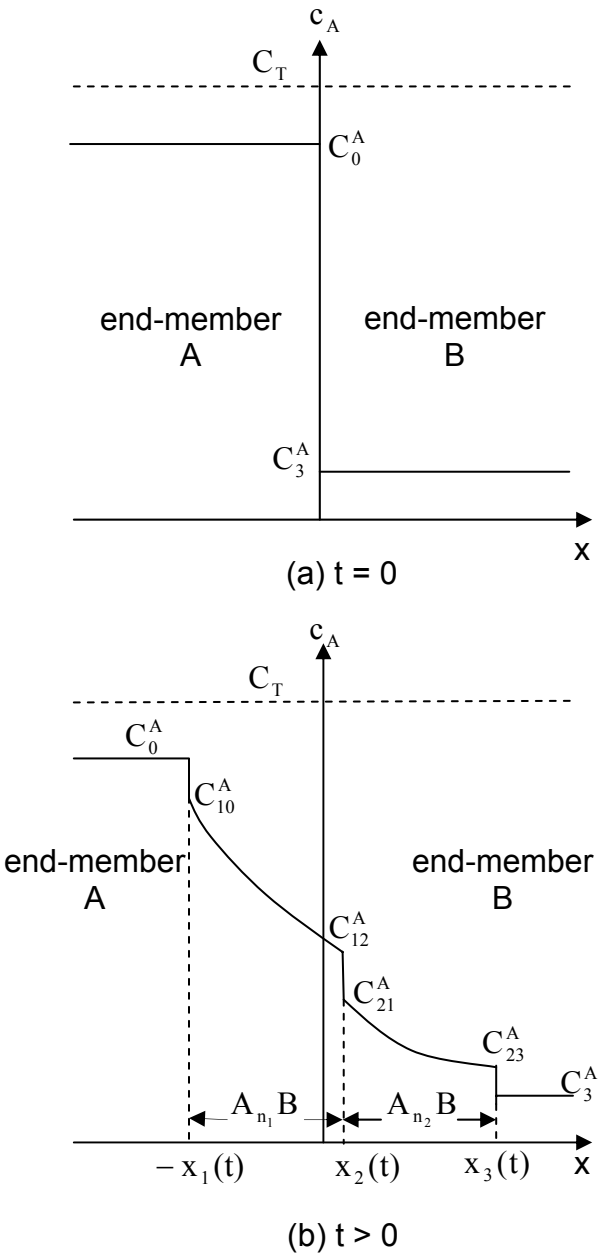

Fig. 2.1. Concentration of A versus position at time t = 0 (a) and t > 0 (b). Initially, end-member A at concentration C_0^A is saturated with B, and end-member B is saturated with A at concentration C_3^A. At t > 0, two compound layers $A_{n_1}B$ and $A_{n_2}B$ form and are bounded by three interfaces at $x = -x_1$, x_2, and x_3. The interfacial concentrations C_{10}^A, C_{12}^A, C_{21}^A, and C_{23}^A follow the equilibrium values.

couple technique. We discuss the implications in section 2.8 and conclude this work in section 2.9.

2.2. Formulation of the Two-layer

Figure 2.1 illustrates the physical situation. A binary diffusion couple is formed by bringing an end member of material A in contact with another end member of material B at time t = 0. At time t > 0, two compound phases $A_{n_1}B$ and $A_{n_2}B$ form between A and B. The concentration c_A of A in $A_{n_1}B$ obeys [1, 17, 33]

$$\frac{\partial c_A}{\partial t} = \frac{\partial}{\partial x}\{[\frac{c_A}{c_T}(D_{B1} - D_{A1}) + D_{A1}]\frac{\partial c_A}{\partial x}\} \ . \qquad (2.1)$$

where c_T is the sum of concentrations of material A and B, D_{A1} and D_{B1} are, respectively, the intrinsic diffusion coefficients of A and B in layer $A_{n_1}B$. The nonlinearity in the equation comes from the Kirkendall effect, which requires that the total concentration be constant in the compound phases, i.e. $c_A + c_B = c_T$. Similarly, the concentration c_A of A in $A_{n_2}B$ is governed by

$$\frac{\partial c_A}{\partial t} = \frac{\partial}{\partial x}\{[\frac{c_A}{c_T}(D_{B2} - D_{A2}) + D_{A2}]\frac{\partial c_A}{\partial x}\}, \qquad (2.2)$$

where D_{A2} and D_{B2} are, respectively, the intrinsic diffusion coefficients of A and B in layer $A_{n_2}B$. At t > 0, the two compound layers are bounded by three interfaces at $x = -x_1(t)$, $x = x_2(t)$ and $x = x_3(t)$. Local equilibrium is assumed to hold at each interface so that c_A is known at the interfaces. Thus, at $x = -x_1(t)$,

$$c_A = C_{10}^A \qquad (2.3a)$$

$$\frac{\partial x_1(t)}{\partial t}(C_{10}^A - C_0^A) = [\frac{C_{10}^A}{c_T}(D_{B1} - D_{A1}) + D_{A1}]\frac{\partial c_A}{\partial x}] \ , \qquad (2.3b)$$

where C_0^A is the concentration of A in end member A which is different from c_T because of finite solubility of B. At the interface between $A_{n_1}B$ and $A_{n_2}B$,

$$c_A = C_{12}^A \qquad \text{at } x = x_{2-} \qquad (2.4a)$$

$$c_A = C_{21}^A \qquad \text{at } x = x_{2+} \qquad (2.4b)$$

$$\frac{\partial x_2(t)}{\partial t}(C_{21}^A - C_{12}^A) = [\frac{C_{12}^A}{c_T}(D_{B1} - D_{A1}) + D_{A1}]\frac{\partial c_A}{\partial x}\bigg|_{x_{2-}} - [\frac{C_{21}^A}{c_T}(D_{B2} - D_{A2}) + D_{A2}]\frac{\partial c_A}{\partial x}\bigg|_{x_{2+}} \ , \qquad (2.4c)$$

where x_{2-} and x_{2+} mean, respectively, the left and the right side of x_2. At $x = x_3(t)$,

$$c_A = C_{23}^A \qquad (2.5a)$$

$$\frac{\partial x_3(t)}{\partial t}(C_3^A - C_{23}^A) = [\frac{C_{23}^A}{c_T}(D_{B2} - D_{A2}) + D_{A2}]\frac{\partial c_A}{\partial x}] \ , \qquad (2.5b)$$

where C_3^A is the initial concentration of A in end member B. Here, the equilibrium concentrations C_0^A, C_{10}^A, C_{12}^A, C_{21}^A, C_{23}^A and C_3^A are found from an equilibrium phase diagram once $A_{n_1}B$ and $A_{n_2}B$ are specified. Equations (2.3b), (2.4c), (2.5b) describe local mass conservation at the interfaces; the left side of the equation is the mass flux generated by sweeping an interface through a concentration jump, whereas the right side is the sum of the Fickian and bulk (Kirkendall) fluxes.

2.3. Self-similar Transformation

Since equations (2.1) to (2.5) contain neither a length nor a time scale, a self-similar solution is sought. A set of self-similar variables is defined as follows:

$$y = \frac{x}{x_1(t)},\ c(y) = \frac{c_A(t,x)}{c_T}. \tag{2.6}$$

The diffusion equation in the $A_{n_1}B$ layer becomes

$$-yD_1\frac{dc}{dy} = \frac{d}{dy}\{[R_{A1} + c(1-R_{A1})]\frac{dc}{dy}\} \tag{2.7a}$$

$$D_1 = \frac{x_1}{D_{B1}}\frac{dx_1}{dt} \tag{2.7b}$$

$$R_{A1} = \frac{D_{A1}}{D_{B1}}\quad , \tag{2.7c}$$

where R_{A1} is a diffusivity ratio, and D_1 is the dimensionless parabolic rate constant for the interface at $x = -x_1(t)$. This rate constant can be viewed as a nondimensionalized effective diffusivity for the interface at x_1; it is an unknown constant that needs to be determined as part of the solution. The diffusion equation in the $A_{n_2}B$ layer becomes

$$-yD_1\frac{dc}{dy} = \frac{d}{dy}\{[R_{A2} + c(R_{B2} - R_{A2})]\frac{dc}{dy}\} \tag{2.8a}$$

$$R_{A2} = \frac{D_{A2}}{D_{B1}} \tag{2.8b}$$

$$R_{B2} = \frac{D_{B2}}{D_{B1}}, \tag{2.8c}$$

where R_{A2} and R_{B2} are diffusivity ratios. Boundary conditions (2.3), (2.4) and (2.5) are also transformed. At the interface between A and $A_{n_1}B$,

$$y = -1 \tag{2.9a}$$

$$c = C_{10} \tag{2.9b}$$

$$D_1(C_0 - C_{10}) = -[R_{A1} + C_{10}(1 - R_{A1})]\frac{dc}{dy}. \tag{2.9c}$$

At the interface between $A_{n_1}B$ and $A_{n_2}B$,

$$y = Y_2 \tag{2.10a}$$

$$c = C_{12} \qquad \text{at } y = Y_{2-} \tag{2.10b}$$

$$c = C_{21} \qquad \text{at } y = Y_{2+} \tag{2.10c}$$

$$Y_2 D_1(C_{21} - C_{12}) = [R_{A1} + C_{12}(1 - R_{A1})]\left.\frac{dc}{dy}\right|_{Y_{2-}} - [R_{A2} + C_{21}(R_{B2} - R_{A2})]\left.\frac{dc}{dy}\right|_{Y_{2+}}. \tag{2.10d}$$

Here Y_{2-} and Y_{2+} represent, respectively, the left and the right side of Y_2. At the interface between $A_{n_2}B$ and B,

$$y = Y_3 \tag{2.11a}$$

$$c = C_{23} \tag{2.11b}$$

$$Y_3 D_1(C_{23} - C_3) = -[R_{A2} + C_{23}(R_{B2} - R_{A2})]\frac{dc}{dy}. \tag{2.11c}$$

Here, C_0, C_{10}, C_{12}, C_{21}, C_{23} and C_3 are the equilibrium concentrations made dimensionless by c_T, and

$$Y_2 = \frac{x_2(t)}{x_1(t)} \qquad (2.12a)$$

$$Y_3 = \frac{x_3(t)}{x_1(t)} \qquad (2.12b)$$

are unknown constants to be determined.

2.4. Numerical Method and Results

A fourth order Runge-Kutta method is used to solve (2.7)-(2.11). Since D_1, Y_2 and Y_3 are unknown, an iteration procedure is adopted and outlined below. First, a value for D_1 is assumed. This allows (2.7) to be integrated from y = -1 with boundary condition (2.9) for c and dc/dy. The integration proceeds until $c = C_{12}$, at which point the integration is stopped and the position corresponds to $y = Y_2$. Subsequently, (2.8) is integrated from $y = Y_2$ using boundary condition (2.10) for c and dc/dy. The integration is stopped when $c = C_{23}$, and the position corresponds to $y = Y_3$. This value is substituted into (2.11c) to yield a new value for D_1 and the procedure is repeated until D_1 converges. A stepsize of 0.01 is used in the integration, and the results presented below are accurate to at least four significant figures.

The numerical method and the two-layer solutions are checked in two special cases. First, the equilibrium concentrations of A at the interfaces are taken to be skew-symmetrically distributed about the middle interface at $y = Y_2$: C_0 = 1, C_{10} = 0.9, C_{12} = 0.7, C_{21} = 0.3, C_{23} = 0.1, and C_3 = 0. In addition, the intrinsic diffusivities of A and B in $A_{n_1}B$ are assumed to be the same as those in $A_{n_2}B$:

$R_{A1} = R_{A2}$ and $R_{B2} = 1$. The computed concentration profile is found to be also skew-symmetric about $y = Y_2 = 0$ with $Y_3 = 1$.

In the second case, the equilibrium concentration of A is maintained continuous across the middle interface and the diffusivities are again set to be the same: $R_{A1} = R_{A2}$ and $R_{B2} = 1$. Thus, the two layers behave as one layer case. Results of c, D_1 and Y_3 agree with the one-layer solutions [17].

A particular case (C_0 = 0.9, C_{10} = 0.8, C_{12} = 0.55, C_{21} = 0.5, C_{23} = 0.45, C_3 = 0.35) is studied in detail to illustrate the general characteristics. Figure 2.2 shows the concentration profiles for $R_{A2} = R_{B2} = 1$ and R_{A1} = 0, 1, 10 and 100. As R_{A1} increases, the $A_{n_1}B$ layer grows much faster than the $A_{n_2}B$ layer. The largest value of $R_{A1} = 100$ yields almost zero thickness for the $A_{n_2}B$ layer. This effect is illustrated further by plotting the interfacial positions Y_2 and Y_3 as functions of R_{A1} for different R_{A2} (Figs. 2.3 and 2.4). For a given value of R_{A2}, both Y_2 and Y_3 approach the same constant value as $R_{A1} \to \infty$, although Y_2 approaches from below and Y_3 from above. This is shown most clearly for $R_{A2} = 0$ and 1. For $R_{A2} = 10$ or larger, R_{A1} needs to be larger than 100 to see the convergence. When Y_2 and Y_3 converge, the $A_{n_2}B$ layer vanishes. The suppression of a compound phase by another when the diffusivity ratio is large agrees with experimental observations [34]. Figure 2.3(a) also shows that Y_2 becomes negative for small R_{A1} and large R_{A2}. Under these conditions, the $A_{n_2}B$ layer

grows much faster than the $A_{n_1}B$ layer. Consequently, the middle interface moves left towards end-member A.

In Fig. 2.4, concentration profiles are plotted for the same interfacial concentrations, but R_{A2} is increased from 0 to 100, and $R_{A1} = R_{B2} = 1$. It shows that as R_{A2} increases, the $A_{n_2}B$ layer thickens at the expense of the $A_{n_1}B$ layer. Fig. 2.5 graphs the interfacial positions Y_2 and Y_3 as functions of R_{A2}. It reveals that as R_{A2} increases, Y_2 decreases from positive to negative and eventually tends to –1 as $R_{A2} \to \infty$, i.e., the $A_{n_1}B$ layer disappears. The position Y_3 always increases with R_{A2} for all R_{A1}. Thus, suppression of one layer by another is again observed.

The effective diffusivity D_1 of the left interface is plotted as functions of R_{A1} and R_{A2} in Fig. 2.6. If either R_{A1} or R_{A2} is fixed, then D_1 varies almost linearly with the other variable, but R_{A1} has a much larger effect on D_1 than R_{A2}.

2.5. Application of the Two-layer Solution

The two-layer self-similar solution can determine the intrinsic diffusion coefficients D_{A2} and D_{B2} (D_{A1} and D_{B1} are assumed known from the one-layer method described in Zhang and Wong [17]). First, two nondimensionalized effective diffusivities are defined for the interfaces at $x = x_2$ and $x = x_3$:

$$D_2 = \frac{x_2}{D_{B1}} \frac{dx_2}{dt} \tag{2.13}$$

$$D_3 = \frac{x_3}{D_{B1}} \frac{dx_3}{dt} \tag{2.14}$$

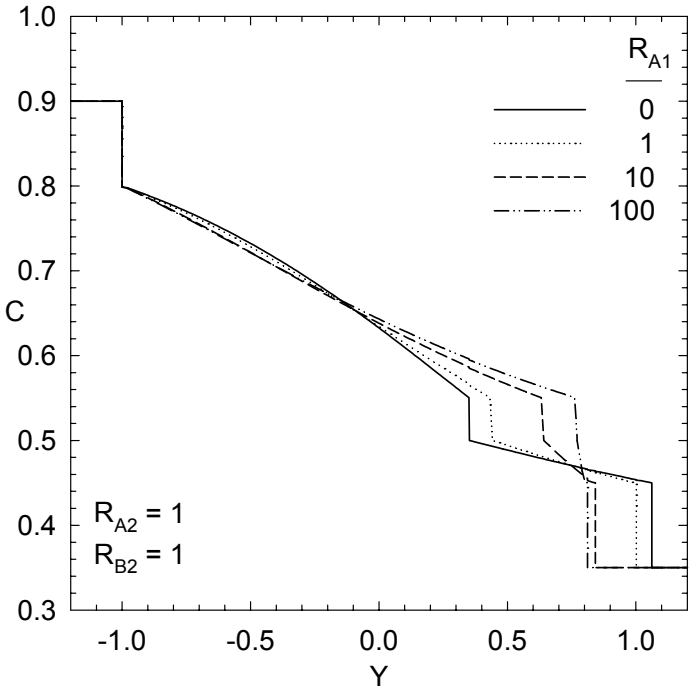

Fig. 2.2. Normalized concentration versus position for different diffusivity ratio R_{A1} with $R_{A2} = R_{B2} = 1$. The concentration profiles are calculated for a particular case: $C_0 = 0.9$, $C_{10} = 0.8$, $C_{12} = 0.55$, $C_{21} = 0.5$, $C_{23} = 0.45$, and $C_3 = 0.35$.

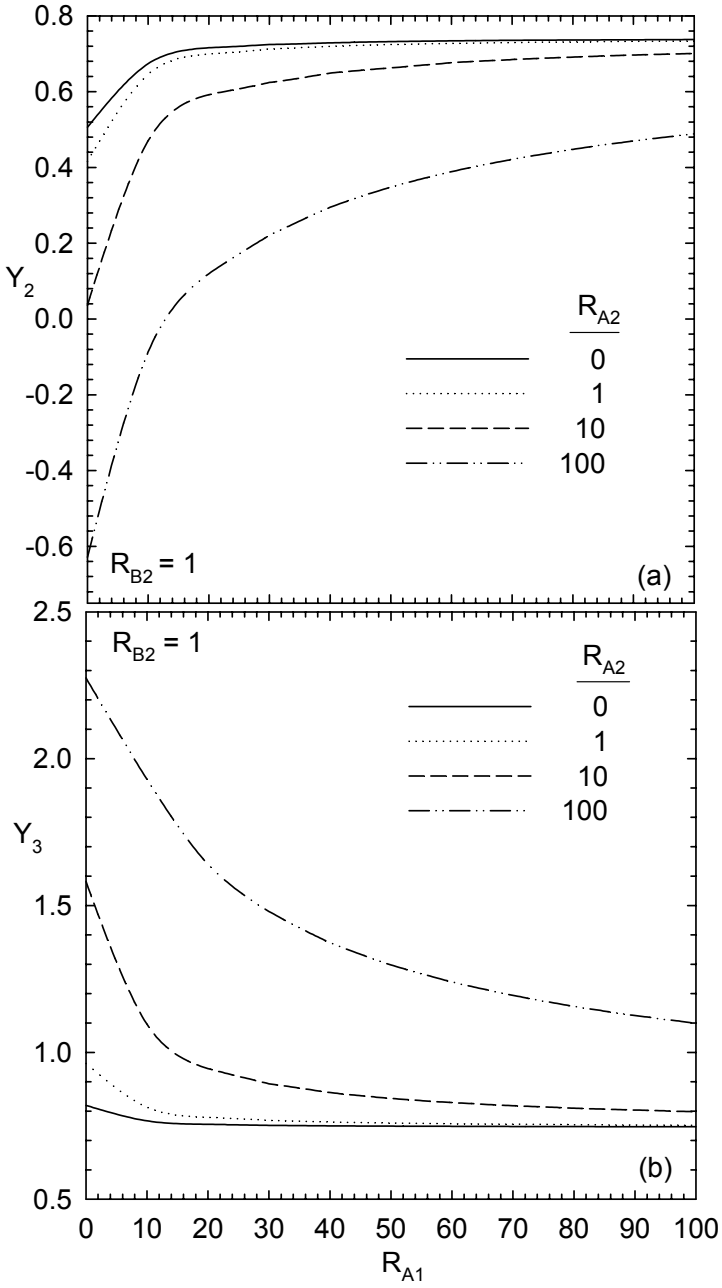

Fig. 2.3. Dimensionless position Y_2 of the middle interface (a) and Y_3 of the right interface (b) versus diffusivity ratio R_{A1} for different diffusivity ratio R_{A2} for the case in Fig. 2.2. $R_{B2} = 1$.

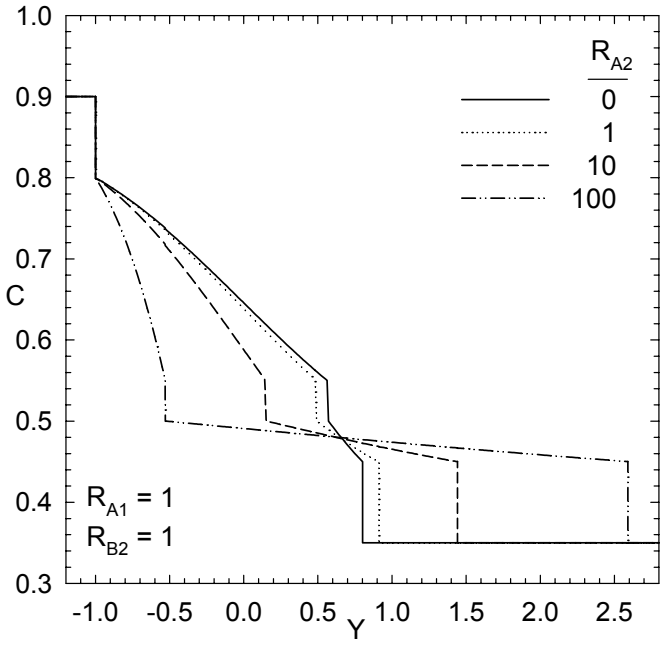

Fig. 2.4. Normalized concentration versus position for different diffusivity ratio R_{A2} with $R_{A1} = R_{B2} = 1$. The concentration profiles are calculated for the case in Fig. 2.2.

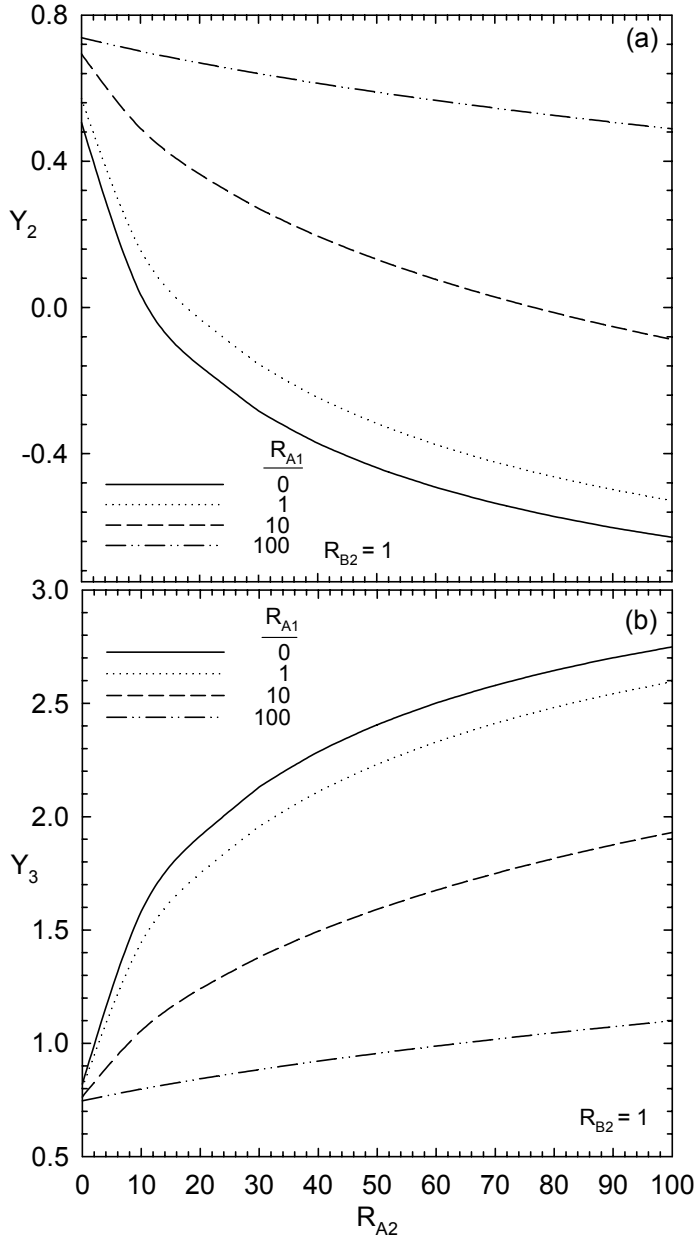

Fig. 2.5 Normalized position Y_2 of the middle interface (a) and Y_3 of the right interface (b) versus diffusivity ratio R_{A2} for different diffusivity ratio R_{A1} for the case in Fig. 2.2. $R_{B2} = 1$.

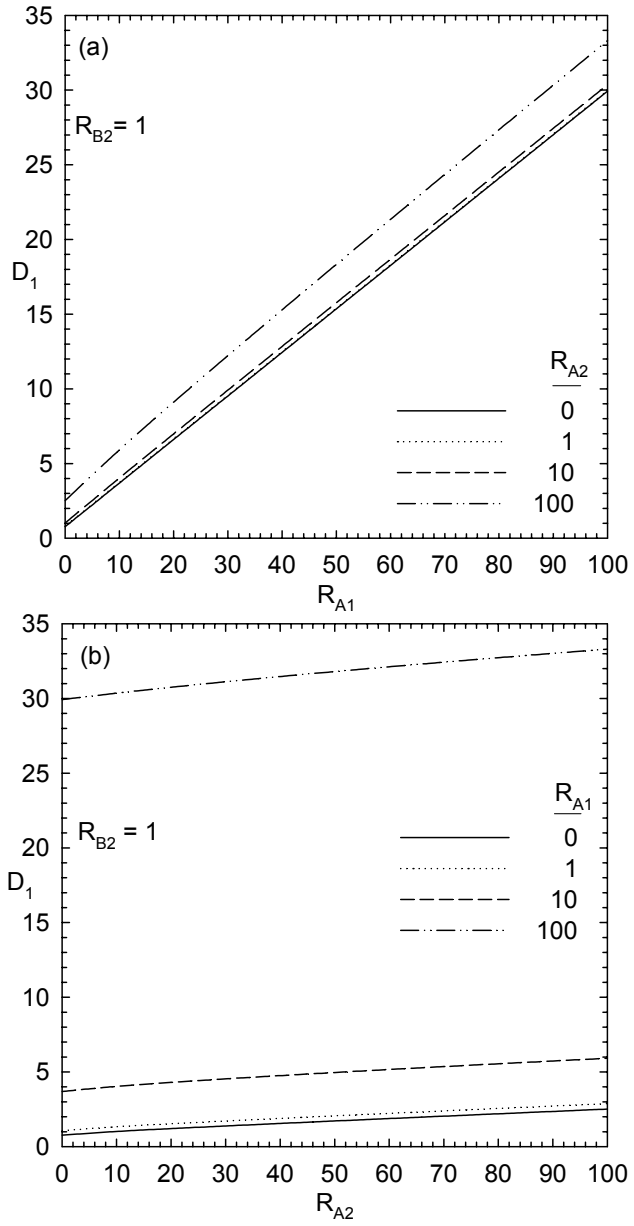

Fig. 2.6. (a). Effective diffusivity D_1 of the interface at $x = -x_1$ versus diffusivity ratio R_{A1} for different diffusivity ratio R_{A2} for the case in Fig. 2.2. (b) D_1 versus R_{A2} for different R_{A1}. $R_{B2} = 1$.

These can be expressed in terms of D_1 in (2.7b), and Y_2 and Y_3 in (2.12):

$$D_2 = Y_2^2 D_1 \tag{2.15}$$

$$D_3 = Y_3^2 D_1 \tag{2.16}$$

The interfacial positions $x_1(t)$, $x_2(t)$, and $x_3(t)$ can be solved from (2.7b), (2.13) and (2.14) with the initial condition that $x_1 = x_2 = x_3 = 0$ at t = 0:

$$x_1 = (2D_1 D_{B1} t)^{1/2} \tag{2.17}$$

$$x_2 = (2D_2 D_{B1} t)^{1/2} \tag{2.18}$$

$$x_3 = (2D_3 D_{B1} t)^{1/2} \quad . \tag{2.19}$$

According to (2.13) and (2.14),

$$\frac{x_2}{x_1} = \left(\frac{D_2}{D_1}\right)^{1/2} = Y_2 \tag{2.20}$$

$$\frac{x_3}{x_1} = \left(\frac{D_3}{D_1}\right)^{1/2} = Y_3 \tag{2.21}$$

In an experiment with a binary diffusion couple that yields two product layers, the interfacial positions x_1, x_2, and x_3 can be measured as functions of time. The interfacial position $x_1(t)$ determines D_1 from (2.17) as D_{B1} is assumed given. The ratios x_2/x_1 and x_3/x_1 give Y_2 and Y_3, denoted by $\overline{Y}_2$ and $\overline{Y}_3$ respectively. The equilibrium phase diagram of the binary alloy fixes C_0, C_{10}, C_{12}, C_{21}, C_{23}, and C_3. Thus, the only unknowns are D_{A2} and D_{B2} or $R_{A2}(= D_{A2}/D_{B1})$ and $R_{B2}(= D_{B2}/D_{B1})$. The self-similar model uses the interfacial concentrations and the diffusivity ratios R_{A1}, R_{A2}, and R_{B2} as inputs to find D_1, Y_2 and Y_3. In the

experiment, all the variables are known except R_{A2} and R_{B2}. The self-similar model finds R_{A2} and R_{B2} by the following iterative scheme. First, assume a set of values for R_{A2} and R_{B2}. Thus, the self-similar model has sufficient inputs to calculate Y_2 and Y_3, which are different from $\overline{Y}_2$ and $\overline{Y}_3$. By adjusting R_{A2} and R_{B2}, Y_2 can be made to approach $\overline{Y}_2$ and Y_3 to $\overline{Y}_3$. After R_2 and R_{B2} have converged, the intrinsic diffusivities are found as

$$D_{A2} = D_{B1} R_{A2} \tag{2.22}$$

$$D_{B2} = D_{B1} R_{B2} \ . \tag{2.23}$$

The particular case studied in the previous section is used to test this iterative scheme. The interfacial concentrations, R_{A1}, D_1, $\overline{Y}_2$, and $\overline{Y}_3$ are specified, and R_{A2} and R_{B2} are found by a double-loop bisection method. Different values of R_{A1}, D_1, $\overline{Y}_2$, and $\overline{Y}_3$ are tried, and R_{A2} and R_{B2} always converge to the correct solutions. Thus, the method of finding intrinsic diffusivities from only the positions of interfaces can be extended to two layers.

Previous experimental studies seldom measure the interfacial positions. Instead, they report the thickness of the compound layers as a function of time. Thus, there is insufficient information to infer the intrinsic diffusivities using the above method. However, in some rare cases, the concentration in the layers is shown. In what follows, we attempt to use this extra information to extract the intrinsic diffusivities.

The γ and ε phases of Ag-Zn alloys have been studied by Williams et al. An Ag-Zn binary diffusion couple can form five equilibrium phases. Williams et al.

fabricated alloy ingots with different compositions and used them as end members of diffusion couples. In one experiment ($\beta-\eta-16$), an end member with the β-phase composition is combined with another with the η-phase composition. Under heating at 400 °C, the thickness of the intermediate γ and ε phases is measured as a function of time. They found that the layer thickness varies as $t^{1/2}$, implying that the growth is controlled by diffusion. At t = 129600 s, the thickness of the γ phase is $\Delta x^{\gamma} = 450\mu m$ and that of the ε phase is $\Delta x^{\varepsilon} = 515\mu m$. The ratio is $r = \Delta x^{\varepsilon}/\Delta x^{\gamma} = 1.14$. Williams et al also plotted the concentrations in the γ and ε phases at a particular time. The data are replotted in Fig. 2.7. To use this information, we vary R_{A1}, R_{A2}, and R_{B2} in the self-similar calculation to generate a concentration profile that is closest to the experimented data, subject to the constraint that $r = (Y_2 + 1)/(Y_3 - Y_2) = 1.14$.

As shown in Fig. 2.7, the measured concentration in the ε-phase is almost horizontal near Y = -1, and becomes almost vertical at the middle interface. We vary R_{A1}, R_{A2}, and R_{B2} to reduce the magnitude of the concentration gradient at Y = -1. This fixes R_{A1} = 0, but a range of R_{A2} and R_{B2} give similar values for the concentration gradient at Y = -1. The two extreme cases are plotted in Fig. 2.7. In one extreme, $R_{A2} = 0$ and $R_{B2} = 5.78$. This gives $D_1 = 0.746$, $Y_2 = 0.403$, $Y_3 = 1.64$. For the other extreme, $R_{A2} = 5.37$ and $R_{B2} = 0$. In this case, $D_1 = 0.749$, $Y_2 = 0.396$, $Y_3 = 1.63$. Thus, both extremes yield similar values for $D_1(=0.75)$, $Y_2(=0.40)$, and $Y_3(=1.6)$. We can find one intrinsic diffusivity from these values. The ε-phase thickness is

$$\Delta x^{\varepsilon} = x_2 - (-x_1) = (2D_2 D_{B1} t)^{1/2} + (2D_1 D_{B1} t)^{1/2} \quad . \tag{2.24}$$

This gives

$$D_{B1} = \frac{(\Delta x^{\varepsilon})^2}{2(1+Y_2)^2 D_1 t} \quad , \tag{2.25}$$

where D_2 has been replaced by $D_1 Y_2^2$ using (2.15). Substitution of the experimental values of Δx^{ε} and t, and the computed values of D_1 and Y_2 yields $D_{B1} = D_{Ag}^{\varepsilon} = 6.96 \times 10^{-13} m^2/s$. This intrinsic diffusivity does not seem to have been measured. However, Heumann [35] presented a measured value of $D_{Ag}^{\gamma}(400°C) = 1 \times 10^{-12} m^2/s$, which is reasonally close to the computed value. Other intrinsic diffusivities in the γ and ε phases cannot be determined except that $D_{Zn}^{\varepsilon} << D_{Ag}^{\varepsilon}$.

2.6. Extension to N Compound Layers

The two-layer self-similar solution can be extended to N compound layers. The governing equation for the i^{th} layer ($A_{n_i}B$) is

$$\frac{\partial c_A}{\partial t} = \frac{\partial}{\partial x}\{[\frac{c_A}{c_T}(D_{Bi} - D_{Ai}) + D_{Ai}]\frac{\partial c_A}{\partial x}\} \quad , \quad i=1, 2, \ldots, N \quad , \tag{2.26}$$

where D_{Ai} and D_{Bi} are the intrinsic diffusion coefficient of A and B in the i^{th} layer. The boundary conditions at $x = x_1(t)$ in (2.3) still hold. In general, at $x = x_i(t)$, i = 2, 3,…, N,

$$c_A = C_{(i-1)i}^{A} \qquad \text{at } x = x_{i-} \tag{2.27a}$$

$$c_A = C_{i(i-1)}^{A} \qquad \text{at } x = x_{i+} \tag{2.27b}$$

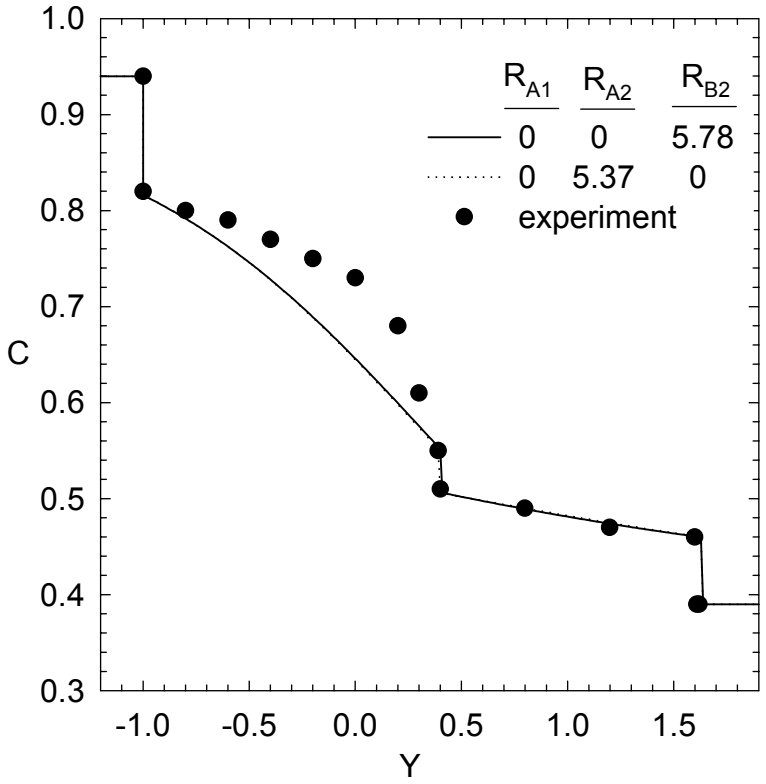

Fig. 2.7. Normalized concentration versus distance in the γ and ε phases of the Ag-Zn alloy at 400 °C. The experimental data are taken from Williams et al. The interfacial concentrations come from the equilibrium phase diagram: $C_0 = 0.936$, $C_{10} = 0.816$, $C_{12} = 0.551$, $C_{21} = 0.506$, $C_{23} = 0.460$ and $C_3 = 0.390$. Two computed concentration profiles with different R_{A2} and R_{B2} are almost indistinguishable.

$$\frac{\partial x_i(t)}{\partial t}(C^A_{(i-1)i} - C^A_{i(i-1)}) = [\frac{C^A_{i(i-1)}}{c_T}(D_{Bi} - D_{Ai}) + D_{Ai}]\frac{\partial c_A}{\partial x}\bigg|_{x_{i+}} - [\frac{C^A_{(i-1)i}}{c_T}(D_{B(i-1)} - D_{A(i-1)}) + D_{A(i-1)}]\frac{\partial c_A}{\partial x}\bigg|_{x_{i-}}, \quad (2.27c)$$

where x_{i-} and x_{i+} mean, respectively, the left and the right side of x_i. At the right-most interface, $x = x_{N+1}(t)$,

$$c_A = C^A_{N(N+1)} \quad (2.28a)$$

$$\frac{\partial x_{N+1}(t)}{\partial t}(C^A_{N+1} - C^A_{N(N+1)}) = [\frac{C^A_{N(N+1)}}{c_T}(D_{BN} - D_{AN}) + D_{AN}]\frac{\partial c_A}{\partial x}] \quad (2.28b)$$

This completes the formulation of the N-layer problem.

The same self-similar transformation is used:

$$y = \frac{x}{x_1(t)},\ c(y) = \frac{c_A(t,x)}{c_T} \quad (2.29)$$

The governing equation for the i^{th} layer ($A_{n_i}B$, i=1, …, N) becomes

$$-yD_1\frac{dc}{dy} = \frac{d}{dy}\{[R_{Ai} + c(R_{B2} - R_{A2})]\frac{dc}{dy}\} \quad (2.30a)$$

$$R_{Ai} = \frac{D_{Ai}}{D_{B1}} \quad (2.30b)$$

$$R_{Bi} = \frac{D_{Bi}}{D_{B1}}, \quad (2.30c)$$

where R_{Ai} and R_{Bi} are the diffusivity ratios. At the interface between A and $A_{n_1}B$, the boundary conditions in (2.9) remain valid. At the interface between the $(i-1)^{th}$ and the i^{th} layer:

$$y = Y_i \quad (2.31a)$$

$$c = C_{(i-1)i} \qquad (y = Y_{i-}) \tag{2.31b}$$

$$c_i = C_{i(i-1)} \qquad (y = Y_{i+}) \tag{2.31c}$$

$$Y_i D_1 (C_{i(i-1)} - C_{(i-1)i}) = [R_{A(i-1)} + C_{(i-1)i}(R_{B(i-1)} - R_{A(i-1)})]\left.\frac{dc}{dy}\right|_{Y_{i-}} - [R_{Ai} + C_{i(i-1)}(R_{Bi} - R_{Ai})]\left.\frac{dc}{dy}\right|_{Y_{i+}} \tag{2.31d}$$

where Y_{i-} and Y_{i+} denote, respectively, the left and the right side of Y_i. At the right-most interface between the N^{th} layer and B,

$$y = Y_{N+1} \tag{2.32a}$$

$$c = C_{N(N+1)} \tag{2.32b}$$

$$Y_{N+1} D_1 (C_{N(N+1)} - C_{N+1}) = -[R_{AN} + C_{N(N+1)}(R_{BN} - R_{AN})]\frac{dc}{dy} \quad . \tag{2.32c}$$

Here, $Y_i = x_i(t)/x_1(t)$, i=2, …, N+1, are unknown constants to be determined.

The same fourth order Runge-Kutta method is used to solve the N-compound layer problem. The procedure is similar to that of the two-layer case. (The computer program is listed in Appendix F.) As an example, we compute the concentration in the β, γ, and ε phases of the Ag-Zn alloy at 400 °C. At this temperature, $D_{Zn}^{\beta} = 1\times10^{-11}\,m^2/s$, $D_{Ag}^{\beta} = 2\times10^{-12}\,m^2/s$, $D_{Zn}^{\gamma} = 4\times10^{-12}\,m^2/s$, and $D_{Ag}^{\gamma} = 1\times10^{-12}\,m^2/s$ [35]. In section 2.5, the self-similar model predicts $D_{Ag}^{\varepsilon} = 6.96\times10^{-13}\,m^2/s$ and $D_{Zn}^{\varepsilon} << D_{Ag}^{\varepsilon}$. Therefore, $R_{A1} = D_{Zn}^{\varepsilon}/D_{Ag}^{\varepsilon} = 0$, $R_{A2} = D_{Zn}^{\gamma}/D_{Ag}^{\varepsilon} = 5.75$, $R_{B2} = D_{Ag}^{\gamma}/D_{Ag}^{\varepsilon} = 1.44$, $R_{A3} = D_{Zn}^{\beta}/D_{Ag}^{\varepsilon} = 14.4$, $R_{B3} = D_{Ag}^{\beta}/D_{Ag}^{\varepsilon} = 2.86$. The computed concentration profile is plotted in Fig. 2.8 for this set of parameters.

2.7. Application to the "Multi-foil" Method

In the "multi-foil" method, markers are planted in a diffusion couple at different distances from the initial interface at time t = 0. Under heating at a temperature of interest, a compound layer grows and moves the markers inside the layer by the Kirkendall effect. At time t, the diffusion is stopped and the displacement of the markers from their initial positions is measured as a function of the initial marker position. The displacement curve is used to calculate the intrinsic diffusion coefficients.

An analytic solution for the displacement curve can be found in the limit of zero concentration gradient. As a compound layer grows, the markers inside move following the Kirkendall velocity v [1, 33]:

$$v = \frac{(D_{A1} - D_{B1})}{c_T} \frac{dc_A}{dx} \quad , \tag{2.33}$$

which can be transformed in terms of the self-similar variables defined in (2.6) as

$$v = \frac{(D_{A1} - D_{B1})}{(2D_1 D_{B1} t)^{1/2}} \frac{dc}{dy} \quad . \tag{2.34}$$

The position of a marker is measured by x, which is related to the velocity of the maker by

$$v = \frac{dx}{dt} \tag{2.35}$$

Let x_0 be the initial position of the marker, and $z = x - x_0$ be the displacement of the marker from the initial position. The objective is to find $z = z(t, x_0)$.

An asymptotic solution has been derived in the limit of zero concentration gradient for the one-layer case [17], i.e. in the limit $C_{10} - C_{12} \to 0$ (Fig. 2.1). The

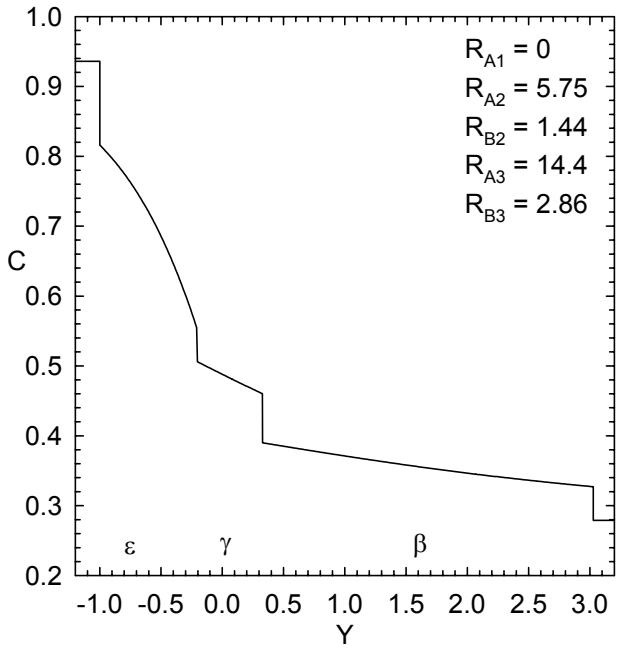

Fig. 2.8. Normalized concentration versus position in the β, γ, and ε phases of the Ag-Zn alloy. The interfacial concentrations are $C_0 = 0.936$, $C_{10} = 0.816$, $C_{12} = 0.551$, $C_{21} = 0.506$, $C_{23} = 0.460$, $C_{32} = 0.390$, $C_{34} = 0.327$, and $C_4 = 0.279$.

solution gives the concentration $c = c(y)$ as constant to the leading order, linear to the first order, and cubic to the second order. The first order linear profile is used here to demonstrate the calculation procedure. (Appendix A lists the second-order solution). The linear profile has a constant slope:

$$\frac{dc}{dy} = -\frac{(C_{10} - C_{21})(C_{10} - C_{12})}{(C_{01} - C_{21})} \quad . \tag{2.36}$$

Thus, the marker position x can be solved from (2.34), (2.35) and (2.36) as

$$x = x_0 - \frac{2(C_{10} - C_{21})(C_{10} - C_{12})(D_{A1} - D_{B1})}{(C_{01} - C_{21})(2D_1 D_{B1})^{1/2}}(t^{1/2} - t_0^{1/2}) \tag{2.37}$$

This equation holds for $t > t_0$, and describes the displacement x of a marker initially at position x_0. The marker begins to move at $t = t_0$. This means that an interface reaches the marker at $t = t_0$, because the marker cannot move if it is outside the growing phase. Thus, the initial position x_0 of the marker is related to t_0 by the interfacial positions. If $x_0 > 0$, then the right interface at $x_2 = (2D_2 D_{B1} t)^{1/2}$ reaches the marker, and $t_0^{1/2} = x_0 / (2D_2 D_{B1})^{1/2} = x_0 t^{1/2} / x_2$. If $x_0 < 0$, then the left interface at $-x_1 = -(2D_1 D_{B1} t)^{1/2}$ reaches the marker, and $t_0^{1/2} = -x_0 / (2D_1 D_{B1})^{1/2} = -x_0 t^{1/2} / x_1$. Thus, if $x_0 > 0$,

$$z = z_m (1 - \frac{x_0}{x_2}) \ , \tag{2.38a}$$

and if $x_0 < 0$,

$$z = z_m (1 + \frac{x_0}{x_1}) \ , \tag{2.38b}$$

where

$$z_m = \frac{2(C_{10} - C_{21})(C_{10} - C_{12})(D_{B1} - D_{A1})}{(C_{01} - C_{21})} \frac{t}{x_1}. \qquad (2.38c)$$

Thus, z_m has the same sign as (D_{B1}-D_{A1}). If $D_{B1} > D_{A1}$, then more B molecules will diffuse from B to A than A molecules from A to B (Fig. 2.1). This creates a net mass flux from B to A, which is balanced by a Kirkendall flux from A to B to maintain the same concentration at every point in the compound layer. The kirkendall flux will move the markers towards B and result in a positive z_m. Thus, the relation between z_m and (D_{B1}-D_{A1}) in (2.38c) makes physical sense. Fig. 2.9 plots the normalized displacement z/z_m versus x_2/x_1 in the β phase of a Ag-Zn couple at 400 °C with $C_0 = 0.460$, $C_{10} = 0.390$, $C_{12} = 0.327$, $C_{21} = 0.279$, and $R_{A1} = 5.0$ [17]. From these data, the self-similar model computes $x_2/x_1 = Y_2 = 0.395$. Thus, the first-order asymptotic solution yields two straight lines with the one on the right much steeper than that on the left.

Two vertex positions of the triangular displacement curve are sufficient to determine the intrinsic diffusivities D_{A1} and D_{B1}. Given an experimentally measured displacement curve, the vertice positions x_1, x_2, and z_m are known together with t, the time at which the displacement curve is recorded. If the interfacial positions x_1 and x_2 are chosen, then D_{A1} and D_{B1} are found by the method of Zhang and Wong [17]. If the peak height z_m and x_1 are chosen, then D_{A1} and D_{B1} are found from (2.17) and (2.38c) as follows. (The last case of choosing z_m and x_1 is basically the same.) The effective diffusivity D_1 in (2.17) has been shown to vary linearly with R_{A1} [17]:

$$D_1 = d_1 R_{A1} + d_0 , \tag{2.39}$$

where d_1 and d_0 depend only on the equilibrium interfacial concentrations. Eliminating D_1 in (2.17) leads to

$$d_1 D_{A1} + d_0 D_{B1} = \frac{x_1^2}{2t} . \tag{2.40}$$

This equation together with (2.38b) yields

$$D_{A1} = \frac{x_1}{2t(d_0 + d_1)}[x_1 + \frac{(C_0 - C_{21}) d_0 z_m}{(C_{10} - C_{21})(C_{10} - C_{12})} \tag{2.41a}$$

$$D_{B1} = D_{A1} - \frac{(C_0 - C_{21}) x_1 z_m}{2t(C_{10} - C_{21})(C_{10} - C_{12})} . \tag{2.41b}$$

Which are accurate to order $(C_{10} - C_{12}) x_1 z_m / t$. This error comes from the expression of z_m in (2.38c), as shown by the second-order asymptotic solution in Appendix A. Since the relation in (2.39) is exact, d_0 and d_1 should be calculated numerically to avoid any unnecessary errors [17]. If a quick estimate is needed, the following asymptotic solution may be used [17]:

$$d_0 = \frac{C_{10}(C_{10} - C_{21})(C_{10} - C_{12})}{(C_0 - C_{21})(C_0 - C_{10})} - [\frac{(C_{10} - C_{21})}{2(C_0 - C_{21})} + \frac{C_{10}}{3(C_0 - C_{10})}] \frac{(C_{10} - C_{12})^2}{(C_0 - C_{10})} , \tag{2.42a}$$

$$d_1 = \frac{(1 - C_{10})(C_{10} - C_{21})(C_{10} - C_{12})}{(C_0 - C_{21})(C_0 - C_{10})} + [\frac{(C_{10} - C_{21})}{2(C_0 - C_{21})} - \frac{1 - C_{10}}{3(C_0 - C_{10})}] \frac{(C_{10} - C_{12})^2}{(C_{01} - C_{10})} . \tag{2.42b}$$

These expressions are accurate to order for $(C_{10} - C_{12})^3$.

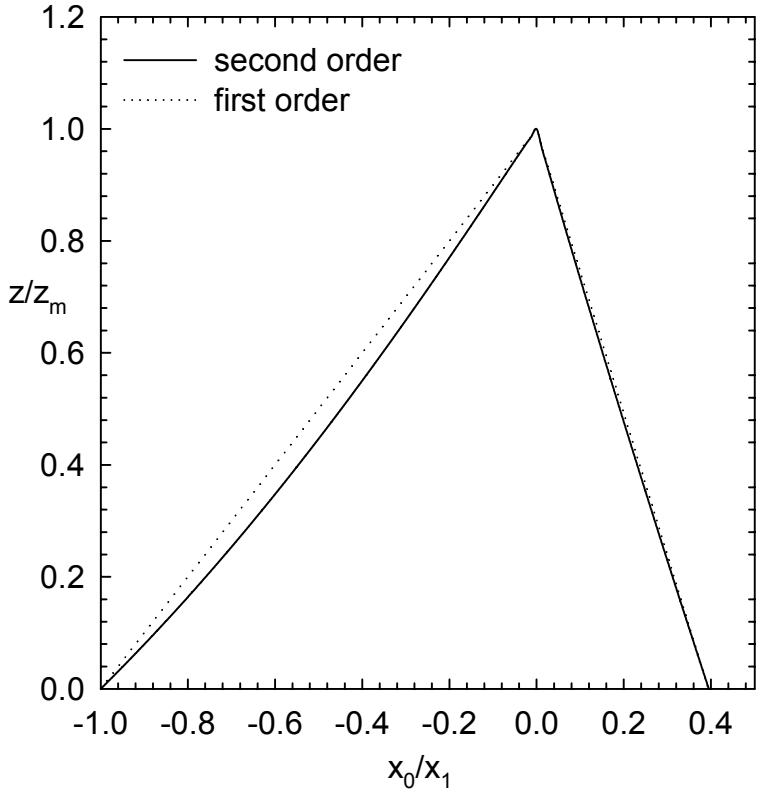

Fig. 2.9. Normalized marker displacement z/z_m versus initial marker position x_0 nondimensionalized by the interfacial position x_1 in the β phase of a Ag-Zn coupe. The first order asymptotic solution is given in (2.38a)-(2.38c), and the second order in (A5a)-(A5b).

2.8. Discussion

The one-layer solution reveals that the effective diffusivities of the interfaces vary linearly with the intrinsic diffusivities [17]. One of the main purposes of this chapter is to see if this conclusion holds for multiple layers. Fig. 2.6(a) shows that D_1 varies almost linearly with R_{A1} for constant R_{A2} and R_{B2}. When $R_{A2} = 0$, the relation is exactly linear. However, as R_{A2} increases, the relation becomes more nonlinear. Thus, the linearity valid for one product layer cannot be generalized to multiple layers.

This chapter assumes that the intrinsic diffusivities are constant in each product phase. This assumption allows a variable interdiffusion coefficient in each layer, and yields a well defined system of equations that is not limited to a particular material. However, for some binary alloys, the assumption may be too restrictive, as shown by the disagreement in Fig. 2.7. To fit a particular binary alloy, the intrinsic diffusivities may have to vary within a product phase. In that case, the growth is still self similar if the intrinsic diffusivities depend only on the concentrations, and the formulation presented here applies with only minor modifications.

In the "multi-foil" method, the maximum displacement z_m occurs at $x_0 = 0$. This is the displacement for markers initially at the interface, i.e. at $x_0 = 0$. It has been suggested that these markers follow the maximum Kirkendall velocity if R_{A1} is constant [31]. Here, the asymptotic solution can verify this. The Kirkendall velocity obeys (2.33), and the maximum velocity occurs at $dv/dx = 0$ or $d^2c_A/dx^2 = 0$, i.e. at the inflection point of the concentration profile. In terms of the

self-similar variables, the maximum velocity is at $d^2c/dy^2 = 0$. The second-order asymptotic solution in the Appendix A finds that position as

$$x = \frac{(C_0 - C_{10})(D_{B1} - D_{A1})x_1}{C_{10}(D_{B1} - D_{A1}) + D_{A1}}. \qquad (2.43)$$

Since $x_1^2/2t = d_1 D_{A1} + d_0 D_{B1}$ from (2.40),

$$x_1 = \frac{2t}{x_1}\frac{(C_{10} - C_{21})(C_{10} - C_{12})}{(C_0 - C_{21})(C_0 - C_{10})}[(1 - C_{10})D_{A1} + C_{10}D_{B1}] \quad ,$$

where d_0 and d_1 from (2.42) have been inserted. Substitution of x_1 into (2.43) yields

$$x = \frac{2(C_{10} - C_{21})(C_{10} - C_{12})(D_{B1} - D_{A1})}{(C_0 - C_{21})}\frac{t}{x_1}.$$

This is the same as z_m. Thus, within the assumptions of this model, markers initially at the interface indeed follow the maximum Kirkendall velocity.

2.9. Conclusion

This chapter studies the diffusion-controlled growth of N compound layers in binary diffusion couples with the nonlinear Kirkendall effect included. A self-similar transformation reduces the nonlinear partial differential equations to nonlinear ordinary differential equations, which are solved numerically by a fourth-order Runge-Kutta method. These nonlinear equations are coupled at the interfaces, the locations of which are unknown and are determined iteratively. A particular diffusion couple with two product layers has been analyzed in detail. It is found that the growth of one layer can be suppressed by the other when the diffusivity ratio is large. The method of finding intrinsic diffusion coefficients from only the locations of interfaces has been extended to two layers. The asymptotic

analysis valid for small concentration gradients is applied to the “multi-foil” method, and yields an analytic solution for the displacement curve. It is found that two vertice positions of the displacement curve are sufficient to calculate the intrinsic diffusion coefficients.

CHAPTER 3 CAPILLARY INSTABILITY OF A RETRACTING FILM STEP

3.1. Introduction

Thin solid films are widely used in electronic industries; they are the basic components of many micro electronic devices. Nowadays, these devices are made smaller by reducing the size of thin films. As a film becomes smaller, the surface to volume ratio is higher and the capillary force stronger. Since the same film surface displacement has more effect on the structural integrity of a smaller film, morphological evolution and instability of thin films are becoming more important.

In an experiment to study the effect of annealing on thin films, Kennefick and Raj deposited uniform copper films on sapphire [37]. The thickness of these uniform films ranges from 50-250 nm. The film and the substrate are heated at 650 °C under nonoxidizing conditions for 20 min to 48 hr. They found that holes form at foreign, non-wetting inclusions, and the film starts to break up at the boundaries of the holes. This breakup proceeds until the entire film decomposes into isolated, irregular islands. To study this breakup process quantitatively, Jiran and Thompson deposited uniform gold film strips on silica substrates and studied the retraction of the film edges [38]. These strips are 40-90 nm thick and 25 μm wide. The strips are annealed at 700-800 °C for about an hour. They found that the initially smooth and straight edges become unstable and develop large amplitude undulations, which eventually extend into “fingers”. These “fingers” then pinch off to form isolated islands to minimize the total surface energy of the

system. The rest part of the film then repeats the retraction process. In electronic materials processing, it is important that a bounded uniform film remains continuous. Therefore, this boundary-induced instability needs to be understood and suppressed.

The stability and evolution of holes in uniform films on substrates have been analyzed by Svolovitz and Safran [5]. In part I of that work, they studied the stability of an array of cylindrical holes in a uniform film. They compared the total surface energy of a unit cell of the array with that of a film with no hole but with the same film volume. They found that a hole may close completely or open toward a stable size. In part II, they investigated numerically the temporal evolution of a hole in a uniform film. The hole is not in equilibrium initially, and it evolves by either surface diffusion or evaperation-condensation. In both cases, there exists a critical hole size, above which the hole grows, and below which it shrinks. The linear stability of a hole in a solid film has been studied by Wong et al [39]. The steady state is a catenoidal hole with zero surface mean curvature. The hole is perturbed assuming that the perturbation evolves by capillarity-driven surface diffusion. The perturbation is expanded in normal modes with their growth rates determined by solving an eigenvalue problem. It is found that a catenoidal hole is always unstable. These stability analyses of holes are valuable, but they cannot explain the breakup of uniform films into islands, which starts from film edges. The breakup occurs even for films without holes.

The retraction of a film edge on a substrate has been studied by Wong et al [40]. They assumed that the uniform film extends to infinity at the other end and

evolves by capillarity-driven surface diffusion. They found that the retracting film edge forms a thickened ridge followed by a valley. The valley sinks with time and eventually touches the substrate. The ridge then detaches from the film. The new film edge retracts to form another ridge accompanied again by a valley, and the mass shedding cycle is repeated. Since their analysis is two-dimensional, it cannot describe the fingering seen in Jiran and Thompson's experiments, but it does give a break-up mechanism in two dimensions, and the predicted retraction speed agrees with experiment.

The present work studies the instability of the retracting film profile obtained previously by Wong et al [40]. Their two-dimensional film profile is perturbed in three dimensions. The growth rate of the perturbation is analyzed as a function of the wavelength of the perturbation and the retracting speed of the moving edge. We find one unstable mode of perturbation, which makes the originally straight contact line wavy. Further growth of this unstable mode can lead to the "fingers" observed by Jiran and Thompson.

This paper is organized a follows. The base state and the perturbation are described in Section 3.2. The resulting eigenvalue problem has an analytic solution that requires numerical evaluation (Section 3.3). Numerical results are presented in Section 3.4. Asymptotic solutions are derived in Section 3.5 and compared with the numerical results. We discuss the implications in Section 3.6 and conclude in Section 3.7.

3.2. Mathematic Model

3.2.1 Base State

Retraction of a two-dimensional step film on a substrate has been studied recently by Wong et al [39]. The film profile at zero time is a semi-infinite step, and it rearranges very quickly at the contact line to form an equilibrium angle α with the substrate. The film then retracts with a thickened edge followed by a valley, as illustrated in Fig. 3.1. As a solid film evolves by capillarity-driven surface diffusion, the film surface displaces with a normal velocity $\bar{u}_n$ that obeys [41]

$$\bar{u}_n = B\bar{\nabla}_s^2\bar{\kappa}, \tag{3.1}$$

in which $\bar{\nabla}_s$ is the surface gradient operator, $\bar{\kappa}$ is the surface mean curvature, and B is a material constant ($B = D_s\gamma\upsilon\Omega^2/k_BT_e$, where D_s is the surface diffusivity, γ is the surface energy per unit area which is taken as isotropic, υ is the number of diffusing atoms per unit area, Ω is the atomic volume, and k_BT_e is the thermal energy). This equation is derived using the fact that the chemical potential varies linearly with the curvature of the solid film surface. If the surface curvature is not uniform, then a gradient in chemical potential exists. This gradient drives a surface flux, which redistributes mass along the solid surface. The net effect is that the solid surface moves along its normal. Equation (3.1) has been applied to grain-boundary growing for measuring surface diffusivities [Xin, 2003], and to many other physical phenomena.

For the retraction of a semi-infinite film, such as that shown in Fig. 3.1, the unperturbed film thickness H constitutes a natural length scale. In what follows,

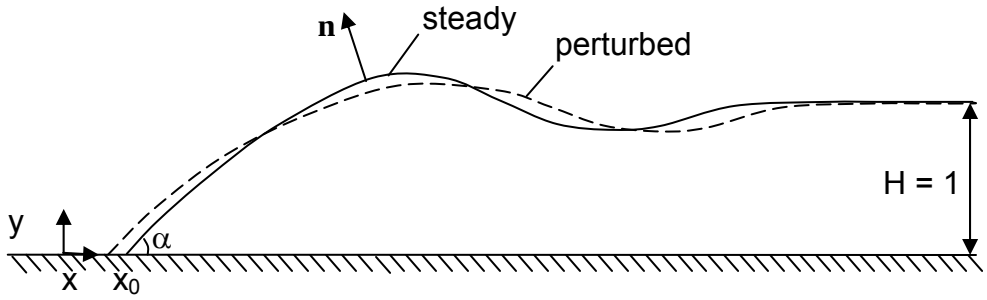

Fig. 3.1. A sketch of a solid film step in two dimensions. The steady film profile intercepts the substrate at $x = x_0$ with contact angle α (solid line). This contact angle is maintained for the perturbed profile (dashed line). The far-field film height H constitutes a natural length scale.

length and time are made dimensionless by H and H^4/B, respectively. In dimensionless variables, equation (3.1) becomes

$$u_n = \nabla_s^2 \kappa . \tag{3.2}$$

This governing equation is subject to the following boundary conditions. At the contact line, the height of the film is zero, the contact angle is in equilibrium, and the mass flux is zero. Far from the contact line, the film is not disturbed and has unit height.

When the contact angle α > $30°$, Wong et al solved the evolving film profile for different α by a numerical method [40]. However when the contact angle $\alpha \to 0$, the breakup time tends to infinity, and the numerical simulation takes too long to reach film breakup. Thus, a small-slope analytic solution is found that is valid for time t >>1. Define a coordinate x^* that moves with the contact line:

$$x^* \equiv x - x_0(t), \tag{3.3}$$

where $x_0(t)$ is the position of the contact line. A new set of variables

$$X = \alpha x^*, \; Y = y, \; T = \alpha^4 t, \tag{3.4}$$

transforms the governing equation (3.2) into

$$\frac{\partial Y}{\partial T} - b^3 \frac{\partial Y}{\partial X} = -\frac{\partial^4 Y}{\partial X^4}, \tag{3.5a}$$

$$b = \frac{1}{\alpha}\left(\frac{dx_0}{dt}\right)^{1/3} . \tag{3.5b}$$

By assuming that the time derivative term is small compared with the other two terms, Wong et al found a series solution for the retracting film profile Y_s [40]. The first two terms are

$$Y_s(T;X) = Y_0 + Y_1, \tag{3.6a}$$

$$Y_0 = 1 + e^{-bX/2}[(\frac{2-b}{\sqrt{3}b})\sin(\frac{\sqrt{3}}{2}bX) - \cos(\frac{\sqrt{3}}{2}bX)], \tag{3.6b}$$

$$Y_1 = (1+\frac{5b}{6})\frac{b}{12}e^{-bX/2}\{X(X+4)\cos(\frac{\sqrt{3}}{2}bX) - [b(1-2b)X^2 + 4(3-b)X + 8]\frac{1}{\sqrt{3}b}\sin(\frac{\sqrt{3}}{2}bX)\}, \tag{3.6c}$$

$$b = \left(\frac{2}{5T}\right)^{1/5} - \frac{5}{24}\left(\frac{2}{5T}\right)^{2/5} + \dots, \tag{3.6d}$$

where db/dT in the original expression of Y_1 has been evaluated using (3.6d) and expressed in terms of b. Solution (3.6) satisfies (3.5) with a residual $\partial Y_1/\partial T$, which vanishes as $T \to \infty$. The film profile represented by (3.6) is steady in the sense that it is independent of time explicitly, but it depends on time implicitly through its dependence on b. This time dependence is weak, so the film profile Y_s evolves slowly.

3.2.2 Normal Mode Analysis

In three dimensions, the governing equation (3.2) under the small-slope assumption and in a frame moving with the contact line becomes

$$\frac{\partial Y}{\partial T} - b^3\frac{\partial Y}{\partial X} = -[\frac{\partial^4 Y}{\partial X^4} + 2\frac{\partial^4 Y}{\partial X^2\partial Z^2} + \frac{\partial^4 Y}{\partial Z^4}], \tag{3.7a}$$

$$Z = \alpha z, \tag{3.7b}$$

where z is the coordinate perpendicular to x and y. The “steady” profile in (3.6) is perturbed as

$$Y(T,X,Z) = Y_s(T;X) + \delta(T,X,Z)\,. \tag{3.8}$$

Substituting (3.8) into (3.7) and assuming $\partial Y_1/\partial T << \partial\delta/\partial T$ yields

$$\frac{\partial\delta}{\partial T} - b^3\frac{\partial\delta}{\partial X} = -[\frac{\partial^4\delta}{\partial X^4} + 2\frac{\partial^4\delta}{\partial X^2\partial Z^2} + \frac{\partial^4\delta}{\partial Z^4}]\,. \tag{3.9}$$

The disturbance is then expressed in normal modes:

$$\delta(T,X,Z) = e^{\sigma T}\cos(kZ)f(X)\,, \tag{3.10}$$

where σ is the growth rate or the eigenvalue and f(X) is the eigenfunction. Substitution of (3.10) into (3.9) leads to an eigenvalue problem:

$$\frac{d^4f}{dX^4} - 2k^2\frac{d^2f}{dX^2} - b^3\frac{df}{dX} + k^4f + \sigma f = 0\,. \tag{3.11}$$

Solution of this equation yields the growth rate σ in terms of the wave number k and constant b.

3.2.3 Boundary Conditions for the Eigenvalue Problem

Boundary conditions for f(X) are complicated because the boundary location is unknown. At the contact line, $X = X_p$ (value unknown),

$$Y = 0\,, \tag{3.12a}$$

$$\mathbf{n}\cdot\mathbf{e}_Y = \cos\alpha\,, \tag{3.12b}$$

$$\mathbf{m}\cdot\nabla_s\kappa = 0\,, \tag{3.12c}$$

where

$$\mathbf{n} = \frac{-Y_X\mathbf{e}_X + \mathbf{e}_Y - Y_Z\mathbf{e}_Z}{\sqrt{1+Y_X^2+Y_Z^2}}\,, \tag{3.12d}$$

$$\mathbf{m} = Y_X \mathbf{e}_X + (Y_X^2 + Y_Z^2)\mathbf{e}_Y + Y_Z \mathbf{e}_Z , \tag{3.12e}$$

$$\nabla_s = \frac{1}{1 + Y_X^2 + Y_Z^2} \{\mathbf{e}_X [(1 + Y_Z^2)\frac{\partial}{\partial X} - Y_X Y_Z \frac{\partial}{\partial Z}] + \mathbf{e}_Y (Y_X \frac{\partial}{\partial X} + Y_Z \frac{\partial}{\partial Z})$$

$$+ \mathbf{e}_Z [(1 + Y_X^2)\frac{\partial}{\partial Z} - Y_X Y_Z \frac{\partial}{\partial X}])\} , \tag{3.12f}$$

$$\kappa = \nabla_s \cdot \mathbf{n} . \tag{3.12g}$$

In the above equations, $\mathbf{e}_X$, $\mathbf{e}_Y$, $\mathbf{e}_Z$ represent unit vectors in the X, Y, Z directions, **n** and **m** are unit vectors normal and tangential to the film surface (Fig. 3.1), and the subscripts X and Z of Y denote differentiation. The boundary conditions in (3.12) state that the height of the film is zero, the contact angle is fixed, and the mass flux tangent to the film surface and into the substrate is zero at the contact line. The contact line at $X = X_p$ is the interception point of the perturbed film profile with the substrate (Fig. 3.1). However, the contact line position can vary and is unknown, and must be solved together with the film profile. For this linear perturbation problem, the boundary conditions can be Taylor expanded about the position $X = 0$ of the static contact line to leading order in δ. The position $X = 0$ is the interception point of the steady film profile with the substrate or $x = x_0$ in Fig. 3.1.

Substitution of $Y = Y_s + \delta$ into (3.12), keeping only linear terms in δ, and expanding the results around $X = 0$ gives that at X = 0 (Appendix B),

$$6\frac{df}{dX} + b(6 - b)f = 0 , \tag{3.13a}$$

$$\frac{d^3 f}{dX} - k^2 \frac{df}{dX} - b^3 f = 0 . \tag{3.13b}$$

As $X \to \infty$,

$$\frac{df}{dX} = 0, \tag{3.14a}$$

$$\frac{d^3 f}{dX^3} = 0. \tag{3.14b}$$

Note that the three boundary conditions at the contact line in (3.12) are combined into two in (3.13), and that all the boundary conditions are homogeneous.

3.3. Solution of the Eigenvalue Problem

Since (3.11) is linear in f with constant coefficients, a general solution is

$$f(X) = \sum_{j=1}^{4} C_j e^{a_j X} \quad . \tag{3.15}$$

The constants a_j, j =1,…,4, are found by substituting (3.15) into (3.11) and solving the quartic algebraic equation using Maple V®:

$$a_1 = p + q, \tag{3.16a}$$

$$a_2 = p - q, \tag{3.16b}$$

$$a_3 = -p + r, \tag{3.16c}$$

$$a_4 = -p - r, \tag{3.16d}$$

$$p = \frac{1}{2\sqrt{6}} \sqrt{8k^2 + s^{1/3} + (48\sigma + 64k^4) s^{-1/3}}, \tag{3.16e}$$

$$q = \frac{1}{2\sqrt{6}} \sqrt{u + 6b^3 p^{-1}}, \tag{3.16f}$$

$$r = \frac{1}{2\sqrt{6}} \sqrt{u - 6b^3 p^{-1}} \tag{3.16g}$$

$$u = 16k^2 - s^{1/3} - 48\sigma s^{-1/3} \quad - 64k^4 s^{-1/3}, \tag{3.16h}$$

$$s = 576k^2\sigma + 512k^6 + 108b^6 + 12\sqrt{768(b^6k^6 - \sigma^2k^4 - \sigma^3) + 9b^6(96\sigma k^2 + 9b^6)}\,.$$

(3.16i)

To find the eigenvalue σ, we impose the homogeneous boundary conditions (3.13) and (3.14) and seek a non-trivial solution for C_j, j = 1, …, 4. Since the boundary location at which (3.14) is applied is at infinity, the sign of the real part of a_i determines if $C_j = 0$ or not. The real part of a_j or $R(a_j)$ is plotted on the complex plane of σ for a full range of k and b. It is found that $R(a_1) > 0$ and $R(a_2) > 0$ for $R(\sigma) > 0$. (No solution is detected for $R(\sigma) \leq 0$.) Thus, $C_1 = C_2 = 0$ for a bounded solution, and we are left with

$$\mathbf{AC} = 0 \tag{3.17a}$$

where $\mathbf{A}$ is a second order matrix with elements

$$A_{11} = b^2 - 6b - 6a_3, \tag{3.17b}$$

$$A_{12} = b^2 - 6b - 6a_4, \tag{3.17c}$$

$$A_{21} = b^3 + k^2a_3 - a_3^3, \tag{3.17d}$$

$$A_{22} = b^3 + k^2a_4 - a_4^3\,. \tag{3.17e}$$

and

$$\mathbf{C} = \begin{pmatrix} C_3 \\ C_4 \end{pmatrix}. \tag{3.17f}$$

To have a nontrivial solution for $\mathbf{C}$, we need

$$|\mathbf{A}| = 0\,. \tag{3.18a}$$

Denote the real and imaginary parts of $|\mathbf{A}|$ by A_r and A_i, respectively, then

$A_r = 0,\ A_i = 0.$ (3.18b)

Solution of these two equations yields σ_r and σ_i, the real and imaginary parts of σ. Since these equations are difficult to solve, we plot A_r and A_i on the complex plane of σ for a given set of k and b values. We find that $A_r = 0$ is a segment along the line $\sigma_i = 0$ and $A_i = 0$ is an arc that intercepts the line segment at only one point. Thus, the interception point, which is an eigenvalue of (3.11), is always real. The position of that point is found by bisection to an accuracy of eight significant digits (see Appendix F for the computer program).

3.4. Numerical Results

The growth rate σ is plotted as a function of the wave number k for b=0.1 in Fig. 3.2. The growth rate increases with k starting at k=0 until σ reaches a maximum value σ_m at $k = k_m$. The growth rate then decreases monotonically, passing through zero at a critic wave number k_c. Thus, when the wave number of the perturbation is less than k_c, the film is always unstable whereas the perturbation is stable when the wave number of the perturbation is greater than k_c.

Perturbations are usually formed by random noise that spans the whole spectrum of wavelength. The perturbation with wavelength $k = k_m$ and maximum growth rate $\sigma = \sigma_m$ is most likely to be observed at late times. Thus, these results deserve more attention. Fig. 3.3 shows the eigenfunction f(X) when b = 0.1 and $k = k_m$ = 0.0685. The eigenfunction is computed from (3.15) and is the sum of two complex exponential functions of X, both decaying in X. The

eigenfunction has the highest magnitude at X=0, and it oscillates around zero with exponentially decreasing amplitude. The eigenfunction reflects the shape of the perturbation in the X direction at constant Z, as defined in (3.10). The effect of the perturbation δ on the base state is revealed by superimposing the perturbation on the equilibrium shape, as shown in Fig. 3.4. The magnitude of the perturbation is 20% of the peak film height. The figure shows that the perturbation affects the contact-line region the most; its effect can barely be seen at the peak of the film at $X \approx 20$.

At $k = k_c$, σ = 0 and the perturbation δ satisfies the steady form of (3.9). Thus, the perturbed film profile Y in (3.8) can be taken as a new three-dimensional base state. The eigenfunction for $k = k_c$ and b = 0.1 is also plotted in Fig. 3.3; it is the sum of two complex exponential functions of X, just like the eigenfunction for $k = k_m$. However, the oscillation is hardly observable. The perturbed film profile is similar to the one shown in Fig. 3.4, especially near the contact-line region.

The maximum growth rate σ_m and the wave numbers k_m and k_c depend on b, and are plotted as a function of b in Figs. 3.5 and 3.6. Fig. 3.5 reveals that σ_m obeys a power law in the domain of interest:

$$\sigma_m = \beta_1 b^{\beta_2}. \qquad (3.19)$$

A good fit is obtained when $\beta_1 = 0.464$, and $\beta_2 = 3.876$. The power fit in (3.19) is also plotted in Fig. 3.5.

The wavenumbers k_m and k_c vary almost linearly with b as shown in Fig 3.6. The parameter b depends on time T following (3.6d). Since the base-state film profile is taken as continuous, this imposes a limit on time because at a critical time $T = T_c$, the base-state film profile starts to breakup into two parts [39]. Thus, the stability analysis in this work is only valid for $T < T_c$ or $b > b_c = b(T_c)$. The critical value b_c is plotted as a function of the contact angle σ_m in Fig. 3.7. It shows that b_c does not change much over the complete range of σ_m; it decreases from

$$b_c = 0.0702 \tag{3.20}$$

at $\sigma_m = 0$ to $b_c = 0.0457$ at $\sigma_m = 180°$. The value at small α is found from the asymptotic solution for T_c (=216,995.9) in the limit $\alpha \to 0$ [39]. Since our stability analysis holds for $b > b_c$, only data with $b \geq 0.05$ are plotted in Fig. 3.6.

3.5. Asymptotic Solution

3.5.1 Asymptotic Solution for σ in the Limit $k \to 0$.

In the limit $k \to 0$, (3.16) can be expanded to $O(k^2, \sigma)$ as

$$a_1 = b - \frac{\sigma}{3b^3} + \frac{2k^2}{3b} \tag{3.21a}$$

$$a_2 = \frac{\sigma}{b^3} \tag{3.21b}$$

$$a_3 = -\frac{b}{2} - \frac{\sigma}{3b^3} - \frac{k^2}{3b} + i\sqrt{3}\left(\frac{b}{2} - \frac{k^2}{3b}\right) \tag{3.21c}$$

$$a_4 = -\frac{b}{2} - \frac{\sigma}{3b^3} - \frac{k^2}{3b} - i\sqrt{3}\left(\frac{b}{2} - \frac{k^2}{3b}\right), \tag{3.21d}$$

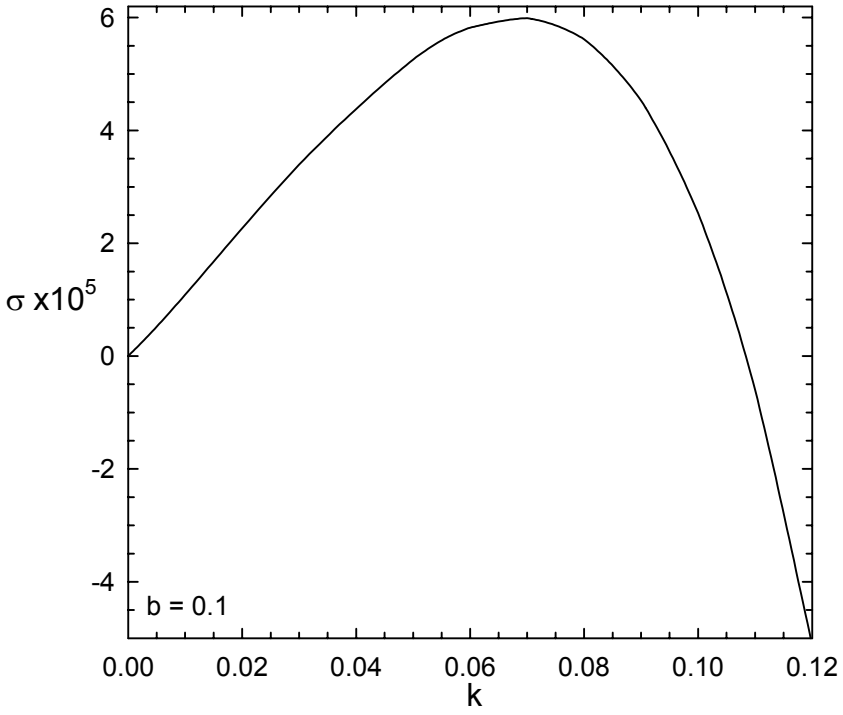

Fig. 3.2. Growth rate σ verus wave number k for b=0.1. The maximum growth rate $\sigma = \sigma_m = 5.997 \times 10^{-5}$ occurs at k = k_m = 0.0685, and $\sigma = 0$ at k = k_c = 0.1084

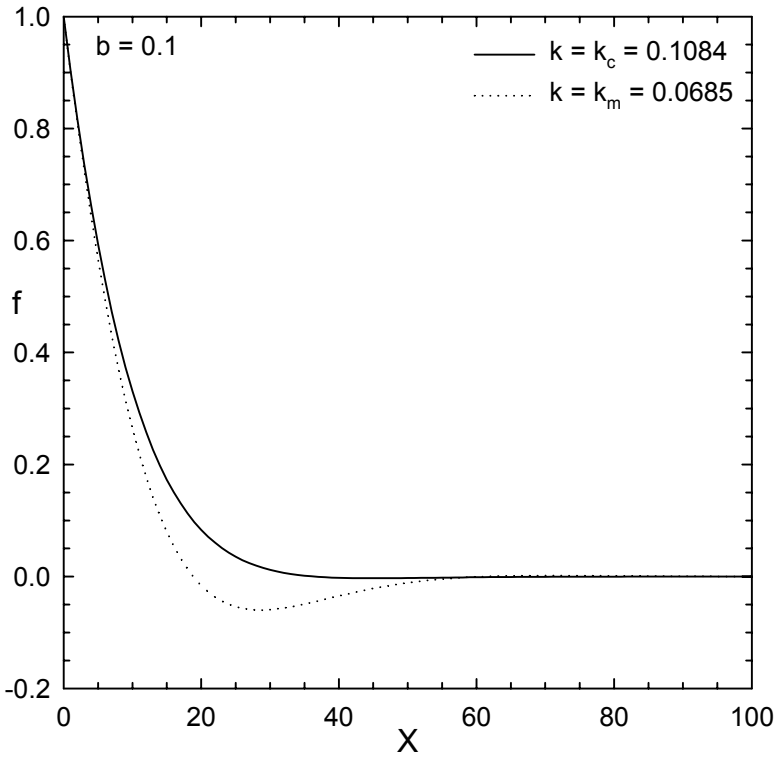

Fig. 3.3. Eigenfunctions computed using (3.15) for b = 0.1.

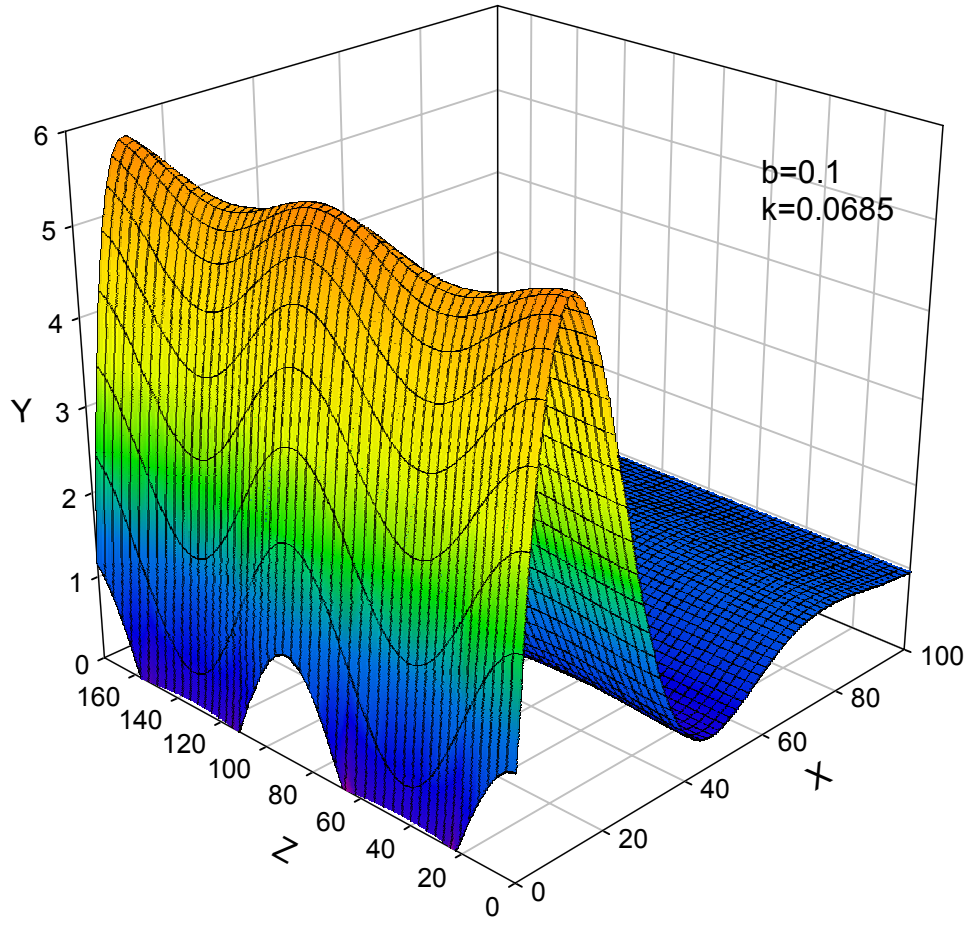

Fig. 3.4. The perturbed film shape for b=0.1 and k = k_m = 0.0685. The magnitude of the perturbation is 20% of the peak film height. The X-position of the contact line varies sinusoidally with Z following (3.10) and (B3).

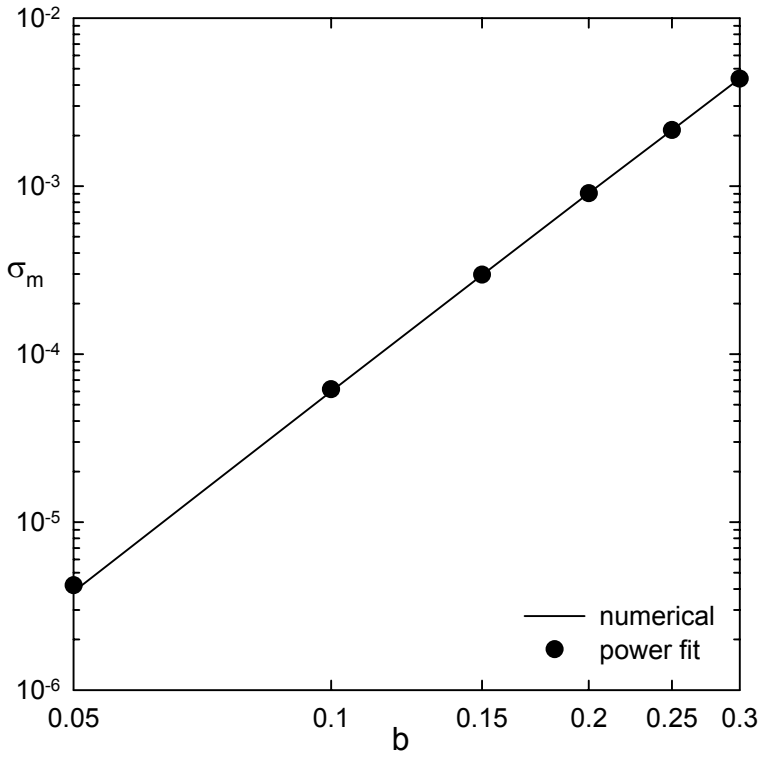

Fig. 3.5. The maximum growth rate versus b. The power fit is given in (3.19).

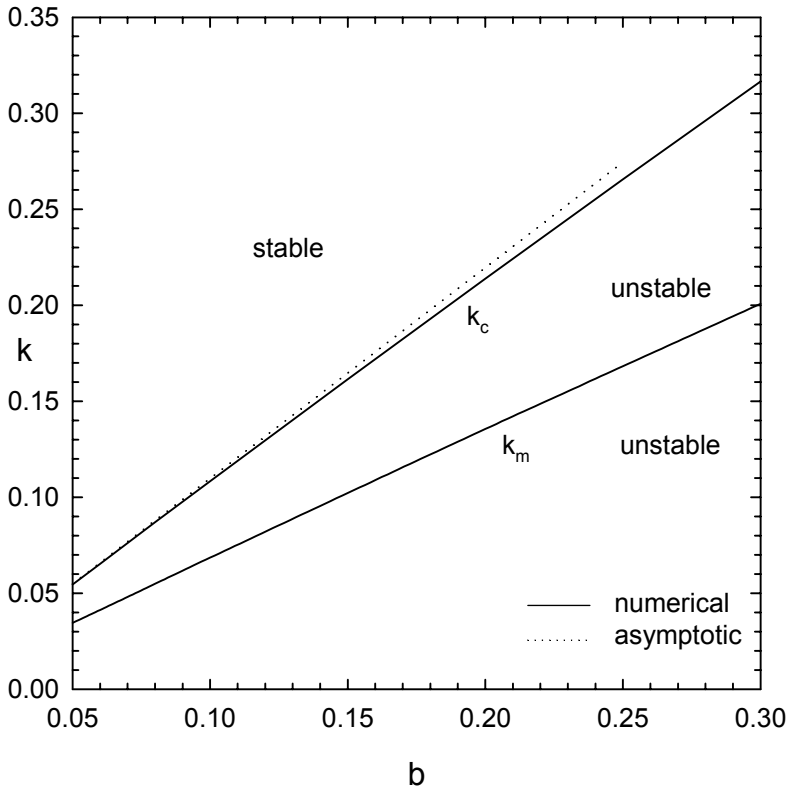

Fig. 3.6. Wavenumbers k_m and k_c versus b. A perturbation is stable if $k \geq k_c$ and unstable if $k < k_c$. The asymptotic solution for k_c holds in the limit $b \to 0$ and is listed in (3.26).

where $i = \sqrt{-1}$. Higher-order terms in σ are not needed since the final result gives $\sigma \sim k^2$. Equation (3.21) shows that if 1 >> R(σ) > 0, then $R(a_1) > 0$ and $R(a_2) > 0$, in agreement with the numerical results. Thus, $C_1 = C_2 = 0$ and the matrix **A** in (3.17) has elements

$$A_{11} = b(b-3) + 2\sigma/b^3 + 2k^2/b - i\sqrt{3}(3b + 2k^2/b), \tag{3.22a}$$

$$A_{12} = b(b-3) + 2\sigma/b^3 + 2k^2/b + i\sqrt{3}(3b + 2k^2/b), \tag{3.22b}$$

$$A_{21} = k^2 b/2 - \sigma/2b - i\sqrt{3}(\sigma/b + k^2 b)/2, \tag{3.22c}$$

$$A_{22} = k^2 b/2 - \sigma/2b + i\sqrt{3}(\sigma/b + k^2 b)/2. \tag{3.22d}$$

For a nontrivial solution of (C_3, C_4), $|\mathbf{A}| = 0$, which gives

$$\sigma = (6 - b)bk^2. \tag{3.23}$$

Fig. 3.7 plots this asymptotic prediction together with the numerical result for b = 0.1. The agreement at small k validates both solutions. Although the curve in Fig. 3.2 seems to suggest linear growth for σ at small k, the results in Fig. 3.7 indicate that σ increases quadratically with k, in agreement with many capillary instability problems [43, 46].

3.5.2 Asymptotic Solution for k_c in the Limit $b \to 0$.

Since the base-state film profile was derived in the limit $T \to \infty$ or $b \to 0$, we seek an asymptotic for k_c in the same limit. At the critical wave number k_c, the growth rate $\sigma = 0$. Substitution of $\sigma = 0$ into (3.16) and keeping only a_3 and a_4 leads to

$$a_3 = -p + r, \tag{3.24a}$$

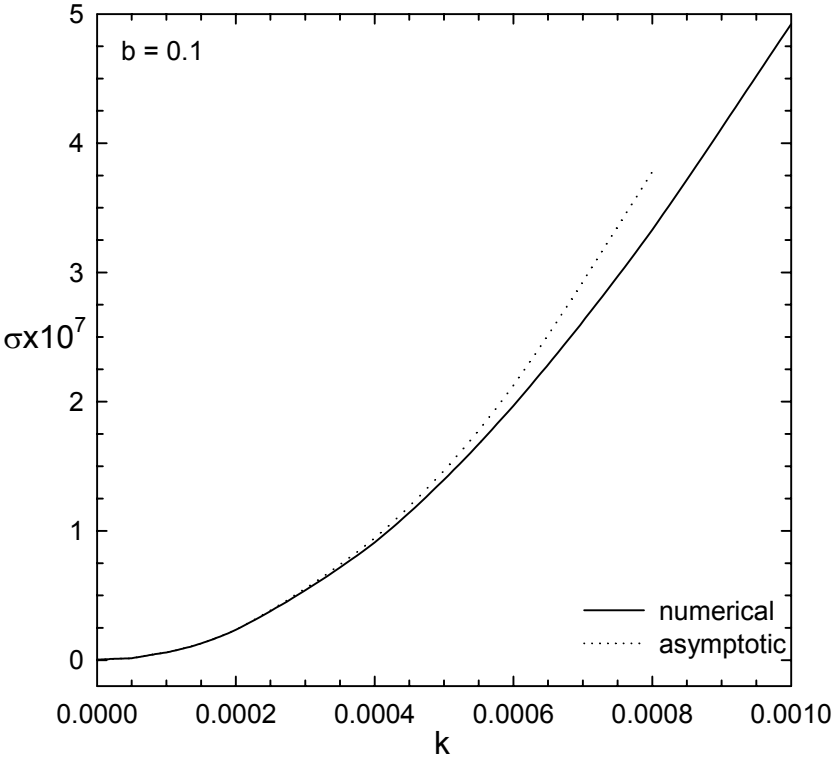

Fig. 3.7. Growth rate σ versus wavenumber k for b = 0.1. The asymptotic solution is given in (3.23).

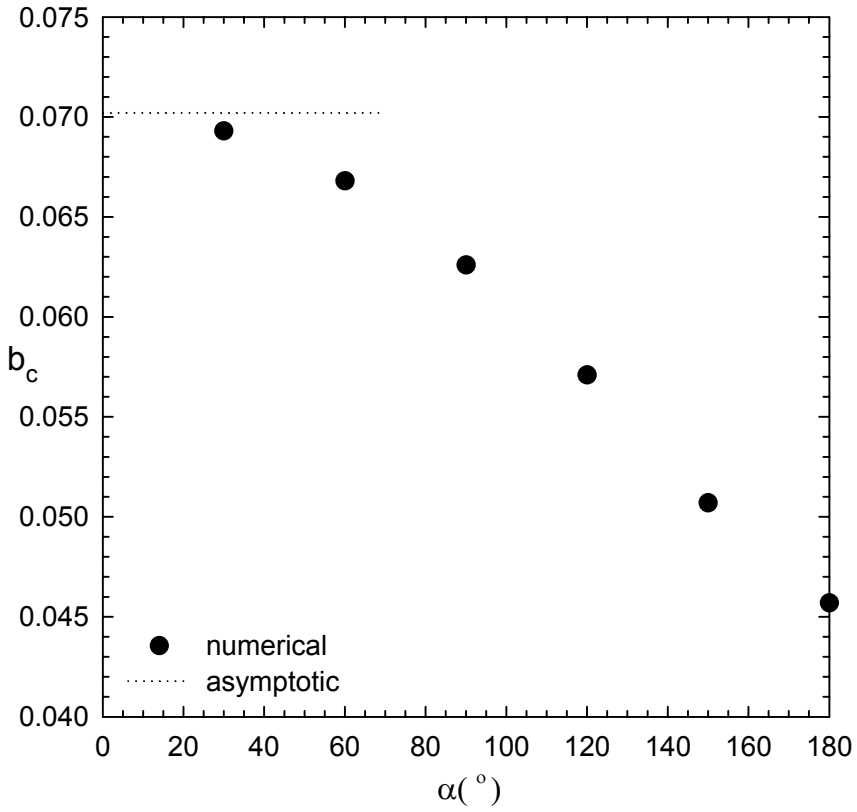

Fig. 3.8. The critical b_c versus the contact angle α. The asymptotic solution is valid for $\alpha \to 0$ and is listed in (3.20). The base state of the stability analysis holds for $b > b_c$.

$$a_4 = -p - r, \tag{3.24b}$$

$$p = \frac{1}{2\sqrt{6}}\sqrt{8k_c^2 + s^{1/3} + 64k_c^4 s^{-1/3}}, \tag{3.24c}$$

$$r = \frac{1}{2\sqrt{6}}\sqrt{-(s^{1/6} - 8k_c^2 s^{-1/6})^2 - 6b^3 p^{-1}}, \tag{3.24d}$$

$$s = 512k_c^6 + 108b^6 + 12b^3\sqrt{768k_c^6 + 81b^6}. \tag{3.24e}$$

Thus, p is real, r is imaginary, and a_3 and a_4 have negative real parts. Matrix $\mathbf{A}$ in (3.17) remains the same with elements

$$A_{11} = b^2 - 6b - 6a_3, \tag{3.25a}$$

$$A_{12} = b^2 - 6b - 6a_4, \tag{3.25b}$$

$$A_{21} = b^3 + k_c^2 a_3 - a_3^3, \tag{3.25c}$$

$$A_{22} = b^3 + k_c^2 a_4 - a_4^3. \tag{3.25d}$$

The critical wavenumber k_c is determined from $|\mathbf{A}| = 0$. In the limit $b \to 0$, k_c is expanded in a series as

$$k_c = c_0 + c_1 b + \ldots. \tag{3.26}$$

To find c_0, substitute the series (3.26) into (3.24) and set b = 0. This gives $a_3 = a_4 = -c_0$. Thus, $|\mathbf{A}| = 0$ implies

$$c_0 = 0. \tag{3.27}$$

The coefficient c_1 is found by substituting $k_c = c_1 b$ into (3.24). Imposing the condition $|\mathbf{A}| = 0$ leads to a nonlinear algebraic equation for c_1, which is solved numerically by Maple V®:

$$c_1 = -0.1435 . \tag{3.28}$$

The asymptotic solution for k_c is also plotted in Fig. 3.6 and agrees well with the numerical result in the appropriate limit.

3.6. Discussion

The governing equation (3.9) of the perturbation δ is derived assuming $\partial Y_1 / \partial T << \partial \delta / \partial T$. This assumption imposes a limit on time. From the expression of Y_1 in (3.6a), we can calculate

$$\frac{\partial Y_1}{\partial T} = \frac{1}{12\sqrt{3}} \sin(\frac{\sqrt{3}}{2} bX) e^{-bX/2} \frac{db}{dT} [\frac{1}{2} b(-2b^2 + b - 3)X^3 + 2b(2b-1)X^2 + 12(b-1)X$$

$$- 8] + \frac{1}{12} \cos(\frac{\sqrt{3}}{2} bX) e^{-bX/2} \frac{db}{dT} [\frac{1}{2} b(b^2 - b - 1)X^3 + (2b^2 - 8b + 1)X^2 + 4(1-b)X] . \tag{3.29}$$

The exponential function limits $X \sim b^{-1}$ or smaller for a non-vanishing value of $\partial Y_1 / \partial T$. By taking $X \sim b^{-1}$ and $db/dT \sim b^6$ from (3.6d), the maximum magnitude of $\partial Y_1 / \partial T$ is estimated to be

$$\frac{\partial Y_1}{\partial T} \sim b^4 . \tag{3.30}$$

According to (3.10),

$$\frac{\partial \delta}{\partial T} = \sigma e^{\sigma T} \cos(kZ) f(X) . \tag{3.31}$$

Since $\sigma \sim \sigma_m \sim b^{\beta_2}$ with $\beta_2 \approx 3.9$ as given in (3.19),

$$\frac{\partial \delta}{\partial T} \sim A b^{3.9} e^{b^{3.9} T} , \tag{3.32}$$

where A is the amplitude of the perturbation. The assumption of $\partial Y_1 / \partial T << \partial \delta / \partial T$ therefore requires

$$b^4 << A b^{3.9} e^{b^{3.9} T} \tag{3.33}$$

Substitution of (3.6d) into (3.33) yields

$$T >> (-\ln A)^{4.5} . \tag{3.34}$$

Given a perturbation of amplitude A, our stability analysis holds for time satisfying the above condition.

Jiran and Thompson observed that a gold film strip under annealing breaks up from the edge into isolated islands [38]. From Fig. 3.2 of their paper, the distance between two adjacent islands is measured to be 1-3 μm. Our stability analysis predicts that a retracting film edge is unstable. The unstable mode makes the contact line wavy, which is the precursor of the "fingers" seen in Jiran and Thompson's experiments. The perturbation with the maximum growth rate is likely the one survived at late times. The wavelength of this most unstable perturbation should determine the spacing of the "fingers" or the distance between two adjacent islands. This wave length in dimensional units is

$$\lambda_m = \frac{2\pi H}{k_m \alpha} . \tag{3.35}$$

In Jiran and Thompson's experiment, the thickness H of the gold film is 0.03 μm. For gold films the contact angle $\alpha \approx 180°$. However, (3.35) is valid for small α. Thus, we assume $\alpha = 90°$ as a compromise. From Fig. 3.6 of this paper, k_m does not vary much for the range of b that is of interest. As an example, we take b =

0.1. This gives $k_m = 0.0685$, and thus $\lambda_m = 1.8$ μm which agrees with the distances between islands observed in Jiran and Thompson's experiments.

The most unstable perturbation may breakup the film in a time t given by $t\sigma_m \sim 1$. This estimate comes from the exponential growth of the perturbation. In dimensional terms, this breakup time is

$$t^* = \frac{H^4}{B\alpha^4 \sigma_m}. \tag{3.36}$$

For Au at 775°C, $D_s = 2.02 \times 10^{-6}\,cm^2/s$, $\gamma = 1.78 J/m^2$, $\Omega = 1.78 \times 10^{-23}\,cm^3$ and we take $\upsilon \approx \Omega^{-2/3} = 1.5 \times 10^{15}\,cm^{-2}$. Thus $B = 1.2 \times 10^{-4}\,\mu m^4/s$. The film thickness H = 0.03 μm, and we again use $\alpha = 90°$. The maximum growth rate $\sigma_m \sim b^{3.8}$ as shown in Fig. 3.5. For convenience, we again take b = 0.1. This gives $\sigma_m = 5.997 \times 10^{-5}$, and thus $t^* = 18s$.

The value of λ_m is reliable since k_m is insensitive to variation in b. However, the value of t^* can only be viewed as a particular case because σ_m increases by about 1000 times over the range of b. The base state of the stability analysis holds in the limit $T \to \infty$ or $b \to 0$. The assumption $\partial\delta/\partial T >> \partial Y_1/\partial T$ of the perturbation equation leads to $T >> (-\ln A)^{4.5}$ in (3.34) or $b << (\ln A)^{-0.9}$. This together with $b > b_c$ in (3.20) brackets a range of b that the stability analysis applies. The sensitive of σ_m to variation in b makes it difficult to arrive at an accurate estimate of t^*. Probably, the only conclusion that can be inferred from $\sigma_m(b)$ is that the fingering instability would breakup the film at an early stage of retraction.

3.7. Conclusion

The straight edges of solid film strips have been observed to retract and develop large amplitude undulations. These “fingers” grow and finally detach from the film to form isolated islands. This work studies the three-dimensional instability of a retracting film edge on a substrate. The retracting film profile is two dimensional with a straight contact line. A cross section of the film shows a thickened edge followed by a valley and the film is unbounded at the other end. This profile is perturbed in three dimensions, assuming that the film evolves by capillarity-driven surface diffusion. We find one unstable mode of perturbation. The growth rate σ of the unstable mode depends on the velocity of the retracting edge (through b) and the wavenumber k of the sinusoidal perturbation along the film edge. A faster retracting film edge is more unstable. When the wave number of the perturbation is less than a critical wavenumber k_c, the film is always unstable, whereas the film is always stable when $k \geq k_c$. Asymptotic solutions are derived for σ in the limit $k \to 0$ and for k_c in the limit $b \to 0$, and they agree with the full numerical solutions in the appropriate limits. The wavelength of the most unstable perturbation agrees with the spacing between two adjacent islands observed in experiments.

CHAPTER 4 RAYLEIGH'S INSTABILITY OF THIN WIRES WITH STRONG CIRCUMFERENTIAL SURFACE ENERGY ANISOTROPY

4.1.Introduction

A thin liquid thread is unstable and will breakup into droplets to minimize the surface energy. The linear stability of a liquid jet was first studied by Lord Rayleigh [42]. Given a circular cylindrical liquid jet of radius R, its linear stability is revealed by imposing a small perturbation on the surface position in the form of a normal mode:

$$r = R + Ae^{\sigma t}\cos n\theta \cos kz, \tag{4.1}$$

where A is the amplitude of the perturbation, t is time, and (r, θ, z) are cylindrical coordinates defined at the center of the cylinder with z along the axis (Fig. 4.1). By assuming inviscid flow and a capillarity-driven pressure gradient, Lord Rayleigh found the growth rate as

$$\sigma = \left(\frac{\gamma}{\rho R^3}\right)^{1/2}\left[\frac{kRI_1(kR)}{I_0(kR)}(1 - k^2R^2 - n^2)\right]^{1/2}, \tag{4.2}$$

where γ is surface tension, ρ is liquid density, and $I_0 = I_0(kR)$ and $I_1 = I_1(kR)$ are the modified Bessel function of the first kind of order 0 and 1, respectively. If the perturbation is axisymmetric (n = 0), then $\sigma > 0$ for $k < 1/R$. Thus, long wave axisymmeric perturbations will grow in time. Nonaxisymmetric perturbations ($n \geq 1$) do not grow since σ is imaginary.

The stability of nonaxisymmetric modes has been suggested as a possible stabilizing source. It has been proposed that a liquid jet emitting from a non-circular orifice may have the unstable axisymmetric mode suppressed. A recent

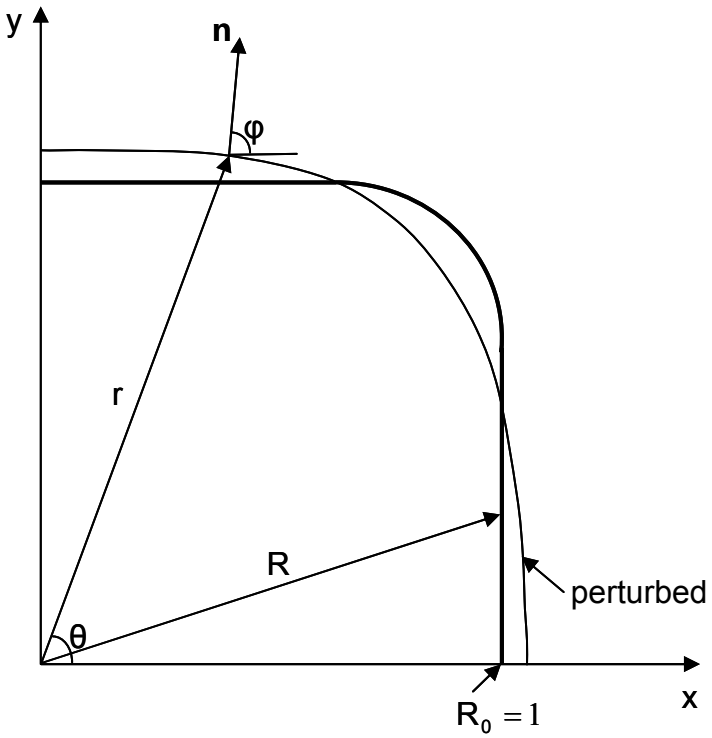

Fig. 4.1. Sketch of the equilibrium (thick line) and perturbed (thin line) wire shapes. The perturbed surface is located by cylindrical coordinates $r = r(\theta)$, whereas the equilibrium surface by $R(\theta)$. Surface normal vector **n** makes an angle φ with the x-axis. The wire is symmetric about the x-axis, and R_0 is half the height of the crystal along the symmetry plane and is used as a length scale.

experimental study of a liquid column supported between two metal disks shows stabilization under acoustic radiation pressure. The main stabilization is attributed to the radiation pressure. However, the liquid column becomes elliptic in the acoustic field, and this may also contribute to the stabilization.

A solid wire is also subject to Rayleigh's instability because it has surface energy and can change shape by surface diffusion [40]. A solid wire can have a non-circular equilibrium shape owing to surface energy anisotropy. Thus, it provides a natural system for studying the effect of non-circular steady state. Nichols and Mullins [43] analyzed the linear stability of a circular wire with isotropic surface energy. He found that if a wire of radius R is perturbed by a disturbance of the form presented in (1.1), then the disturbance may grow with a growth rate

$$\sigma = \frac{B}{R^4}(n^2 + k^2R^2)(1 - k^2R^2 - n^2), \qquad (4.3)$$

where B is a material constant. Thus, axisymmetric disturbances with wavelengths greater than $2\pi R$ will also grow, and non-axisymmetric disturbances will decay.

The linear stability of a wire on a solid substrate has been studied by McCullum et al [46]. They assumed that the surface energy is isotropic so that the wire has the cross-sectional shape of a part-circle. The wire surface touches the substrate with a specified contact angle. They found that the wire is unstable to long-wave perturbations of the varicose (sausage) type. However, the range of unstable wavelength is always less than that of a freely-suspended circular cylinder with the same volume. Since the steady state of the wire is not axisymmetric, this result seems to suggest that a non-circular steady state is stabilizing. However, the stabilization may be attributed to the presence of the substrate.

The linear stability of a wire with surface energy anisotropy was first studied by Cohn. He assumed that the surface energy varies linearly in the axial direction but is isotropic in the circumferencial direction. As a result, the wire is still circular. He found that the anisotropy can be stabilizing or destabilizing. Gurski and McFadden investigated the linear stability of a wire with surface energy anisotropy in both axial and circumferencial directions. Their stability analysis is based on finding the sign of the second variation of the total surface energy. They found that the anisotropy can be stabilizing or destabilizing relative to the isotropic case. Their analysis, however, has a significant deficiency because it cannot yield the growth rates of the unstable perturbations.

The present chapter studies the linear stability of a triangular or square wire by expanding the perturbation in normal modes. This yields an eigenvalue problem in which the eigenvalue is the growth rate of a normal mode. We find that the zeroth and first modes are unstable for long wavelengths. The zeroth mode has the fastest growth rate, and the wavelength vorresponding to this growth rate will likely determine the size of particles after breakup.

Results obtained here for wires also apply to channels because mass moves by surface diffusion and it does not matter which side of the interface the solid lies. Evolution of channels in sapphire has been studied in an effort to understand crack healing in ceramics. It is found that under annealing channels breakup into bubbles in general. However, for some crystallographic orientations, the channels remain intact with thin cylindrical sections connected by thick nodes. Although this work deals with linear stability and cannot predict the second stable state observed in experiments, it

provides a first step in understanding the effect of surface energy anisotropy on linear stability and paves the way for future nonlinear analysis.

This chapter is organized as follows. The equilibrium shapes are first described in Section 4.2. Capillarity-driven surface diffusion is introduced next in Section 4.3. A perturbation in the form of a normal mode is imposed (Section 4.4). The numerical method used to solve the linear stability problem is presented in Section 4.5, and the numerical results are listed in Section 4.6. An analytic solution for weak-anisotropy is derived in Section 4.7 and compared with the numerical results. We discuss the implications in Section 4.8 and conclude in Section 4.9.

4.2. Equilibrium Shapes

In a crystalline solid, atoms are arranged on a lattice, and the surface free energy varies with the orientation of the surface plane relative to the lattice. As a crystal forms, the minimum energy orientations are preferentially exposed to form planar surfaces or facets. At equilibrium, the chemical potential μ of a crystal is constant [41]:

$$\mu = \Omega(\gamma + \frac{d^2\gamma}{d\varphi^2})\bar{\kappa}, \tag{4.4}$$

where Ω is the atomic volume, γ is the surface energy per unit area, φ is the angle the surface normal makes with the horizontal axis (Fig. 4.1), and $\bar{\kappa}$ is the surface curvature. Equation (4.4) holds for two dimensions.

In general, γ is prescribed as a function of φ. This approach works if the anisotropy is weak. However, when the anisotropy is strong, the surface stiffness $\gamma + d^2\gamma/d\varphi^2$ can become negative over certain crystallography orientation. This may induce ill-posedness in evolution problems [49].

Recently, a new model of facets has been developed that can avoid the ill-posedness. In this model, the surface stiffness is prescribed as a function of φ [50]:

$$\gamma + \frac{d^2\gamma}{d\varphi^2} = \gamma_0 H(\varphi), \tag{4.5}$$

where $\gamma_0 = \mu R_0/\Omega$ can be viewed as the isotropic surface energy per unit area (R_0 is half the height of the crystal along the symmetry plane as shown in Fig. 4.1). By comparing with (4.4), H is recognized as the radius of curvature of the equilibrium crystal surface, made dimensionless by R_0. In this approach, a facet is represented by the Dirac delta function in $H(\varphi)$, with the weight of the delta function equal to the length of the facet plane [50]. To facilitate numerical simulations, the delta function is replaced by a spike function [51]:

$$H(\varphi) = P + L\sum_{i=-M}^{M} [\cosh(\frac{\varphi - \varphi_i}{w})]^{-1}. \tag{4.6}$$

In total there are 2M + 1 spikes, with one centered at each $\varphi = \varphi_i$ (φ_i is the orientation of a facet plane on the equilibrium crystal). To model a solid wire surface, $H(\varphi)$ is only needed in $0 \le \varphi \le 2\pi$. Thus, M is chosen such that the spike at φ_{-M-1} or φ_{M+1} has negligible contribution to $H(\varphi)$ in the domain of interest. The height and width of the spike are controlled by L and w, respectively. Since $H(\varphi)$ is the radius of curvature of the equilibrium crystal surface, L is therefore the radius of curvature of the facet planes, and P that of the corners, all made dimensionless by R_0. (As the sharpness of corners on an equilibrium crystal depends on temperature, P can be used to study the effect of temperature.) If $P \ge 0$, then $H(\varphi) \ge 0$ and the surface stiffness is never negative. Thus,

the ill-posedness is avoided even for arbitrarily strong anisotropy.

The equilibrium wire shape is found from $H(\varphi)$ as follows. Consider a wire with a horizontal symmetry plane as shown in Fig. 4.1. A Cartesian coordinate system (x, y) is defined with the x-axis coinciding with the symmetry plane. The coordinates have been made dimensionless by R_0. If s is the arc-length along the crystal surface, then from geometry,

$$\frac{dx}{ds} = -\sin\varphi, \tag{4.7a}$$

$$\frac{dy}{ds} = \cos\varphi, \tag{4.7b}$$

and the radius of curvature $H = ds/d\varphi$ [51]. Thus,

$$\frac{dx}{d\varphi} = -H\sin\varphi, \tag{4.8a}$$

$$\frac{dy}{d\varphi} = H\cos\varphi. \tag{4.8b}$$

Hence, the wire shape obeys

$$x(\varphi) = 1 - \int_0^{\varphi} H\sin\varphi d\varphi, \tag{4.9a}$$

$$y(\varphi) = \int_0^{\varphi} H\cos\varphi d\varphi. \tag{4.9b}$$

These equations give the positions of the wire surface by varying φ from 0 to π. When $\varphi = \pi$, x = -1 and y = 0, and the above two equations yield two integral constraints on $H(\varphi)$:

$$\int_0^{\pi} H(\varphi)\sin\varphi d\varphi = 2, \tag{4.10a}$$

$$\int_0^{\pi} H(\varphi)\cos\varphi \, d\varphi = 0, \qquad (4.10b)$$

Thus, the parameter P, L, and w are related. Paticularly, as $w \to 0$, L ~ $(1 - P)w^{-1}$ [51]. Hence, w can be interpreted physically as a measure of the curvature of the facet planes in the equilibrium crystal. In this work, we set w = 0.05, and P = 1, 0.5, 0.35 and 0.05 for the square wire with $\varphi_i = i\pi/2$, and P = 1, 0.93, 0.7, 0.2 and 0.02 for the triangular wire with $\varphi_i = 2i\pi/3$. Given the narrow width of the spikes, we find that only 5 spikes (M = 2) are needed for an accurate value of $H(\varphi)$ in the domain $0 \le \varphi \le 2\pi$. Once w and P are specified, L is found from (4.10a) by evaluating the definite integral using the Newton-Coates method. Values of L are computed to an accuracy of 12 decimal places and are listed in Tables 1 and 2. The positions (x, y) of the crystal surface are determined from (4.9) by the same numerical method to the same accuracy (the computer program is listed in Appendix F). Some of the equilibrium shapes are plotted in Figs. 4.4 and 4.5. (The square shapes are rotated by 45° for better numerical accuracy of the eigenvalue.)

The cross-sectional area A_c of the wire changes with P and may be used as another length scale to make the variables dimensionless. The area can be calculated from the surface position (x, y) as

$$A_c = 2\int_0^{\pi} y\left(\frac{dx}{d\varphi}\right)d\varphi \quad . \qquad (4.11)$$

The above integrals are evaluated by the Newton-Coates method. Results of A_c are listed in Tables 1 and 2.

The surface energy of the equilibrium crystal can also be found from $H(\varphi)$ by

solving (4.5) with appropriate boundary conditions, as shown by Xin and Wong (2004). They have plotted the surface energy for square [50] and triangular [51] crystals with different w and P. Hence, their results will not be repeated here.

4.3. Capillarity-driven Surface Diffusion

Consider a thin wire in which capillarity is the main driving force and mass moves by surface diffusion (Fig. 4.1). If the wire is not in thermodynamic equilibrium, the chemical potential varies along the solid surface and the gradient induces diffusion along the surface. The resulting surface evolution is governed by [41]

$$\bar{u}_n = C\bar{\nabla}_s^2[(\gamma + \frac{d^2\gamma}{d\varphi^2})\bar{\kappa}], \tag{4.12}$$

where $\bar{u}_n$ is the normal surface velocity, $\bar{\nabla}_s$ is the surface gradient operator and $C = D_s u\Omega^2/k_B T$ (D_s is the surface diffusivity, u is the number of diffusion atoms per unit area, and $k_B T$ is the thermal energy). This equation is derived using the fact that the chemical potential varies linearly with the curvature of the wire surface. If the surface curvature is not uniform, then a gradient in chemical potential exists. This gradient drives a surface flux, which redistributes mass along the solid surface. The net effect is that the solid surface moves along its normal. The surface stiffness $\gamma + d^2\gamma/d\varphi^2$ is related to $H(\varphi)$ according to (4.5). Thus, (4.12) becomes

$$\bar{u}_n = C\gamma_0\bar{\nabla}_s^2(H\bar{\kappa}). \tag{4.13}$$

Equation (4.12) has been applied to model grain-boundary grooving for measuring surface diffusivities, and to model other physical phenomena [49].

If length and time are made dimensionless by R_0 and $R_0^4/C\gamma_0$, respectively, then in dimensionless variables (4.13) becomes

$$u_n = \nabla_s^2(H\kappa)\,. \tag{4.14}$$

The perturbed wire surface is located by $r = r(t,\theta,z)$. To express (4.14) in terms of r, we note $u_n = \mathbf{n}\cdot\partial\mathbf{x}/\partial t$, where $\mathbf{x} = r\mathbf{e}_r + z\mathbf{e}_z$ is the position vector of a surface point, and $\mathbf{n}$ is the outward unit normal vector shown in Fig. 4.1. Equation (4.14) then becomes [40]

$$\frac{\partial r}{\partial t} + \frac{G}{r}\nabla_s^2(H\kappa) = 0\,, \tag{4.15a}$$

where

$$\kappa = \nabla_s \cdot \mathbf{n}\,, \tag{4.15b}$$

$$\mathbf{n} = G^{-1}(-r\mathbf{e}_r + \frac{\partial r}{\partial\theta}\mathbf{e}_\theta + r\frac{\partial r}{\partial z}\mathbf{e}_z)\,, \tag{4.14c}$$

$$G = [r^2 + (\frac{\partial r}{\partial\theta})^2 + (r\frac{\partial r}{\partial z})^2]^{1/2}\,, \tag{4.15d}$$

$$\nabla_s = \frac{\mathbf{e}_r}{G^2}(\frac{\partial r}{\partial\theta}\frac{\partial}{\partial\theta} + r^2\frac{\partial r}{\partial z}\frac{\partial}{\partial z}) + \frac{\mathbf{e}_\theta}{G^2}\{r[1+(\frac{\partial r}{\partial z})^2]\frac{\partial}{\partial\theta} - r\frac{\partial r}{\partial\theta}\frac{\partial r}{\partial z}\frac{\partial}{\partial z}\}$$

$$-\frac{\mathbf{e}_z}{G^2}\{\frac{\partial r}{\partial\theta}\frac{\partial r}{\partial z}\frac{\partial}{\partial\theta} - [r^2 + (\frac{\partial r}{\partial\theta})^2]\frac{\partial}{\partial z}\}\,. \tag{4.15e}$$

The governing equation is subject to periodic boundary conditions. At $\theta = 0$ and $\theta = 2\pi$,

$$r\big|_0 = r\big|_{2\pi}\,, \tag{4.16a}$$

$$\left.\frac{\partial r}{\partial\theta}\right|_0 = \left.\frac{\partial r}{\partial\theta}\right|_{2\pi}\,, \tag{4.16b}$$

$$\left.\frac{\partial^2 r}{\partial\theta^2}\right|_0 = \left.\frac{\partial^2 r}{\partial\theta^2}\right|_{2\pi}\,, \tag{4.16c}$$

$$\left.\frac{\partial^3 r}{\partial\theta^3}\right|_0 = \left.\frac{\partial^3 r}{\partial\theta^3}\right|_{2\pi}\,. \tag{4.16d}$$

4.4. Linear Stability

The linear stability of a wire is determined by applying a perturbation $\delta(t,\theta,z)$ to the equilibrium shape $R(\theta)$ as shown in Fig. 4.1:

$$r(t,\theta,z) = R(\theta) + \delta(t,\theta,z)\,. \tag{4.17}$$

The perturbed surface location $r(t,\theta,z)$ is substituted into (4.15a) and the equation is expanded in a series in δ. Since $\delta \ll 1$, the nonlinear terms are negligible and are subsequently dropped to yield a linear equation in δ. The perturbation is then written in the form of a normal mode:

$$\delta(t,\theta,z) = e^{\sigma t}\sin(kz)f(\theta)\,, \tag{4.18}$$

where k is the wave number in the z direction and σ is the dimensionless growth rate. The solid wire is unstable if σ is positive.

To find σ, equation (4.18) is substituted into the linearized equation, and we arrive at an eigenvalue problem:

$$c_4\frac{d^4f}{d\theta^4} + c_3\frac{d^3f}{d\theta^3} + c_2\frac{d^2f}{d\theta^2} + c_1\frac{df}{d\theta} + c_0 f - \sigma f = 0\,, \tag{4.19}$$

where c_4, c_3, c_2, c_1 and c_0 are functions of k, R, R_θ, $R_{\theta\theta}$, $R_{\theta\theta\theta}$, and $R_{\theta\theta\theta\theta}$, and are listed in Appendix C.

The periodic boundary conditions become

$$f\big|_0 = f\big|_{2\pi}\,, \tag{4.20a}$$

$$\left.\frac{df}{d\theta}\right|_0 = \left.\frac{df}{d\theta}\right|_{2\pi}, \tag{4.20b}$$

$$\left.\frac{d^2f}{d\theta^2}\right|_0 = \left.\frac{d^2f}{d\theta^2}\right|_{2\pi}, \tag{4.20c}$$

$$\left.\frac{d^3 f}{d\theta^3}\right|_0 = \left.\frac{d^3 f}{d\theta^3}\right|_{2\pi} . \qquad (4.20d)$$

4.5. Numerical Method

The eigenvalue problem (4.19) is solved by a pseudospectral method. The eigenfunction $f(\theta)$ is discretized into $\mathbf{f} = [f(\theta_j), j = 1...N]$, where θ_j are the Chebychev collocation points. Equation (4.1) then reduces to a system of algebraic equations:

$$\mathbf{A}\mathbf{f} = \sigma\mathbf{f} , \qquad (4.21a)$$

$$\mathbf{A} = \sum_{i=0}^{4} \mathbf{c}_i \mathbf{D}^i , \qquad (4.21b)$$

where $\mathbf{c}_i$ are diagonal matrices with element $c_i(\theta_j)$ at the jth row (c_i are given in Appendix C), and $\mathbf{D}$ is the differentiation matrix. The first and last two rows of $\mathbf{A}$ are replaced by the boundary conditions. With N collocation points, the pseudospectral method yields N-4 eigenvalues. When the equilibrium shape has sharp corners (P << 1), the computation is performed in the domain $0 \le \theta \le 90°$ for the square wire and $0 \le \theta \le 120°$ for the triangular wire to take advantage of symmetry. Since the Chebychev collocation points are not evenly distributed, the square is rotated by 45° such that more Chebychev points are placed in the sharp corners to increase resolution. For the triangular wire, the origin of the coordinate system is shifted to the centroid of the triangle to create a unit symmetry cell in the domain $0 \le \theta \le 120°$. However, the smaller computational domains miss a set of higher eigenmodes. Therefore, the full domain $0 \le \theta \le 360°$ is used to capture those missing eigenmodes, and consequently results for those modes are less accurate. In general, as P decreases or as the corner sharpens, more collocation points are needed to obtain the same accuracy. Results

presented below are calculated with N = 256 to 2000. By varying N, we find that the results are accurate to at least four significant digits.

The coefficients c_i depend on the equilibrium shape $R(\theta)$ and its derivatives as shown in Appendix E. However, the equilibrium shape in Section 4.3 is described by $x(\varphi)$ and $y(\varphi)$, which need to be converted to $R(\theta)$. Given a Chebychev collocation point θ_j, the corresponding normal angle φ_j is found from $x(\varphi)$ and $y(\varphi)$ in (4.9) and

$$\theta = \tan^{-1}\left(\frac{y}{x}\right). \tag{4.22}$$

Since φ varies monotonically with θ, φ_j is calculated by bisection to an accuracy of 10 decimal places. Once φ_j is determined, the radius follows as

$$R = \sqrt{x^2 + y^2}\,. \tag{4.23}$$

This is how $R(\theta)$ is calculated. Its first derivative can be written as $dR/d\theta = (dR/ds)(ds/d\theta)$. From (4.9) and (4.23),

$$\frac{dR}{ds} = \frac{\partial R}{\partial x}\frac{\partial x}{\partial s} + \frac{\partial R}{\partial y}\frac{\partial y}{\partial s} = (x^2 + y^2)^{-1/2}(-x\sin\varphi + y\cos\varphi)\,. \tag{4.24}$$

Also, from (4.8) and (4.22),

$$\frac{d\theta}{ds} = \frac{\partial \theta}{\partial x}\frac{\partial x}{\partial s} + \frac{\partial \theta}{\partial y}\frac{\partial y}{\partial s} = \frac{(x\cos\varphi + y\sin\varphi)}{x^2 + y^2}\,. \tag{4.25}$$

Thus ,

$$\frac{dR}{d\theta} = \frac{-x\sin\varphi + y\cos\varphi}{x\cos\varphi + y\sin\varphi}(x^2 + y^2)^{1/2}\,. \tag{4.26}$$

Higher derivatives $R_{\theta\theta}$, $R_{\theta\theta\theta}$, and $R_{\theta\theta\theta\theta}$ can be similarly expressed in terms of φ, x, y, … etc (Appendix D). Thus, given a chebychev collocation point θ_j, the coefficients c_i are determined.

4.6. Numerical Results

4.6.1 General Characteristics

The eigenfuction and eigenvalue depend on the equilibrium shape and the wavenumber k. Only two groups of equilibrium shapes are considered: square and triangle. Within each group, the shape is controlled by the radius of curvature P of the corner surface between two adjacent facets.

With N collocation points, N-4 eigenvalues are obtained and about a third of them turn out to be real. In general, the complex eigenvalues have larger (negative) real parts than the real ones. These complex eigenvalues are attributable to discretization errors because, as N increases, the small eigenvalues converge to values independent of N, and because the eigenvalues are shown later to be real for weak anisotropy. Thus, only real eigenvalues are presented, and they are arranged in descending order as σ_0, σ_1, σ_2, …. We find that the fundamental eigenvalue σ_0 is unique, but higher eigenvalues degenerate. For the square wire, two identical values are obtained for σ_1, σ_3, σ_5, … and two different values appear for even-numbered eigenvalues. For the triangular wire, two different values exist for σ_i, where i is a multiple of 3, and two identical values for other eigenvalues. The reason for this degeneracy will be investigated later in Section 4.7 by an asymptotic analysis. Only the first two eigenvalues σ_0 and σ_1 are ever positive. Thus, only the first two modes of perturbation can be unstable.

4.6.2 Fundamental Eigenmode

The fundamental eigenvalue σ_0 is plotted as a function of wave number k for different radius of curvature P and for square and triangular equilibrium shapes in Fig. 4.2. For each curve with fixed P, σ_0 increases quadratically with k before reaching a maximum value $\sigma_0 = \sigma_m$ at $k = k_m$. The growth rate σ_0 then decreases monotonically with k, passing through $\sigma_0 = 0$ at $k = k_c$. Results of σ_m, k_m, and k_c for different P are listed in Tables 1 and 2. The range of k in which σ_0 is positive and the magnitude of σ_0 are indicators of the stability of the system. As P decreases from unity (i.e. as the equilibrium shape deviates from a circle), σ_m will decrease first and reach a minimum value at $P = P_m$ before increasing ($P_m \approx 0.5$ for the square and $P_m = 0.93$ for the triangle). The growth rate σ_0 is plotted for $P = P_m$ for the square wire in Fig. 4.2(a), but not for the triangular wire in Fig. 4.2(b) because it is indistinguishable from P = 1 case.

The fundamental eigenfunction f_0 is plotted in Fig. 4.3 for different P. The eigenfunctions are computed for $k = k_m$, the wavenumber at which σ_0 is maximum. This particular wavenumber is chosen because it is likely the wavenumber of the particles after breakup of the wire, and the corresponding eigenfunction probably will determine the perturbed wire shape at late times. When P = 1(i.e., when the equilibrium shape is cirular), f_0 is constant. When P < 1, f_0 has four-fold symmetry for the square wire in Fig. 4.3(a), and three-fold symmetry for the triangular wire in Fig. 4.3(b). When P << 1, i.e. when the corners of the equilibrium shape become sharp, sharp peaks also appear in f_0 at the corner positions. The reason for these peaks is revealed when the eigenfunctions are superimposed onto the equilibrium shapes in Figs. 4.4 and 4.5. In

both figures, the perturbed wires retain the same cross-sectional shapes as the equilibrium ones. The sharp peaks in the eigenfuctions are needed to maintain the corners of the perturbed shapes sharp. Note that the cross-sectional area of the perturbed wire vary sinusoidally along the z–direction.

4.6.3 First Eigenmode

The first eigenmode has two identical eigenvalues σ_1 and two different eigenfunctions, one for each eigenvalue. The eigenvalue is plotted as a function of wavenumber k in Fig. 4.6 for different P. It shows that σ_1 decreases quadratically with k. For P = 1, $\sigma_1 = 0$ at k = 0. For P = 0.5 (square wire) and 0.7 (triangular wire), $\sigma_1 > 0$ for $0 \le k < k_{1c}$, and the maximum point of σ_1 occurs at k = 0 and is denoted by $\sigma_1 = \sigma_{1m}$. Results of σ_{1m} and k_{1c} are listed in Tables 1 and 2.

The first eigenmode has two eigenfunctions: f_{11} and f_{12}, which are plotted in Fig. 4.7 for $k = k_{1c} = 0.402$ for the square wire and $k = k_{1c} = 0.424$ for the triangular wire. When P = 1, the equilibrium shape is a circle and $f_{11} = \sin\theta$ and $f_{12} = \cos\theta$. When $P < 1$, f_{11} remains skew-symmetric and f_{12} symmetric about $\theta = 180°$. Furthermore, for the square wire f_{11} shows additional symmetry and f_{12} skew-symmetry about $\theta = 90°$ and $270°$, but no other symmetry can be found for f_{11} and f_{12} of the triangular wire. The effect of these eigenfunctions is revealed by superimposing them onto the equilibrium shape in Fig. 4.8. It shows that f_{11} shifts the wire vertically and f_{12} horizontally. The first eigenmode is a linear combination of these two eigenfunctions; their combined effect is to perturb the wire helically along the axis but with no twisting.

4.6.4 Higher Eigenmodes

The eigenvalues σ_2 and σ_3 of the second and third eigenmodes are plotted as a function of wave number k for different radius of curvature P in Fig. 4.9 for the square wire and in Fig. 4.10 for the triangular wire. In all the cases, the eigenvalue decreases as k increases with P fixed. The eigenvalues are always negative, so that the perturbations are stable. The eigenvalue σ_2 for the square wire and σ_3 for the triangular wire split into two branches as P decreases from unity. One branch is higher and one lower than the P =1 case at constant k. The other eigenvalues (σ_3 for the square and σ_2 for the triangle) also degenerate, but they yield two identical numbers that are smaller than the P = 1 case. Figure 4.11 shows eigenfunctions f_{21} and f_{22} corresponding to eigenvalues σ_{21} and σ_{22} for the square and triangular wires depicted in Figs. 4.9 and 4.10. When P = 1, the equilibrium shape is a circle, and $f_{21} = \sin 2\theta$ and $f_{22} = \cos 2\theta$. When P < 1, the eigenfunctions f_{21} and f_{22} for the square wire are periodic with period $180°$. In addition, f_{21} is skew-symmetric and f_{22} symmetric about $\theta = 90°$. However, for the triangular wire, f_{21} and f_{22} both have period $360°$, and f_{21} is skew-symmetric and f_{22} symmetric about $\theta = 180°$.

The effects of eignfuctions f_{21} and f_{22} on the equilibrium shapes are shown in Fig. 4.12. For the square wire (Fig. 4.12(a)), f_{21} compresses the square into a rectangle, whereas f_{22} squeezes from two opposite corners to make the square into a diamond. For the triangular wire (Fig. 4.12(b)), f_{21} flatens the triangle from the top corner toward the opposing side, whereas f_{22} squeezes the triangle vertically from two corners.

Fig. 4.12 shows eigenfuctions f_{31} and f_{32} corresponding to eigenvalues σ_{31} and σ_{32} plotted in Figs. 4.9 and 4.10. When P = 1, the equilibrium shape is a circle, and $f_{31} = \sin 3\theta$ and $f_{32} = \cos 3\theta$. When P < 1, for the square wire, f_{31} is skew-symmetric and f_{32} symmetric about $\theta = 180°$, whereas for the triangular wire, both f_{31} and f_{32} have period $120°$, with f_{31} skew-symmetric and f_{32} symmetric about $\theta = 60°$. Steady and perturbed wire shapes are plotted in Fig. 4.14. For the square wire, f_{31} pushes in the bottom two sides and flatens the top corner, and f_{32} does the same to the square except that it is rotated $90°$. For the triangular wire, f_{31} twists the wire counter-clockwise, whereas f_{32} pushes in the sides to extend the corners.

4.7. An Asymptotic Solution for Weak Anisotropy

An asymptotic solution is found in the limit of zero anisotropy for the square wire. The triangular wire is not as suitable because of the uncertainty in the location of the center. The asymptotic analysis explains the appearance of degeneracy in the eigenvalues calculated by the numerical method. When the surface energy is isotropy, P = 1 and the wire is circular. As P decreases, the wire begins to deviate from circularity. For $1 \le P \le 0.92$, we fit the wire shape by a Fourier series:

$$R = C_0 + C_4\cos(4\theta) + C_8\cos(8\theta) + C_{12}\cos(12\theta) \ . \qquad (4.27)$$

The coefficients C_0, C_4, C_8 and C_{12} are plotted as a function of (1-P) and fitted by a second order polynomial. By keeping only the linear terms, we find

$$R(\theta) = 1 + \varepsilon[1 - \alpha\cos(4\theta)] \ , \qquad (4.28a)$$

$$\alpha = 0.7441 \ , \qquad (4.28b)$$

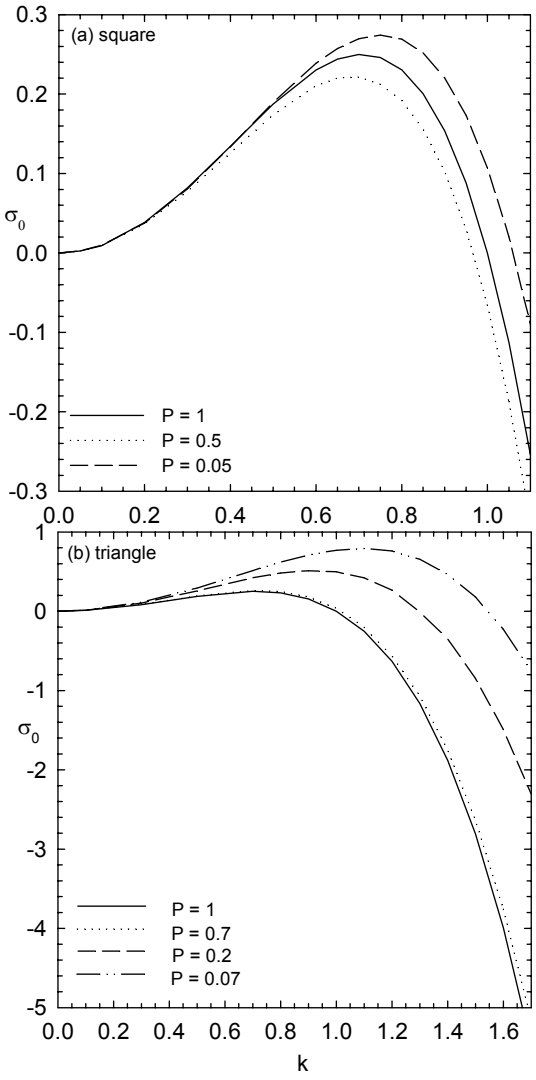

Fig. 4.2. The fundamental eigenvalue σ_0 versus wave number k for different radius of curvature P for (a) square and (b) triangular equilibrium shapes.

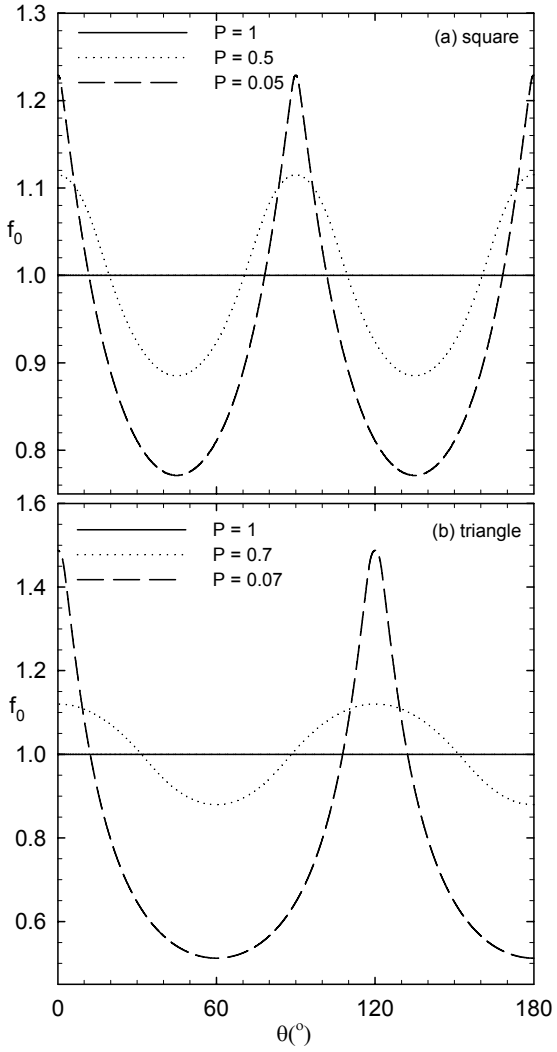

Fig. 4.3. The fundamental eigenfunction f_0 for $k = k_m$ and different P for (a) square and (b) triangular equilibrium shapes. The eigenfunctions are symmetric about $\theta = 180°$.

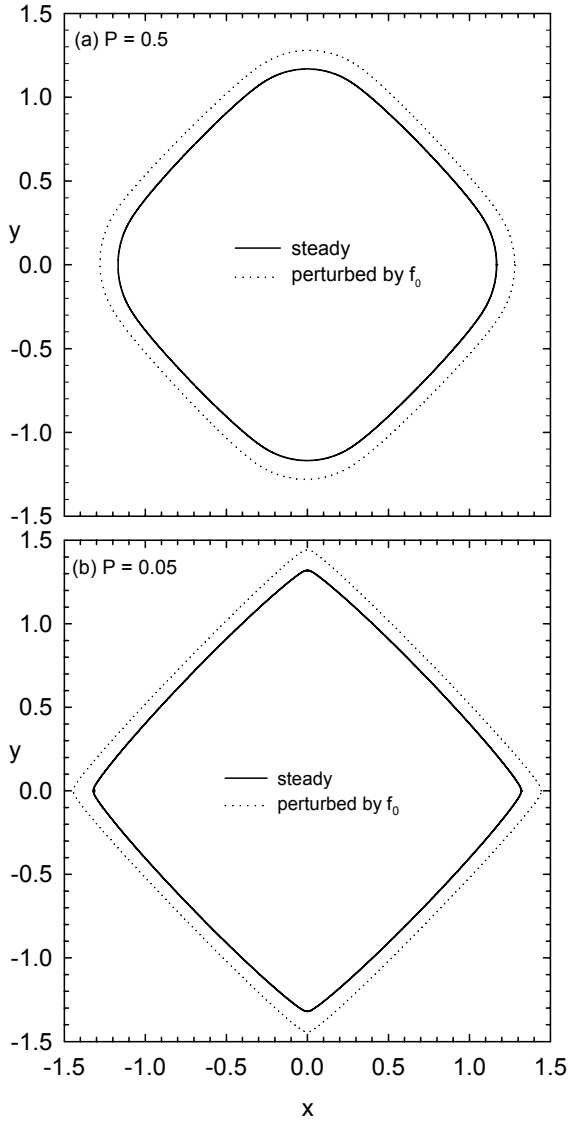

Fig. 4.4. Square wires perturbed by the eigenfuncition f_0 in Fig. 3(a). The cross-sectional area of the perturbed wire varies sinusoidally in the axial direction about the equilibrium value.

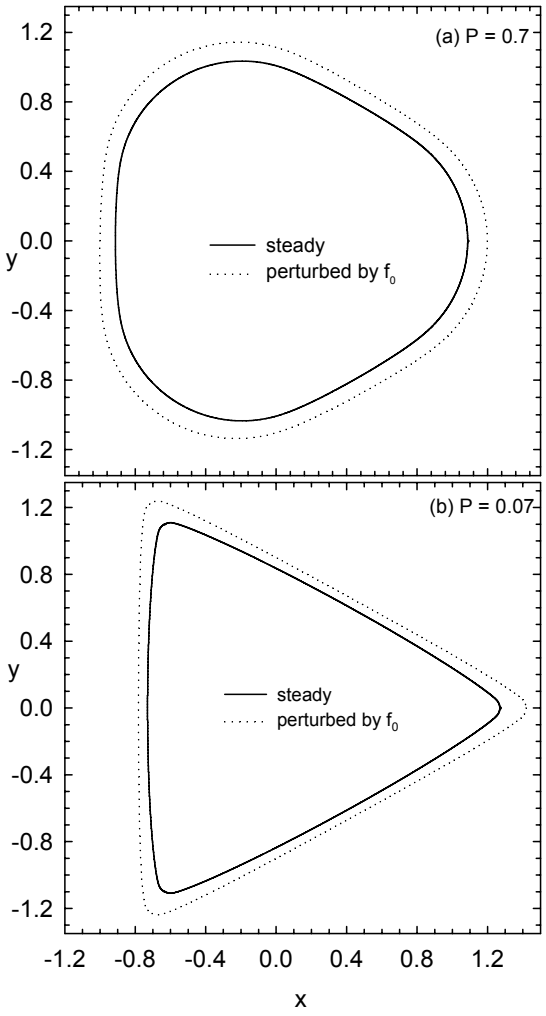

Fig. 4.5. Triangular wires perturbed by the eigenfuncition f_0 in Fig. 3(b). The cross-sectional area of the perturbed wire varies sinusoidally in the axial direction about the equilibrium value.

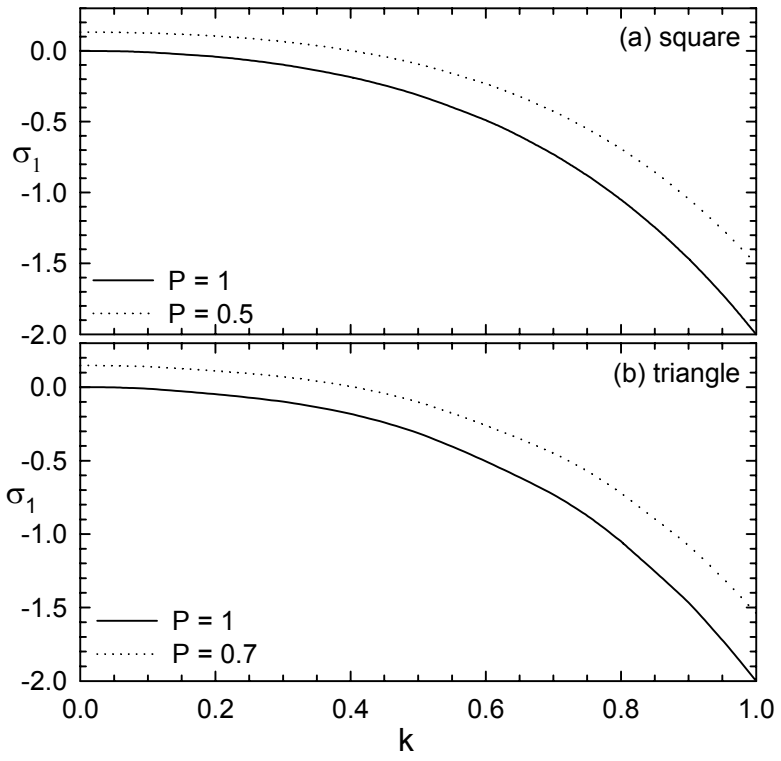

Fig. 4.6. Eigenvalue σ_1 of the first eigenmode versus wave number k for different radius of curvature P and different equilibrium shapes.

Table 4.1 Numerical results for the square wire made dimensionless by R_0

P	L	A_c	k_m	σ_m	k_c	k_{1c}	σ_{1m}
1	0	3.141593	0.707	0.250	1.000	0	0
0.5	6.033860	3.650013	0.683	0.221	0.967	0.402	0.1319
0.35	7.844018	3.747482	0.688	0.228	0.971	0.522	0.1883
0.05	11.464334	3.866186	0.750	0.274	1.060	-	-

Table 4.2 Numerical results for the triangular wire made dimensionless by R_0 .

P	L	A_c	k_m	σ_m	k_c	k_{1c}	σ_{1m}
1	0	3.141593	0.707	0.250	1.000	0	0
0.93	0.998688	3.166997	0.705	0.248	0.998	0.00502	0.00901
0.7	4.280090	3.174530	0.720	0.261	1.020	0.424	0.147
0.2	11.313574	2.789188	0.924	0.510	1.296	-	-
0.07	13.268280	2.598861	1.092	0.790	1.548	-	-

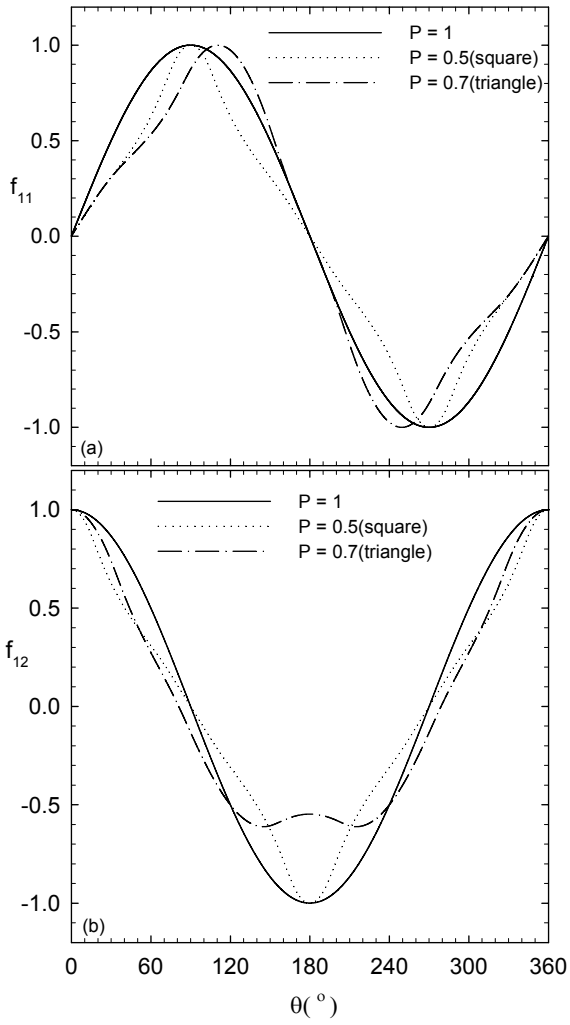

Fig. 4.7. Eigenfunctions f_{11} and f_{12} of the first eigenmode at $k = k_c$ for different radius of curvature P and different equilibrium shapes.

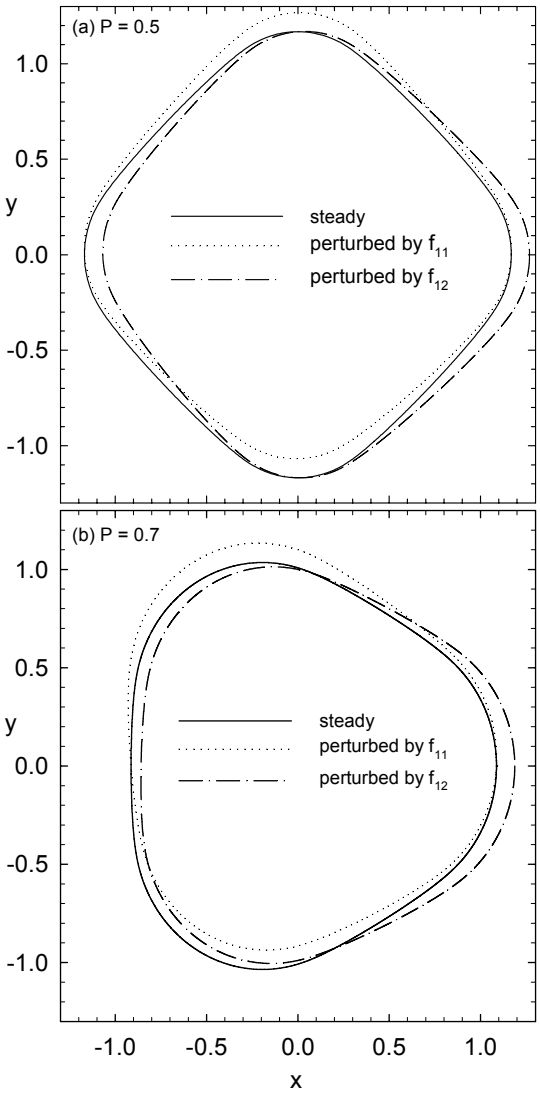

Fig. 4.8. Equilibrium and perturbed wire shapes. The eigenfunctions f_{11} and f_{12} are graphed in Fig. 4.7. The combined effect of the eigenfuctions is to perturb the wire helically along the axis but with no twisting.

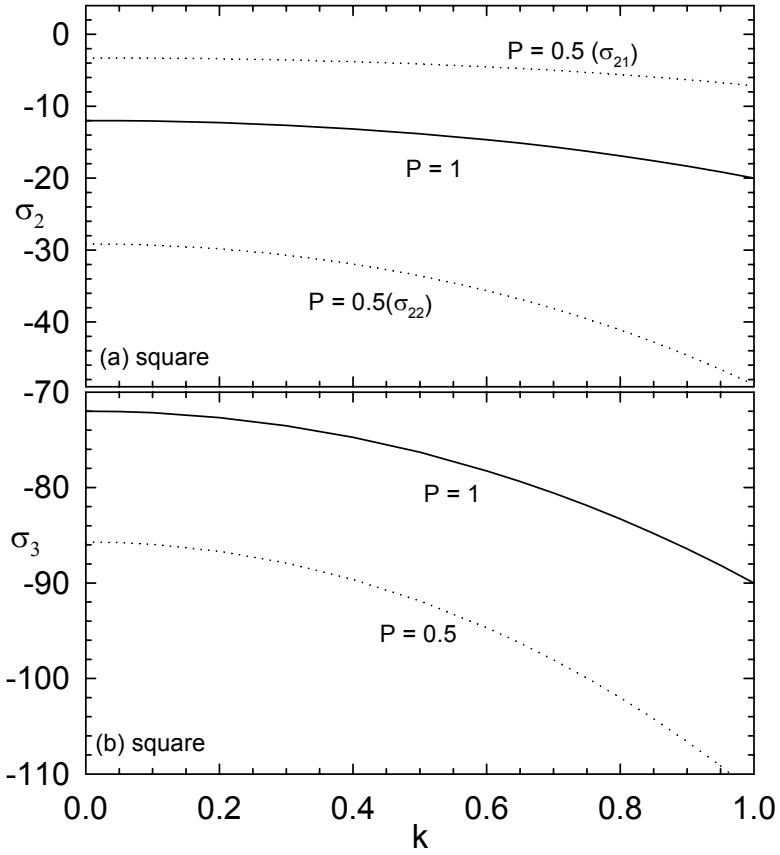

Fig. 4.9. Eigenvalues σ_2 and σ_3 of the second and third eigenmode for the square wire as a function of wave number k for different radius of curvature P. The eigenvalues degenerate into two branches as P decreases from unity; σ_2 yields two different values (σ_{21} and σ_{22}) and σ_3 two identical values.

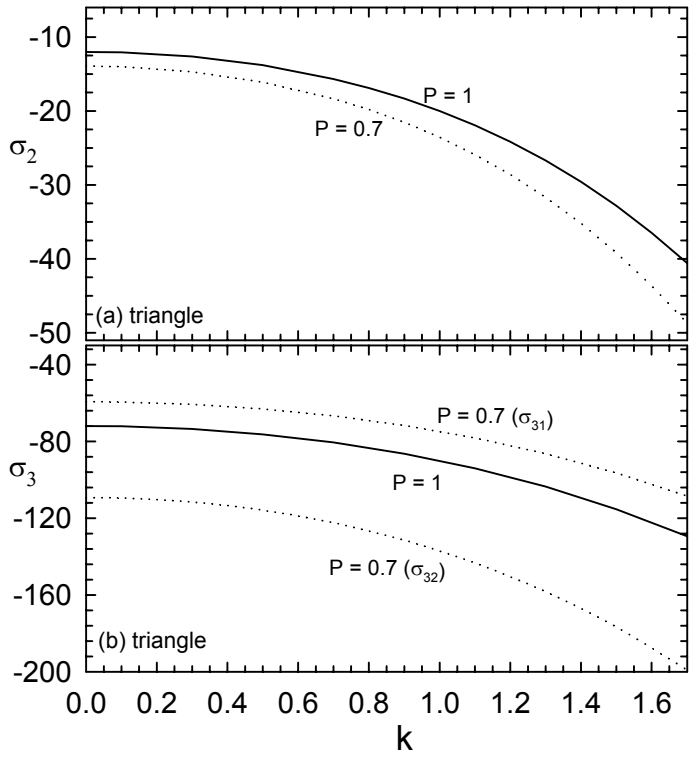

Fig. 4.10. Fig 10 Eigenvalues σ_2 and σ_3 of the second and third eigenmode for the triangular wire as a function of wave number k for different radius of curvature P. The eigenvalues degenerate into two branches as P decreases from unity; σ_3 yields two different values (σ_{31} and σ_{32}) and σ_2 two identical values.

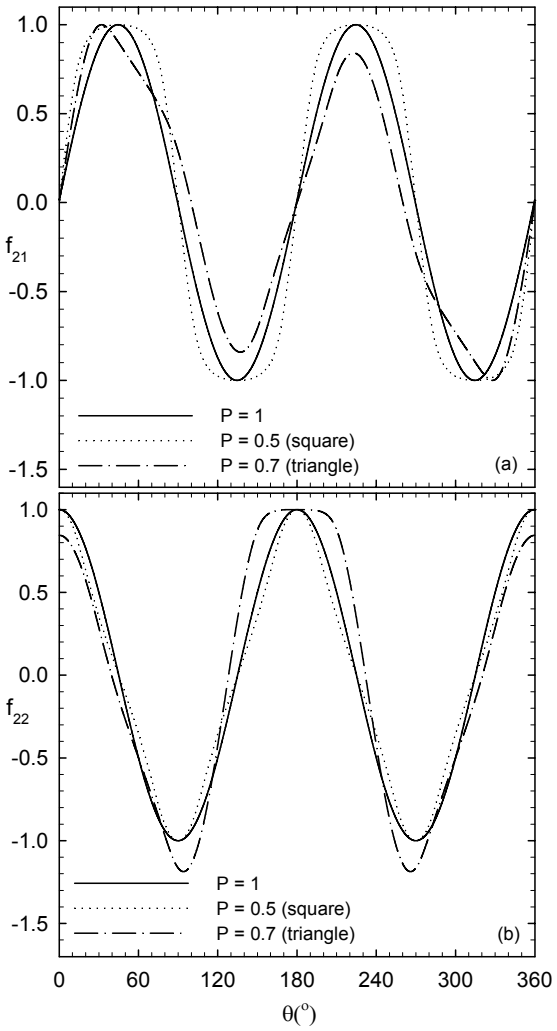

Fig. 4.11. Eigenfunctions f_{21} and f_{22} correspondign to eigenvalues σ_{21} and σ_{22} shown in Figs. 4.9 and 4.10 for square and triangular wires. The eigenfunctions for the square and triangular wires have different symmetries.

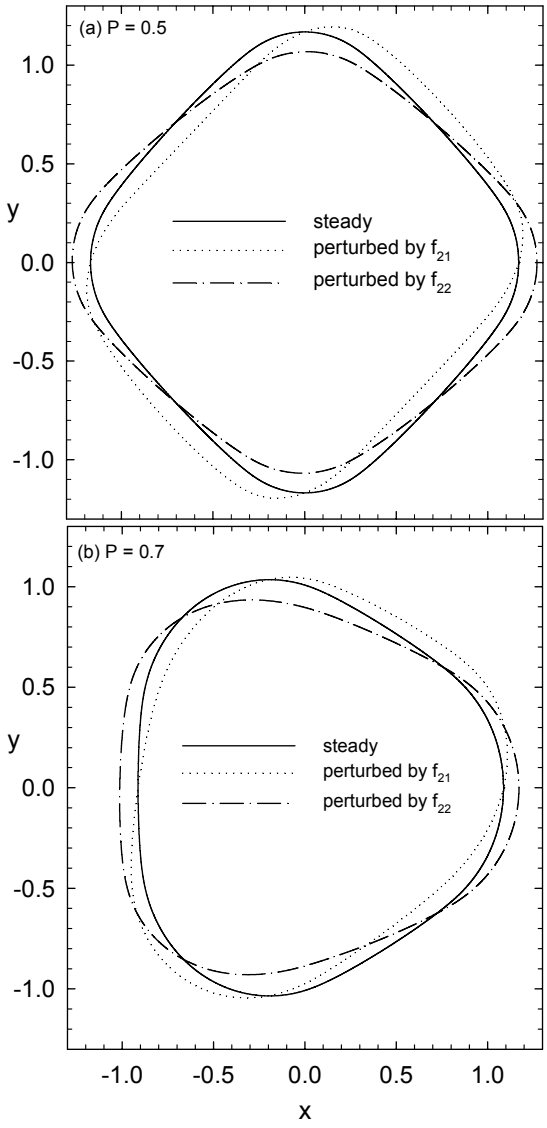

Fig. 4.12. Equilibrium and perturbed wire shapes. The eigenfunctions f_{21} and f_{22} are graphed in Fig. 4.11. The combined effect of the eigenfuctions is to pinch the wire sinusoidally along the axis.

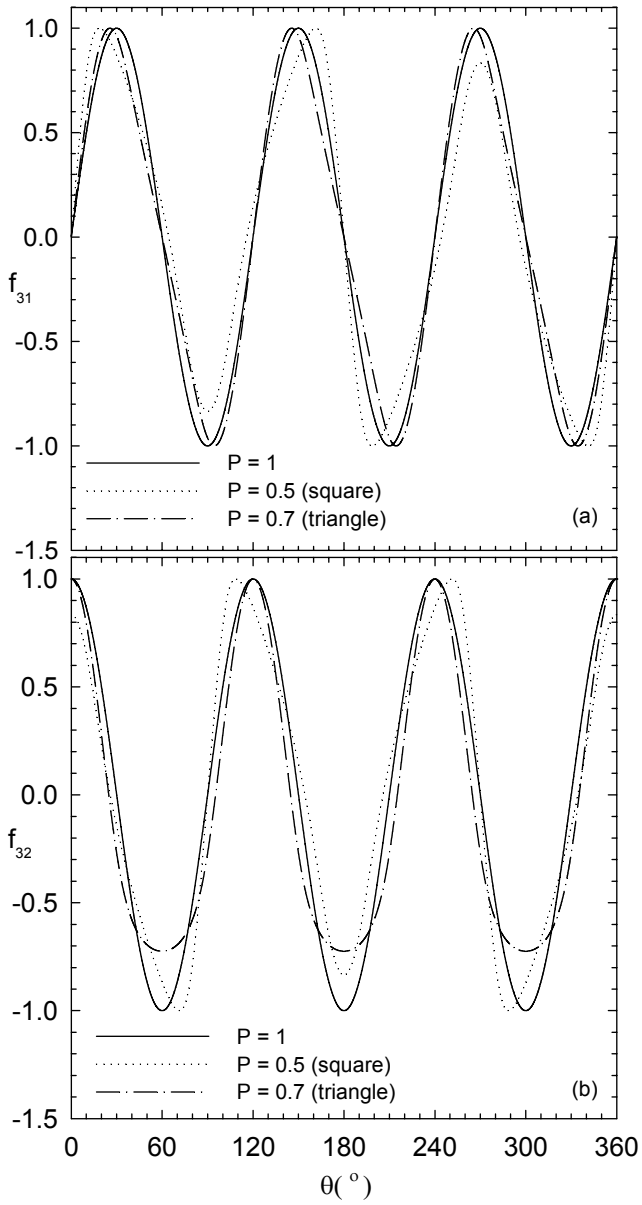

Fig. 4.13. Eigenfunctions f_{31} and f_{32} corresponding to eigenvalues σ_{31} and σ_{32} shown in Figs. 4.9 and 4.10 for square and triangular wires. The eigenfunctions for square and triangular wires have different symmetries.

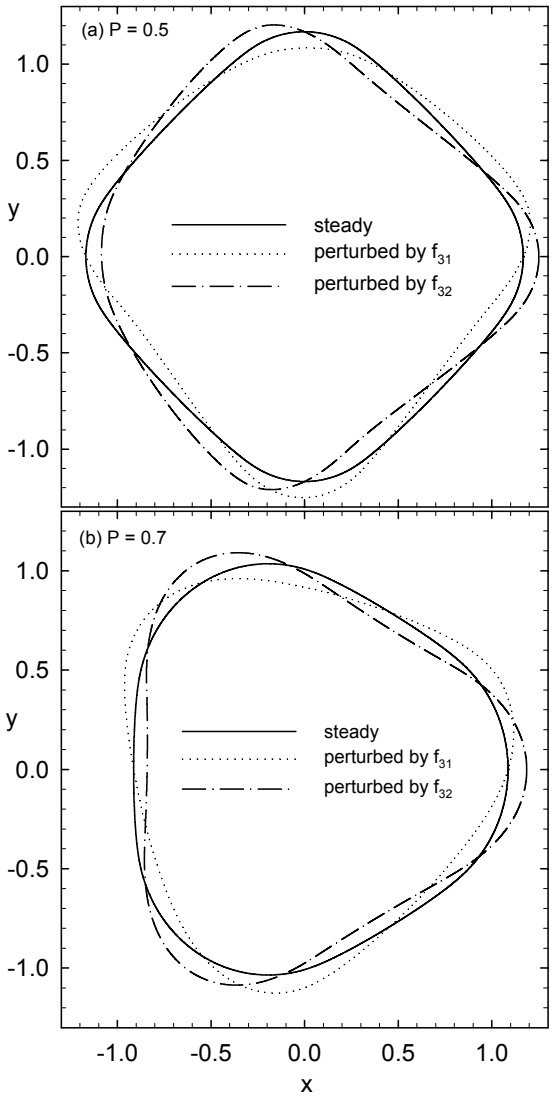

Fig. 4.14. Equilibrium and perturbed wire shapes. The eigenfunctions f_{31} and f_{32} are graphed in Fig. 4.13. Although the effect of individual eigenfunction is clear, their combined behavior is not obvious.

$$\varepsilon = 0.2067(1-P)\,, \tag{4.28c}$$

where the higher-order Fourier expansions have been dropped. If the surface energy is isotropic, P = 1 and thus $\varepsilon = 0$. Hence, ε is a measure of deviation from isotropy, and we seek an asymptotic solution in the limit $\varepsilon \to 0$. (Note that $R(0) \neq 1$ in (4.28a) because the Fourier expansion fits the cross-sectional area and not the surface location at $\theta = 0$.)

The equilibrium shape is perturbed by a small disturbance:

$$r(t,\theta,z) = 1 + \varepsilon[1 - \alpha\cos(4\theta)] + \delta(t,\theta,z)\,, \tag{4.29}$$

and the disturbance is written in the form of a nomal mode as

$$\delta(t,\theta,z) = e^{\sigma t}\sin(kz)F(\theta)\,. \tag{4.30}$$

To find the growth rate σ, equation (4.29) is substituted into the governing equation (4.4) and expanded to second order in ε. We arrive at an eigenvalue problem:

$$b_4\frac{d^4F}{d\theta^4} + b_3\frac{d^3F}{d\theta^3} + b_2\frac{d^2F}{d\theta^2} + b_1\frac{dF}{d\theta} + b_0F - \sigma F = 0\,, \tag{4.31a}$$

$$b_i = \varepsilon^2 b_{i2} + \varepsilon b_{i1} + b_{i0}\,,\ i = 0,1,2,3,4 \tag{4.31b}$$

where $b_{ij} = b_{ij}(k,\theta)$ are listed in Appendix E. The eigenfuction F is subject to periodic boundary conditions as in (4.20) with function f replaced by F.

The eigenvalue problem (4.31) is solved by expanding the eigenfunction and eigenvalue:

$$F(\theta) = F_0(\theta) + \varepsilon F_1(\theta) + \varepsilon^2 F_2(\theta) + \ldots\,, \tag{4.32}$$

$$\sigma = \Sigma_0 + \varepsilon\Sigma_1 + \varepsilon^2\Sigma_2 + \ldots\,. \tag{4.33}$$

Substituting into (4.31) and collecting terms of the same order in ε yields

$$b_{40}\frac{d^4F_0}{d\theta^4} + b_{20}\frac{d^2F_0}{d\theta^2} + (b_{00} - \Sigma_0)F_0 = 0\,, \tag{4.34a}$$

$$b_{40}\frac{d^4F_1}{d\theta^4}+b_{20}\frac{d^2F_1}{d\theta^2}+(b_{00}-\Sigma_0)F_1=\Sigma_1F_0+T_1\,, \tag{4.34b}$$

$$b_{40}\frac{d^4F_2}{d\theta^4}+b_{20}\frac{d^2F_2}{d\theta^2}+(b_{00}-\Sigma_0)F_2=\Sigma_2F_0+T_2\,, \tag{4.34c}$$

$$T_1=-b_{41}\frac{d^4F_0}{d\theta^4}-b_{31}\frac{d^3F_0}{d\theta^3}-b_{21}\frac{d^2F_0}{d\theta^2}-b_{11}\frac{dF_0}{d\theta}-b_{01}F_0\,, \tag{4.34d}$$

$$\begin{aligned}T_2=&-b_{41}\frac{d^4F_1}{d\theta^4}-b_{31}\frac{d^3F_1}{d\theta^3}-b_{21}\frac{d^2F_1}{d\theta^2}-b_{11}\frac{dF_1}{d\theta}-b_{01}F_1\\&-b_{42}\frac{d^4F_0}{d\theta^4}-b_{32}\frac{d^3F_0}{d\theta^3}-b_{22}\frac{d^2F_0}{d\theta^2}-b_{12}\frac{dF_0}{d\theta}-b_{02}F_0+\Sigma_1F_1\,.\end{aligned} \tag{4.34e}$$

Note that b_{40} , b_{20} , and b_{00} depend only on k, as shown in Appendix E. The eigenfuctions F_i , i = 0, 1, 2, obey the following periodic boundary conditions:

$$F_i\big|_0=F_i\big|_{2\pi}\,, \tag{4.35a}$$

$$\left.\frac{dF_i}{d\theta}\right|_0=\left.\frac{dF_i}{d\theta}\right|_{2\pi}\,, \tag{4.35b}$$

$$\left.\frac{d^2F_i}{d\theta^2}\right|_0=\left.\frac{d^2F_i}{d\theta^2}\right|_{2\pi}\,, \tag{4.35c}$$

$$\left.\frac{d^3F_i}{d\theta^3}\right|_0=\left.\frac{d^3F_i}{d\theta^3}\right|_{2\pi}\,. \tag{4.35d}$$

Analytic solutions are found for the asymptotic expansions of eigenfunction and eigenvalue.

The leading-order eigenfunction F_0 satisfies the linear equation (4.34a) with constant coefficients. Therefore, a general solution is

$$F_0=e^{q\theta}\,, \tag{4.36a}$$

$$q^2 = \frac{-b_{20} \pm \sqrt{b_{20}^2 - 4b_{40}(b_{00} - \sigma_0)}}{2b_{40}}. \qquad (4.36b)$$

The periodic boundary conditions require

$$q = \pm ni, \; n = 0, 1, 2, \ldots, \qquad (4.37)$$

where $i = \sqrt{-1}$ only here. Equating (4.36b) and (4.37) yields

$$\Sigma_0 = (k^2 + n^2)(1 - n^2 - k^2). \qquad (4.38)$$

This agrees with Mullins's expression in (4.3) for a circular cylindrical wire. The leading-order eigenfunction F_0 has two independent solutions F_0^1 and F_0^2 that satisfy the boundary conditions in (4.30):

$$F_0^1 = \sin n\theta, \qquad (4.39a)$$

$$F_0^2 = \cos n\theta. \qquad (4.39b)$$

These two solutions generate two branches in higher-order expansions.

The first-order expansions F_1 and Σ_1 are found following the standard technique. The homogeneous part of F_1 satisfies the same equation as F_0 and therefore has the same solution. To get Σ_1, multiply both sides of (7.8b) by $d^2F_0/d\theta^2$, and integrate from 0 to 2π to yield

$$b_{40}\int_0^{2\pi} \frac{d^4F_1}{d\theta^4}\frac{d^2F_0}{d\theta^2}d\theta + b_{20}\int_0^{2\pi} \frac{d^2F_1}{d\theta^2}\frac{d^2F_0}{d\theta^2}d\theta + (b_{00} - \Sigma_0)\int_0^{2\pi} F_1\frac{d^2F_0}{d\theta^2}d\theta = \int_0^{2\pi} (\Sigma_1 F_0 + T_1)\frac{d^2F_0}{d\theta^2}d\theta. \qquad (4.40)$$

By using integration by parts and the periodic boundary conditions, the left side of (4.40) can be rearranged as

$$\int_0^{2\pi} \frac{d^2F_1}{d\theta^2}[b_{40}\frac{d^4F_0}{d\theta^4} + b_{20}\frac{d^2F_0}{d\theta^2} + (b_{00} - \Sigma_0)F_0]d\theta = \int_0^{2\pi} (\Sigma_1 F_0 + T_1)\frac{d^2F_0}{d\theta^2}d\theta . \qquad (4.41)$$

The left side vanishes according to (4.34a), so that

$$\Sigma_1 = -\int_0^{2\pi} T_1 \frac{d^2F_0}{d\theta^2}d\theta \Big/ \int_0^{2\pi} F_0 \frac{d^2F_0}{d\theta^2}d\theta \ . \qquad (4.42)$$

Since there are two branches of F_0, Σ_1 also has two branches. Substitution of

$F_0 = F_0^1 = \text{sinn}\theta$ into (4.42) yields

$$\Sigma_1^1 = L_1 + (L_2 \int_0^{2\pi} \sin^2 n\theta \cos 4\theta \, d\theta - L_3 \int_0^{2\pi} \text{sinn}\theta \, \text{cosn}\theta \sin 4\theta \, d\theta) \Big/ \int_0^{2\pi} \sin^2 n\theta \, d\theta , \qquad (4.43)$$

$$L_1 = 3n^4 - (3 - 2k^2)n^2 - k^2(k^2 + 1) , \qquad (4.44a)$$

$$L_2 = -\alpha[19\, n^4 + (34\, k^2 + 317)n^2 + 15(k^2 + 16)(k^2 + 1)] , \qquad (4.44b)$$

$$L_3 = 144\alpha\, n^3 + 20(9\alpha + 7\, k^2)n , \qquad (4.44c)$$

where it is assumed $n \neq 0$. The integrals in the numerator vanish if $n \neq 2$. Thus,

$$\Sigma_1^1 = L_1 , \text{ if } n \neq 2, \qquad (4.45a)$$

$$\Sigma_1^1 = L_1 + \frac{1}{2}(L_2 + L_3) , \text{ if } n = 2. \qquad (4.45b)$$

The second branch of Σ_1 is found by substitution of $F_0 = F_0^2 = \text{cosn}\theta$ into (4.42):

$$\Sigma_1^2 = L_1 + (L_2 \int_0^{2\pi} \cos^2 n\theta \cos 4\theta \, d\theta + L_3 \int_0^{2\pi} \text{sinn}\theta \, \text{cosn}\theta \sin 4\theta \, d\theta) \Big/ \int_0^{2\pi} \cos^2 n\theta \, d\theta . \qquad (4.46)$$

Thus,

$$\Sigma_1^2 = L_1 , \text{ if } n \neq 2. \qquad (4.47a)$$

$$\Sigma_1^2 = L_1 - \frac{1}{2}(L_2 + L_3) , \text{ if } n = 2. \qquad (4.47b)$$

Hence, the first-order eigenvalue Σ_1 has two branches, and each branch is divided into two cases depending on n.

The first-order eigenfunction F_1 obeys (4.34b) and has a homogeneous and a particular part. The homogeneous part is the same as F_0 because it satisfies the same governing equation. The particular part depends on the source term on the right side of (4.34b). Since the source term is a function of F_0 and Σ_1, the particular part also has two branches. The first branch gives the source term as

$$\Sigma_1 F_0 + T_1 = -\frac{1}{2}(L_2 - L_3)\sin(n+4)\theta - \frac{1}{2}(L_2 + L_3)\sin(n-4)\theta \text{, if } n \neq 0, 2, \tag{4.48a}$$

$$\Sigma_1 F_0 + T_1 = -\frac{1}{2}(L_2 - L_3)\sin(n+4)\theta \text{, if } n = 2. \tag{4.48b}$$

Thus,

$$F_1^1 = Q_1 \sin[(n+4)\theta] + Q_2 \sin[(n-4)\theta] \text{, if } n \neq 0, 2, \tag{4.49a}$$

$$F_1^1 = Q_1 \sin[(n+4)\theta] \text{, if } n = 2, \tag{4.49b}$$

where

$$Q_1 = -\frac{L_2 - L_3}{2L_4}, \tag{4.50a}$$

$$Q_2 = -\frac{L_2 + L_3}{2L_5}, \tag{4.50b}$$

$$L_4 = -(n+4)^4 - (2k^2 - 1)(n+4)^2 + k - \Sigma_0, \tag{4.50c}$$

$$L_5 = -(n-4)^4 - (2k^2 - 1)(n-4)^2 + k - \Sigma_0. \tag{4.50d}$$

The second branch gives the right side of (4.34b) as

$$\Sigma_1 F_0 + T_1 = -\frac{1}{2}(L_2 - L_3)\cos(n+4)\theta - \frac{1}{2}(L_2 + L_3)\cos(n-4)\theta \text{, if } n \neq 2, \tag{4.51a}$$

$$\Sigma_1 F_0 + T_1 = -\frac{1}{2}(L_2 - L_3)\cos(n+4)\theta \text{, if } n = 2. \quad (4.51b)$$

Thus,

$$F_1^2 = Q_1\cos[(n+4)\theta] + Q_2\cos[(n-4)\theta], \text{ if } n \neq 2, \quad (4.52a)$$

$$F_1^2 = Q_1\cos[(n+4)\theta], \text{ if } n = 2. \quad (4.52b)$$

This completes the first-order expansions.

The second-order expansions Σ_2 and F_2 can be found following the same procedure as that for Σ_1 and F_1 (see Appendix E for details). There are again two branches: Σ_2^1 and Σ_2^2, and F_2^1 and F_2^2. It is observed that $\Sigma_2^1 = \Sigma_2^2$ if $n \neq 2$ or 4, and Σ_2^1 is undefined if n = 0 so that only one branch remains for the fundamental mode.

From the above asymptotic solutions, we can infer the general behavior of Σ_m for $m \geq 1$. It has two branches: Σ_m^1 and Σ_m^2, which have the same value except when m = 2, 4, 6, …, 2m. They differ because of coupling between the perturbation modes and the equilibrium wire shape. Since Σ_m has two branches, the nth eigenvalue σ_n also has two branches:

$$\sigma_{n1} = \Sigma_0 + \varepsilon\Sigma_1^1 + \varepsilon^2\Sigma_2^1 + \ldots + \varepsilon^m\Sigma_m^1 + \ldots, \quad (4.53a)$$

$$\sigma_{n2} = \Sigma_0 + \varepsilon\Sigma_1^2 + \varepsilon^2\Sigma_2^2 + \ldots + \varepsilon^m\Sigma_m^2 + \ldots. \quad (4.53b)$$

where the asymptotic expansions depend on n and k.

From the behavior of Σ_m, we can conclude that $\sigma_{n1} = \sigma_{n2}$ if n is odd. If n = 2m, m = 1, 2, 3, …, then $\sigma_{(2m)1}$ and $\sigma_{(2m)2}$ remain the same for $\Sigma_1, \Sigma_2, \ldots, \Sigma_{m-1}$, and they start to diverge from Σ_m, which is at $O(\varepsilon^m)$. Thus, to see the difference between $\sigma_{(2m)1}$ and

$\sigma_{(2m)2}$, the asymptotic expansion must be carried out to at least $O(\varepsilon^m)$. Hence, the difference between $\sigma_{(2m)1}$ and $\sigma_{(2m)2}$ decreases as m increases.

The asymptotic eigenvalues are compared with the numerical results in Figs. 4.15-4.17. The fundamental eigenvalue has only one branch because when n = 0, Σ_1^1 and Σ_2^1 are undefined. Thus,

$$\sigma_0 = \Sigma_0\big|_{n=0} + \varepsilon\Sigma_1^2\big|_{n=0} + \varepsilon^2\Sigma_2^2\big|_{n=0}. \tag{4.54}$$

For a fixed ε or P, σ_0 is only a function of k. Comparison of this function is excellent between asymptotic and numerical solution for $\varepsilon << 1$. To see how they diverge, we fix k = $1/\sqrt{2}$ (which is the value of k_m for $\varepsilon = 0$), and vary ε (or P) in Fig. 4.15. It shows that the two predictions agree well when (1-P)<<1.

The first eigenvalue σ_1 has two branches with the same value:

$$\sigma_1 = \Sigma_0\big|_{n=1} + \varepsilon\Sigma_1\big|_{n=1} + \varepsilon^2\Sigma_2\big|_{n=1}. \tag{4.55}$$

In Fig. 4.16, we plot σ_1 versus (1-P) for k = 0. This k corresponds to the maximum value of σ_1. The comparison between asymptotic and numerical calculations improves as (1-P) $\to 0$. Fig. 4.16 also shows that σ_1 increases quadratically with (1-P). This is because from (4.44a) and (4.47a), $\Sigma_1 = 3n^4 - (3-2k^2)n^2 - k^2(k^2+1) = 0$ if n = 1 and k = 0.

The second and third eigenvalue σ_2 and σ_3 are plotted as a function of (1-P) in Fig. 4.17 for k = $1/\sqrt{2}$. The second eigenvalue σ_2 has two branches and their values begin to diverge as (1-P) increases. The third eigenvalue σ_3 has two branches with the same value. The asymptotic and numerical predictions agree well as (1-P) $\to$ 0.

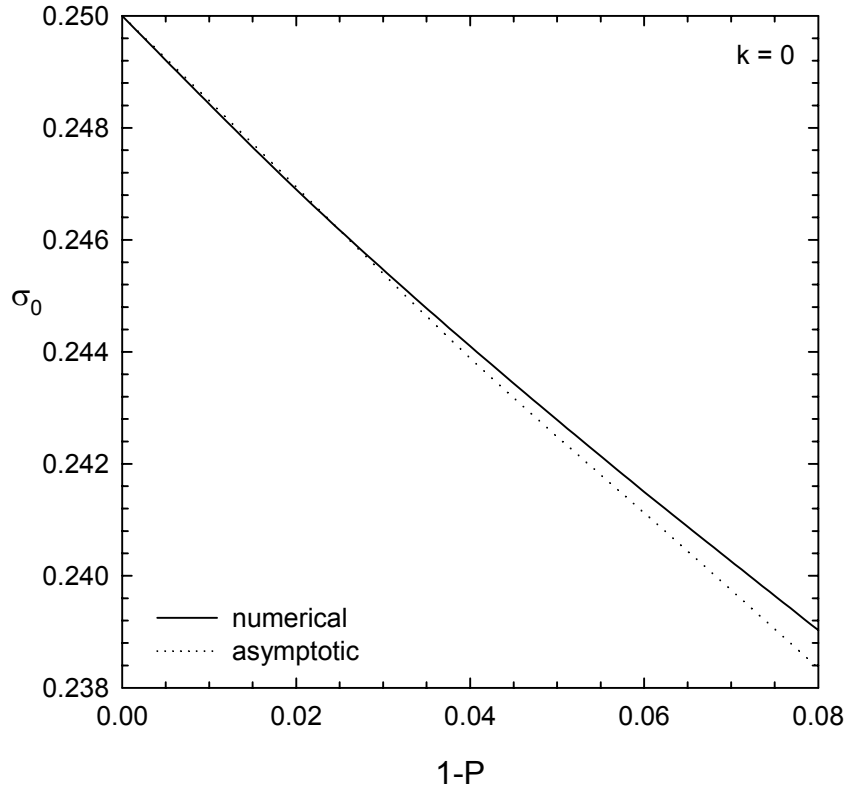

Fig. 4.15. The eigenvalue σ_0 versus (1-P) at k = $1/\sqrt{2}$ for the square wire. This value of k is k_m for P = 1. The asymptotic solution is listed in (4.54).

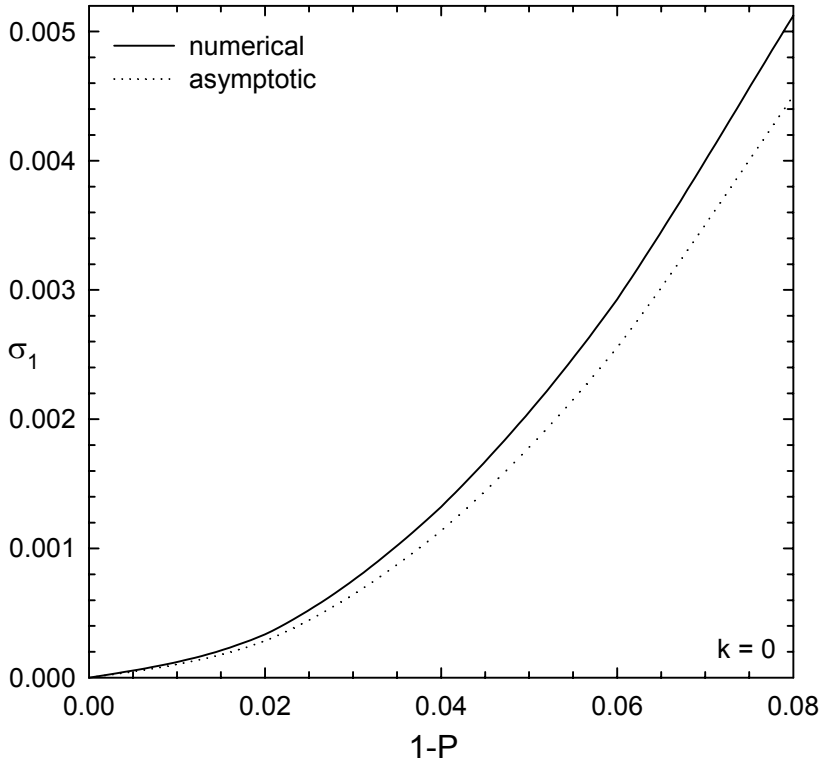

Fig. 4.16. The eigenvalue σ_1 versus (1-P) at k = 0 for the square wire. This value of k corresponds to the maximum value of σ_1. The asymptotic solution is listed in (4.55).

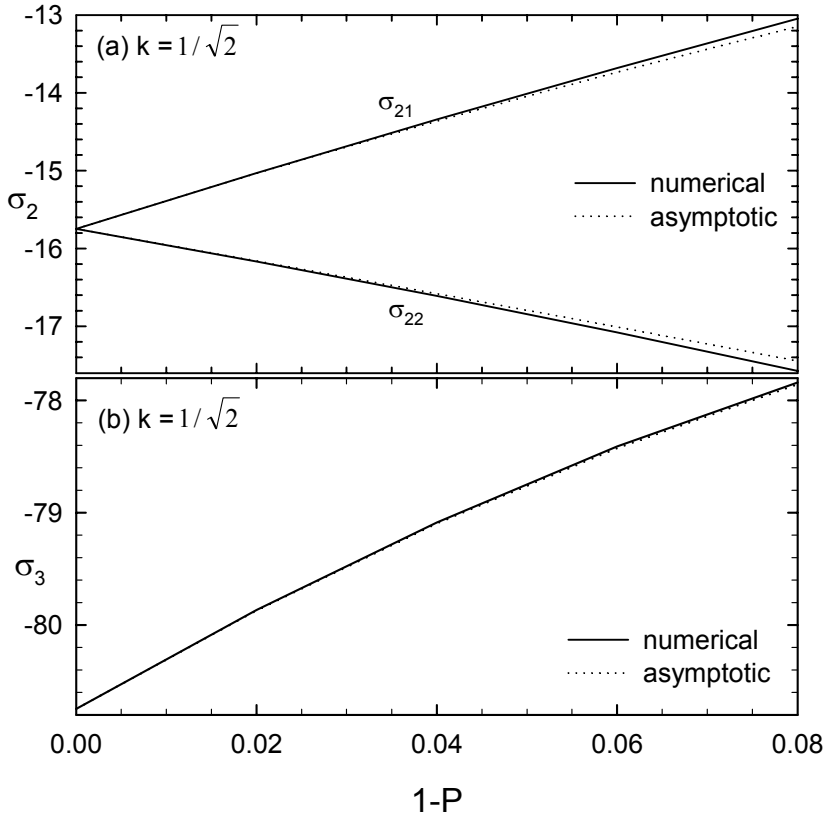

Fig. 4.17. The eigenvalues σ_2 (a) and σ_3 (b) versus (1-P) at k = $1/\sqrt{2}$ for the square wire. This value of k is k_m for P =1. The bifurcation of σ_2 as (1-P) increases is well captured by both solutions.

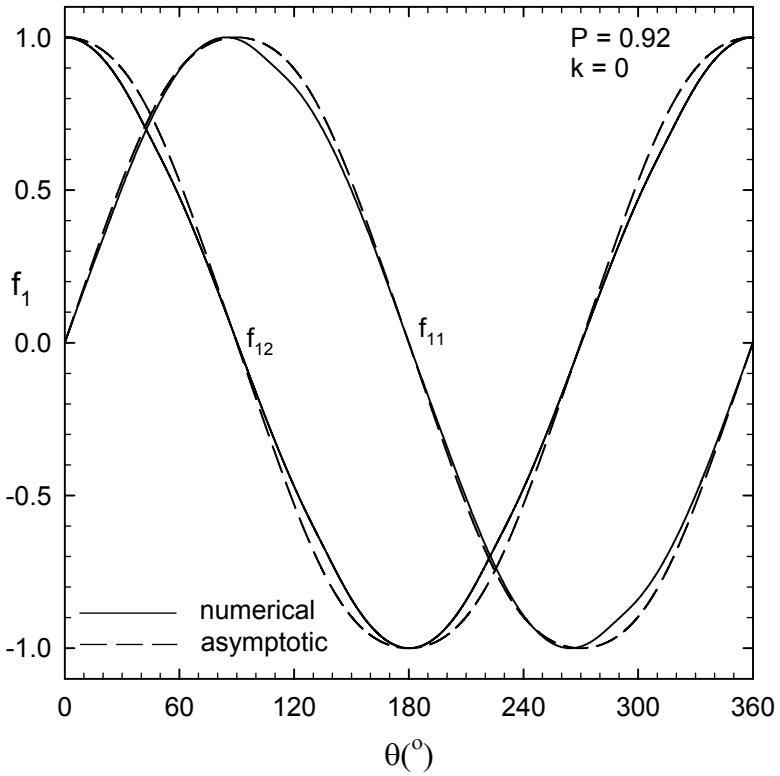

Fig. 4.18. Eigenfuntions f_{11} and f_{21} for P = 0.92 and k = 0. The value of P is the largest value of value of (1-P) in Fig. 4.16, and k = 0 is the wave number at which σ_1 is highest.

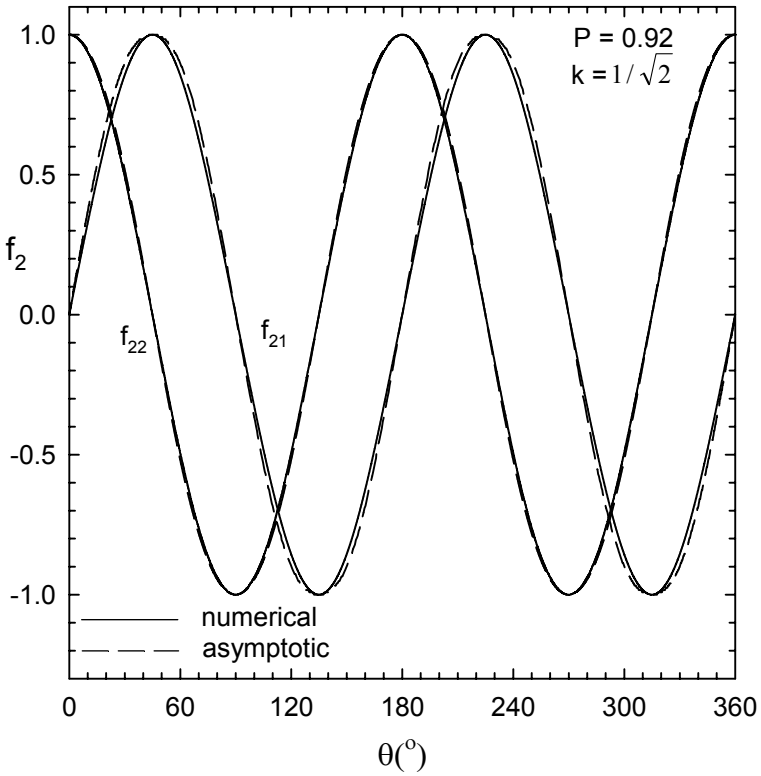

Fig. 4.19. Eigenfunctions f_{21} and f_{22} for P = 0.92 and k = $1/\sqrt{2}$. The value of P is the largest value of (1-P) in Fig. 4.17, and k = $1/\sqrt{2}$ = k_m for P = 1.

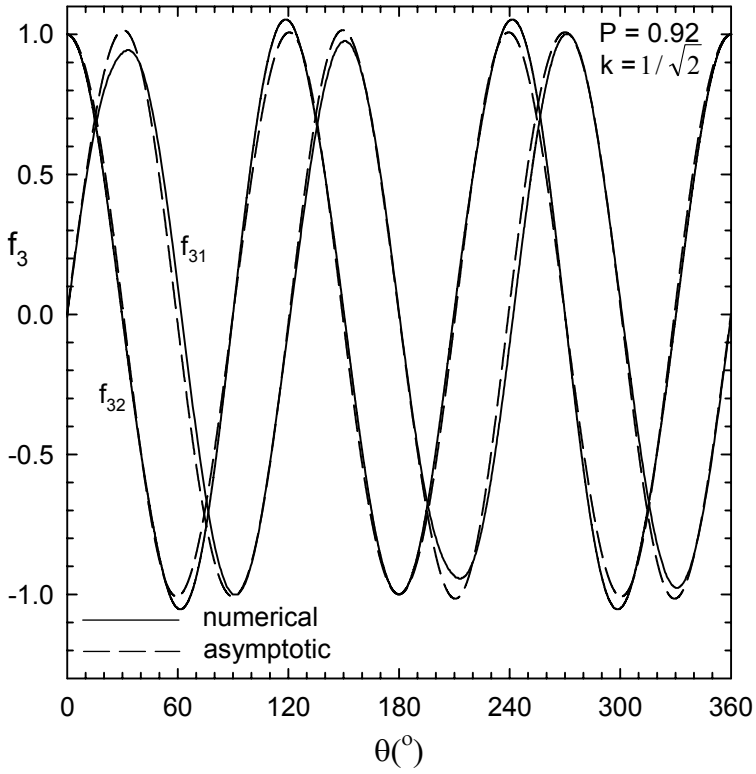

Fig. 4.20. Eigenfunctions f_{31} and f_{32} for P = 0.92 and k = $1/\sqrt{2}$. The value of P is the largest value of (1-P) in Fig. 4.17, and k = $1/\sqrt{2}$ = k_m for P = 1.

The eigenfunctions f_1, f_2 and f_3 are compared in Figs. 4.18-4.20 for P = 0.92. This value of P corresponds to the domain boundary of (1-P) shown in Figs. 4.15 and 4.17. Thus, the agreement between asymptotic and numerical results should improve as P increase. The zeroth asymptotic eigenfunction f_0 is simply a constant, and the comparison is not meaningful and therefore not shown.

4.8. Discussion

The surface energy is taken to be anisotropic in the circumferential direction only. Thus, the anisotropy is two dimensional. However, the stability results in this paper also hold for three-dimensional anisotropy, because the steady wire shape is two dimensional and a small perturbation in the surface position cannot see the variation in surface energy in the third dimension. Hence, the linear stability analysis is valid for anisotropy more general than the one used in this paper.

The degeneracy of eigenvalues provides an easy way to check the numerical accuracy. Two identical values are obtained for a set of eigenvalues, if the number N of Chebychev collocation points is large enough. The number of identical digits is an indication of the numerical accuracy. We increase N until at least four significant digits are the same. The square wire has a unit-cell of symmetry in the domain $0 \le \theta \le 90°$. However, when this domain is used in the computation, it determines σ_0, σ_4, σ_8, …. Other eigenvalues are missing, and can only be found using the full domain size. Thus, results of σ_1 are less accurate. When P << 1, σ_1 can not be calculated to the desirable accuracy, and therefore its values are not listed in Table 1 and 2.

In this work, length and time are made dimensionless by R_0 and $R_0^4/C\gamma_0$, where R_0 is half the crystal height along the symmetry plane shown in Fig. 4.1. It is also possible

Table 4.3 Numerical results for the square wire made dimensionless by A_c

P	k_m^*	σ_m^*	k_c^*	k_{1c}^*	σ_{1m}^*
1	1.253	2.467	1.772	0	0
0.5	1.305	2.944	1.847	0.768	1.757
0.35	1.332	3.202	1.880	1.011	2.645
0.05	1.475	4.096	2.084	-	-

Table 4.4 Numerical results for the triangular wire made dimensionless by A_c.

P	k_m^*	σ_m^*	k_c^*	k_{1c}^*	σ_{1m}^*
1	1.253	2.467	1.772	0	0
0.93	1.255	2.487	1.776	0.00893	0.0904
0.7	1.283	2.630	1.817	0.755	1.481
0.2	1.543	3.968	2.164	-	-
0.07	1.760	5.336	2.496	-	-

to use the cross-sectional area A_c to provide a length scale. If A_c is used, then all wires will have the same volume. We use R_0 because it is easily defined whereas A_c must be calculated numerically, and because the results can be easily converted to be volume measuring:

$$k^* = k\sqrt{A_c},$$

$$\sigma^* = \sigma A_c^2.$$

Table 3 and 4 list newly converted values of k_m^*, σ_m^*, k_c^*, k_{1c}^*, and σ_{1m}^*. It shows that both σ_m^* and k_c^* increase as P decrease. Thus, the non-monotonic behavior of σ_m and k_c is due to variation of in A_c.

One of the motivation for this work is to investigate the effect of non-circular equilibrium wire shape on the stability. By increasing the anisotropy while keeping thy same wire volume, we find that the anisotropy is destabilizing: Longer ranges of wavelength become unstable and the maximum growth rates increase. This is in contrast to the conclusions of Gurski and McFadden (2003), who found that the anisotropy can be stabilizing. Since they also compared wires with the same volume, the origin of this discrepancy is unknown.

The most unstable perturbation may breakup the wire in a time t given by $t\sigma_m \sim 1$. This estimate comes from the exponential growth of the perturbation. In dimensional terms, this breakup time is

$$\bar{t} = \frac{R_0^4}{C\gamma_0 \sigma_m}.$$

For a gold wire with radius 1 μm at 775°C , $D_s = 2.02 \times 10^{-6} \text{cm}^2/\text{s}$, $\gamma_0 = 1.78 \text{J/m}^2$, $\Omega = 1.78 \times 10^{-23} \text{cm}^3$ and we take $\upsilon \approx \Omega^{-2/3} = 1.5 \times 10^{15} \text{cm}^{-2}$. Thus $C\gamma_0 = 1.2 \times 10^{-4} \mu\text{m}^4/\text{s}$. The wire radius R_0 = 1 μm . From table 1, the maximum growth rate $\sigma_m = 0.25$ for a wire with circular cross-section. Thus $\bar{t} = 3.3 \times 10^4 \text{s}$.

4.9. Conclusions

The linear stability of a solid wire with square or triangular cross sections has been studied. The stability of the wire depends on the equilibrium wire shape and the wave number k of the perturbation in the axial direction. The equilibrium shape of the wire is prescribed by a newly developed delta-function model of facets, which allows strong anisotropy but at the same time avoids ill-postedness. The equilibrium shape is perturbed in both circumferential and axial directions. The perturbation is expanded in normal modes and the growth rate of a normal mode is found by solving an eigenvalue problem. The eigenvalue problem is solved numerically by a pseudospectral method, and analytically in the limit of zero anisotropy. The eigenvalue or the growth rate is found to be real. The fundamental eigenvalue is positive for long wavelengths. The maximum growth rate σ_m increases monotically with anisotropy. Thus, the surface energy anisotropy is destabilizing. The first eigenvalue is also positive for long wavelengths, bit the maximum magnitude is always less than σ_m for the range of parameter studied. The results obtained here for wires also hold for channels.

CHAPTER 5 RAYLEIGH'S INSTABILITY OF NANO-WIRES BY MOLECULAR DYNAMICS SIMULATIONS

5.1. Introduction

A thin liquid thread is unstable and will breakup into droplets to minimize the surface energy. The linear stability of a liquid jet was first studied by Lord Rayleigh [42]. Given a circular cylindrical liquid jet of radius R, its linear stability is revealed by imposing a small perturbation on the surface position in the form of a normal mode:

$$r = R + Ae^{\sigma t}\cos n\theta \cos kz, \tag{5.1}$$

where A is the amplitude of the perturbation, t is time, and (r , θ , z) are cylindrical coordinates defined at the center of the cylinder with z along the axis. By assuming inviscid flow and a capillarity-driven pressure gradient, Lord Rayleigh found the growth rate as

$$\sigma = \left(\frac{\gamma}{\rho R^3}\right)^{1/2}\left[\frac{kRI_1(kR)}{I_0(kR)}(1-k^2R^2-n^2)\right]^{1/2}, \tag{5.2}$$

where γ is surface tension, ρ is liquid density, and $I_0 = I_0(kR)$ and $I_1 = I_1(kR)$ are the modified Bessel function of the first kind of order 0 and 1, respectively. If the perturbation is axisymmetric (n = 0), then $\sigma > 0$ for $k < 1/R$. Thus, long wave axisymmeric perturbations will grow in time. Nonaxisymmetric perturbations ($n \geq 1$) do not grow since σ is imaginary.

A solid wire is also subject to Rayleigh's instability because it has surface energy and can change shape by surface diffusion [40]. Nichols and Mullins [43] analyzed the linear stability of a circular wire with isotropic surface energy. He

found that if a wire of radius R is perturbed by a disturbance of the form presented in (1.1), then the disturbance may grow with a growth rate

$$\sigma = \frac{B}{R^4}(n^2 + k^2R^2)(1 - k^2R^2 - n^2), \qquad (5.3)$$

where B is a material constant. Thus, axisymmetric disturbances with wavelengths greater than $2\pi R$ will also grow, and non-axisymmetric disturbances will decay. The evolution of a perturbed wire has been simulated numerically by Coleman. He followed the evolution of the wire to the point of pinch-off. Wong et al [40] derived a self-similar solution for the wire profile near the moment of pinch-off. They found that the self-similar profile contains a thin neck bridging two opposing cones with half-cone angle of $45.06°$. This cone angle is universal because it is independent of materials and initial condition. Their discovery is supported by the numerical simulations of Coleman .

The linear stability of a wire with surface energy anisotropy was first studied by Cohn. He assumed that the surface energy varies linearly in the axial direction but is isotropic in the circumferencial direction. As a result, the wire is still circular. He found that the anisotropy can be stabilizing or destabilizing. Gurski and McFadden investigated the linear stability of a wire with surface energy anisotropy in both axial and circumferencial directions. Their stability analysis is based on finding the sign of the second variation of the total surface energy. They found that the anisotropy can be stabilizing or destabilizing relative to the isotropic case. Their analysis, however, has a significant deficiency because it cannot yield the growth rates of the unstable perturbations.

In chapter 4, we analyzed the linear stability of thin wires with strong anisotropic surface energy. The wires are square or triangular in shape. The surface position is perturbed by an infinitesimal disturbance, which is expanded in normal modes. The growth rate of a normal mode is determined by solving an eigenvalue problem. They found that the anisotropy is strictly destabilizing. Their results are verified by an asymptotic solution in the limit of zero anisotropy.

Nanowires with size down to several nanometers and sufficient length have been fabricated in experiment [7]. Their mechanical, thermal, optical and electrical properties have been extensively investigated due to interests in low dimensional physics and applications in nano-technology.

Tantalum carbide nanorods and nanoparticles have been synthesized using a vapor-solid reaction path starting with CVD grown carbon nanotube precursors. The Rayleigh instability is postulated as ithe mechanism responsible for the transition from nanorod to nanoparticle morphologies.

This chapter will investigate the Rayleigh instability of nono-wires by molecular dynamic simulations. The purpose is to prove the applicability of continuum results to molecular scales. Particularly, we would like to verify the instability prediction of Kan and Wong, and the universal pinch-off angle derived in chapter 4. This paper is organized as follows. The simulation method is outlined in Section 5.2, and the results are presented in Section 5.3. We discuss the implications in Section 5.4 and conclude in Section 5.5.

5.2. Simulation Method

5.2.1 Intermolecular Potential and Force

We will use the Lennard-Jones potential to describe the interaction between atoms. The Lennard-Jones potential between two atoms separated by a distance r^* is

$$\varphi^* = 4\varepsilon\left[\left(\frac{\sigma}{r^*}\right)^{12} - \left(\frac{\sigma}{r^*}\right)^{6}\right] \quad , \tag{5.4}$$

where ε stands for the well depth of the potential curve, and σ is a characteristic distance at which the potential equals zero.

The attracting force between two atoms is the first derivative of the potential:

$$F^* = -\frac{24\varepsilon}{r^*}\left[2\left(\frac{\sigma}{r^*}\right)^{12} - \left(\frac{\sigma}{r^*}\right)^{6}\right]. \tag{5.5}$$

This equation can be made dimensionless as follows:

$$F = \frac{F^*}{\varepsilon/\sigma} \ , \tag{5.6a}$$

$$r = \frac{r^*}{\sigma}, \tag{5.6b}$$

$$F = -\frac{24}{r}\left(\frac{2}{r^{12}} - \frac{1}{r^{6}}\right). \tag{5.6c}$$

Two atoms experience zero force at a distance $r = S = 2^{1/6}$. For the rest of the paper, time and velocity are made dimensionless by $\sigma\sqrt{m/\varepsilon}$ and $\sqrt{\varepsilon/m}$, respectively, where m is the mass of the atom.

5.2.2 Integration of Newton's Equation of Motion

This work will apply the velocity-verlet algorithm to integrate Newton's equation of motion. Given the position $\mathbf{r}(i)$ and velocity $\mathbf{V}(i)$ of an atom at the ith time step, the velocity-verlet algorithm calculates the position and velocity at the next time step as

$$\mathbf{r}(i+1) = \mathbf{r}(i) + \mathbf{V}(i)\Delta t + \frac{1}{2}(\Delta t)^2 \mathbf{F}(i), \tag{5.7a}$$

$$\mathbf{V}(i+1) = \mathbf{V}(i) + \frac{1}{2}\Delta t[\mathbf{F}(i) + \mathbf{F}(i+1)], \tag{5.7b}$$

where $\mathbf{F}$ is the force exerted on the atom by other atoms, and Δt is the time interval. At time step i, $\mathbf{r}(i)$ and $\mathbf{V}(i)$ are known. The force $\mathbf{F}(i)$ can be calculated since the positon $\mathbf{r}(i)$ of all atoms are known. Then $\mathbf{r}(i+1)$ at time step i+1 can be calculated from (7a). From $\mathbf{r}(i+1)$, $\mathbf{F}(i+1)$ can be calculated and $\mathbf{V}(i+1)$ at time step (i+1) can be derived from (7b).

The Velocity-verlet algorithm has a discretization error of order $(\Delta t)^2$. In this study, we take $\Delta t = 0.01$. We have tried smaller Δt, and it does not change the conclusions of the simulations.

5.2.3 Initial Positions and Velocities

The initial positions of atoms are shown in Fig. 5.1. The axis of the nano-wire is in the z direction. A layer of atoms in a cross-section plane (x, y) is arranged into a hexagon. Two closest neighbor atoms in the same layer are separated by distance S, at which the force between two atoms calculated by (6c) is zero. The next layer of atoms is shifted as shown in Fig. 5.1. The distance between two neighbor layers is $\sqrt{2/3}S$, so that two closest atoms between tow layer are

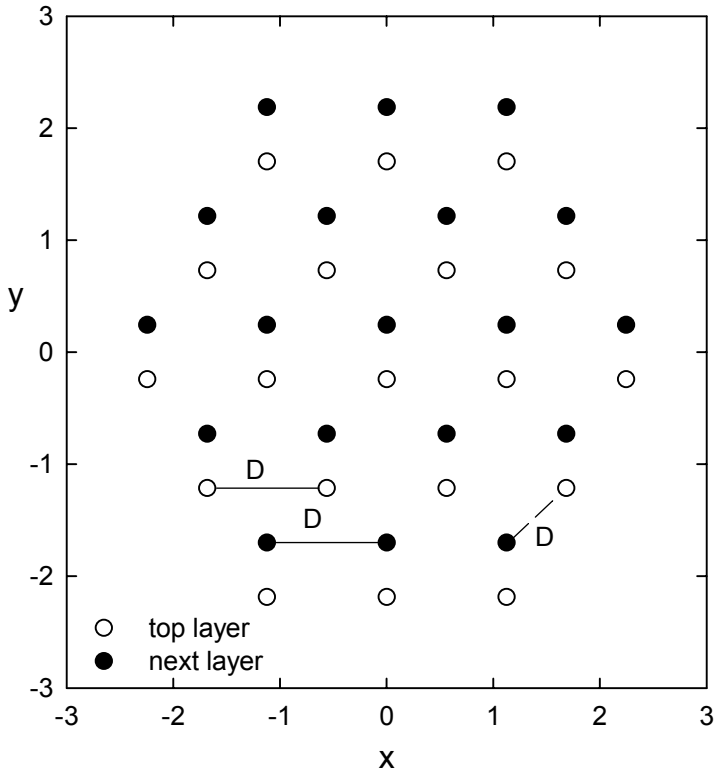

Fig. 5.1. Initial positions of atoms in two neighbor layers. The distance between any two closest neighbor atoms is S.

always a distance S apart. This arrangement of atoms is repeated along the axis, so that the atoms are arranged in hcp. The initial velocity of an atom is created by a random number generator with the number n^* ranging from 0 to 1. This number is then multiplied by a mean velocity corresponding to a specified temperature.

5.2.4 Boundary Conditions

Periodic boundary conditions are imposed at the two ends of the wire at z = 0 and z = L. At time t, the initial positions and velocities of atoms are assumed specified in the main section. These are copied to two neighbor periodic sections with L added to or subtracted from the z coordinates of atoms. At the next time step, the positions and velocities of atoms in the main section will be calculated by the velocity verlet algorithm. Each atom in the main periodic section experiences forces by all other atoms in three periodic sections with a cutoff distance of r = 5. When an atom diffuses out of one end of the main section, another atom will diffuse into the main section from the opposite end to the corresponding position. There are reflective walls at $x = \pm 6R$ and $y = \pm 6R$, but they are seldom used because the atoms do not fly away from the wire at the temperatures studied. After the positions and velocities of atoms in the main section are updated. we will repeat the copying process. In this way, the nano-wire evolves.

5.2.5 Thermostat

The temperature of the nano-wire is maintained constant by a velocity rescaling method. Let the instantaneous temperature of the wire be T, which is calculated by the following expression:

$$T = \frac{1}{2N}\sum_{1}^{N} \mathbf{V}_i \cdot \mathbf{V}_i , \tag{5.8}$$

where $\mathbf{V}_i$ is the velocity of the ith atom, and N is the number of atoms in one periodic section. The temperature has been made dimensionless by ε/k_B, where k_B is the Boltzmann constant.Assume the desired temperature is T_o. In our study, at every ten time steps velocities are scaled by a factor P:

$$P = \sqrt{\frac{T_0}{T}} . \tag{5.9}$$

This way of maintaining the temperature is commonly use in the literature and does not affect the mechanism of this work

5.3. Simulation Results

We simulate with different length L and with radius R = S, 2S, and 3S. The case of R = 2S is shown in Fig. 5.1. The melting temperature depends on the wire size and is determined by two method: the mean-square displacement δ and the internal energy per atom E. The mean-square displacement is defined as

$$\delta = \frac{1}{N}\sum_{j=1}^{N} (\mathbf{r}_j(t_0 + 100) - \mathbf{r}_j(t_0))^2 , \tag{5.10}$$

where $t_0 = 50$.

Fig. 5.2 presents the average mean-square displacement δ as a function of temperature T for different size R of nanowires. The plot is used to find the

melting point of the nanowires. The diffusion of atoms becomes much faster when the temperature reaches T=0.14, 0.34, and 0.40 for nanowire radius R = S, 2S and 3S, respectively, indicating the melting points of the nanowires.

The internal energy E per atom is defined as

$$E = \frac{1}{N}\left(\frac{1}{2}\sum_{i-1}^{N} V_i \cdot V_i + \frac{1}{2}\sum_{i=1}^{N}\sum_{j=1}^{N}\varphi_{ij}\right), \tag{5.11}$$

where φ_{ij} is the Lennard-Jones potential between atom i and j. Fig. 5.3 shows the internal energy per atom E(T) as a function of temperature T for different size R of nanowires. When a three dimensional system melts, a jump in the caloric curve can be observed, which can be used to find the melting point of the nanowires. As the sizes of nanowire increase, the jumps in E(T) become more obvious, which occurs at T = 0.34 and 0.40 for R = 2S and 3S, respectively. The jump in E(T) for R = S is indistinguishable because the nanowire at that size is very close to be a one-dimensional system and there is no strict phase transition existing for one dimensional systems.

Figs. 5.4-5.6 show snapshots at different times of nanowires with different radius R, length L, and temperature T. The length L is expressed in terms of $dz = \sqrt{2/3}S$, which is the initial separation between two layers. The nanowires are soilid at the temperature studied.

Fig. 5.7 depicts the total energy as a function of time t for the nanowire with R = 2S, L = 30dz, and T = 0.32. When the nanowire breaks, there is an obvious drop of total energy in the curve and the total energy tends to a constant value as time t increases after breakup.

Figs. 5.8-5.10 show snapshots at different times of the nanowire with different radus R, length L, and temperatue T. At the studied temperatures, the nanowires are solid. The nanowires will not break and evolve into stable shapes after long times.

Fig. 5.11 shows a summary of behavior of nanowires with different radius R, length of periodic section L, and temperature T. At these temperatures, all the nanowires are liquid. The plot shows that all wires break when the ratio $L/R > 2\pi$, which agrees with Rayleigh's instability prediction of liquid jet at continuum level.

Fig. 5.12 shows a summary behavior of nanowires with different radius R, lenth of periodic section L, and temperature T. At these temperatures, all the nanowires are solid. The plot shows that the critical ratio of L/R deviates from 2π, which disagrees with the Rayleigh's instability of solid wires derived at the continuum level. But our result showed that the solid nanowires can be unstable.

5.4. Discussion

To study the effect of strain and compression to the instability of the nanowires. One case of r = d, L = 18 dz, and T = 0.14 is picked. In this case, the nanowire is solid and L is slightly below the critical periodic section length. The initial distance between two adjacent atoms is varied from 1.0 to 1.3 whereas the equilibrium distance between two adjacent atoms in R = 1.12. Our result shows that strain and compression will change the shape of the nanowires, but will not vary the instability behavior of the nanowires.

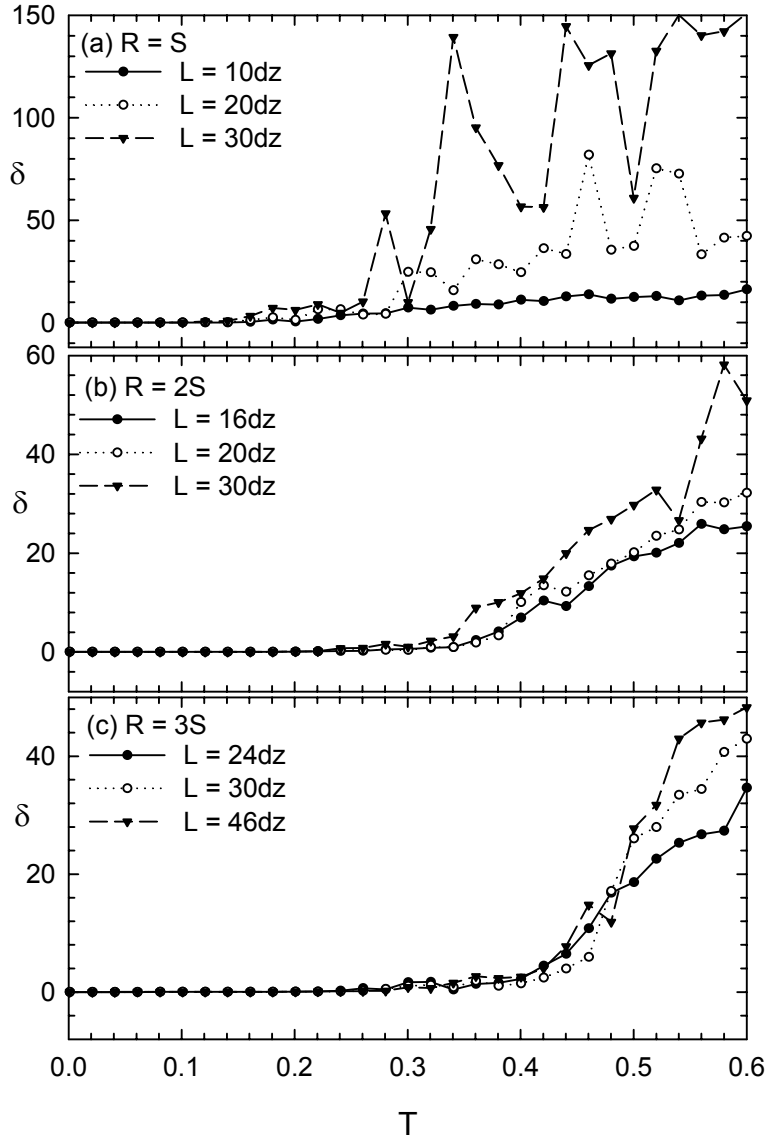

Fig. 5.2. Average mean-square displacement versus temperature for different radus R and length L of nanowires.

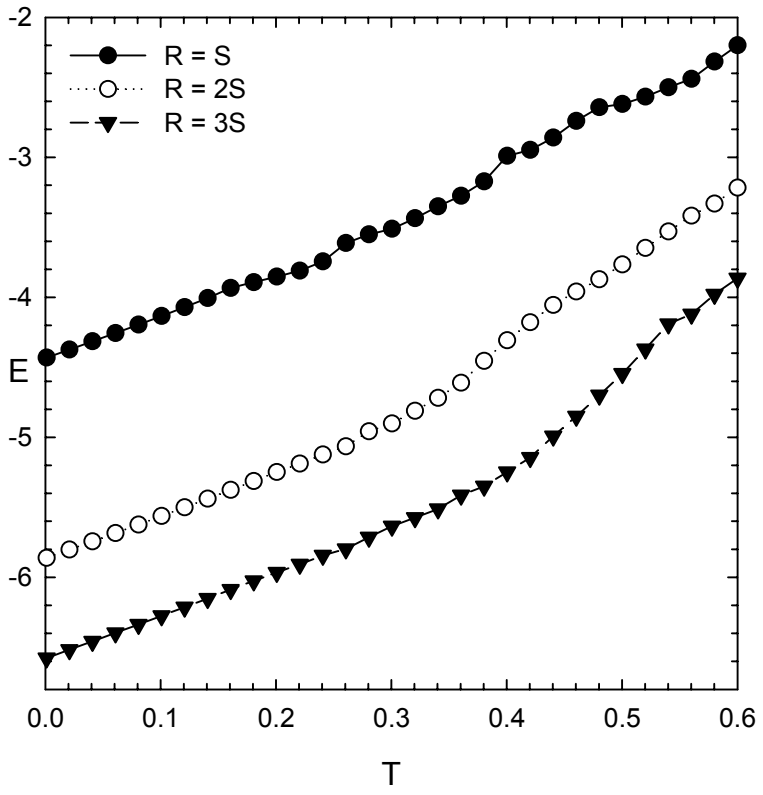

Fig. 5.3. Average internal energy per atom versus temperature for different radial size of nanowires.

R = D, L = 20dz, T = 0.14

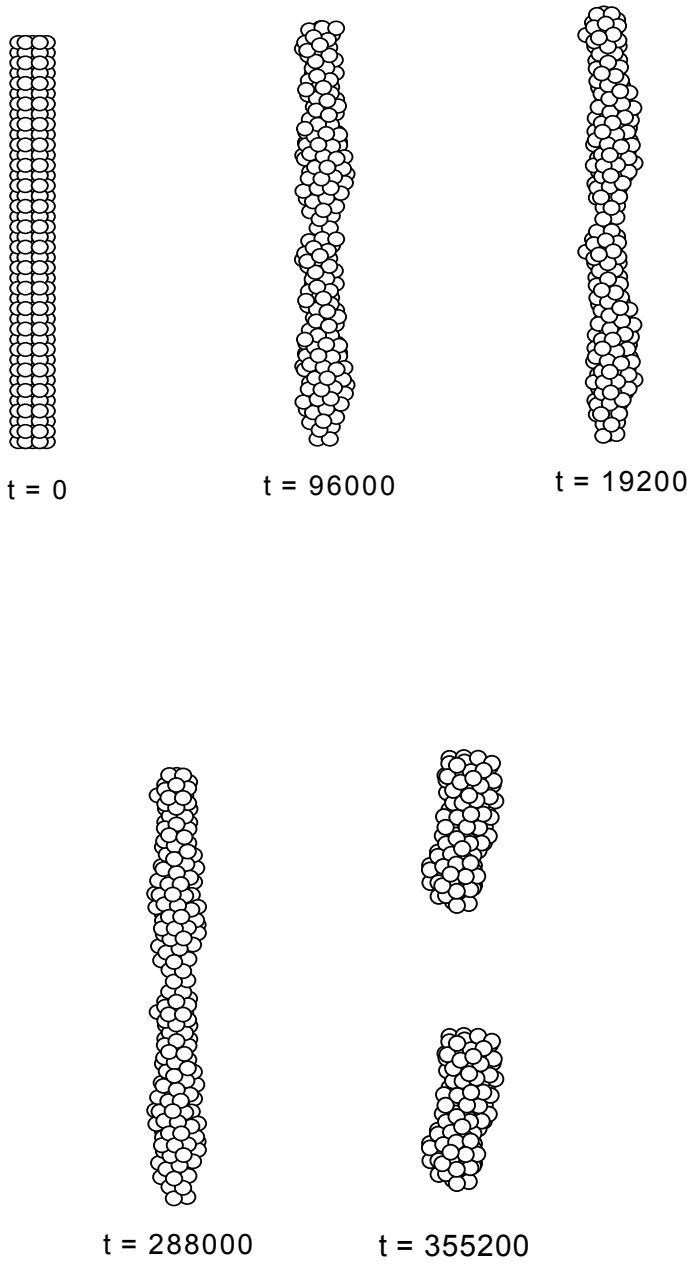

Fig. 5.4 Snapshots at different times of the nanowire with radius R = S, periodic section length L = 20dz and temperature T = 0.14. The distance $dz = \sqrt{2/3}S$ is the initial separation between two adjacent layers.

R = 2D, L = 16dz, T = 0.32

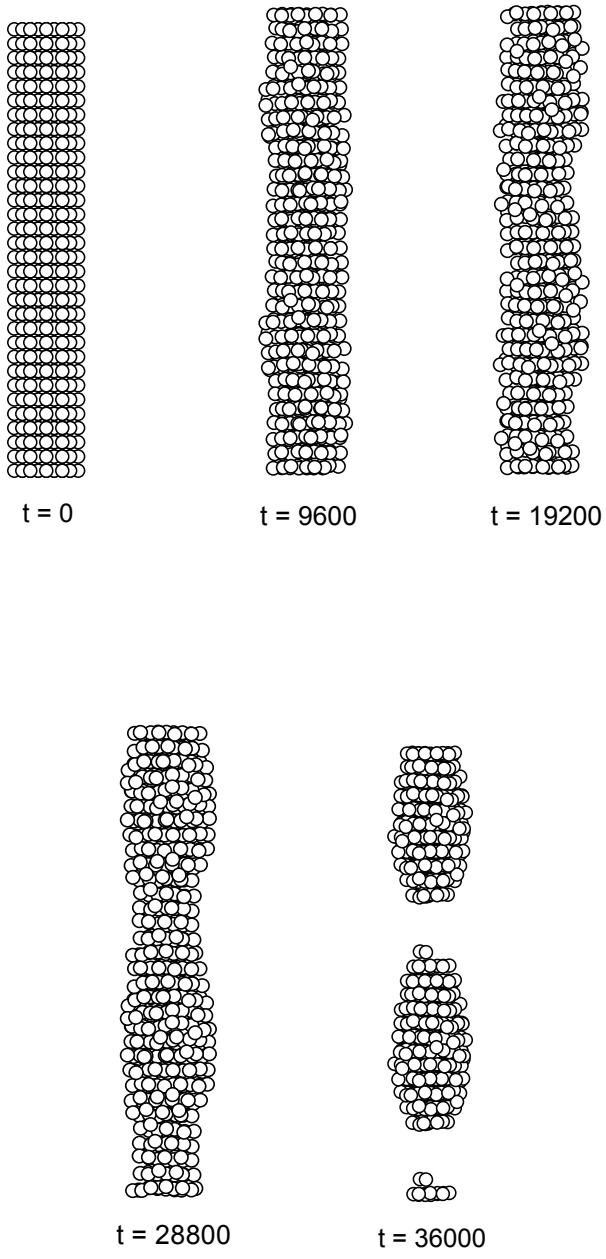

Fig. 5.5. Snapshots at different times of the nanowire with radius R = 2S, periodic section length L = 16dz and temperature T = 0.32. The distance $dz = \sqrt{2/3}S$ is the initial separation between two adjacent layers.

R = 3D, L =30dz, T = 0.38

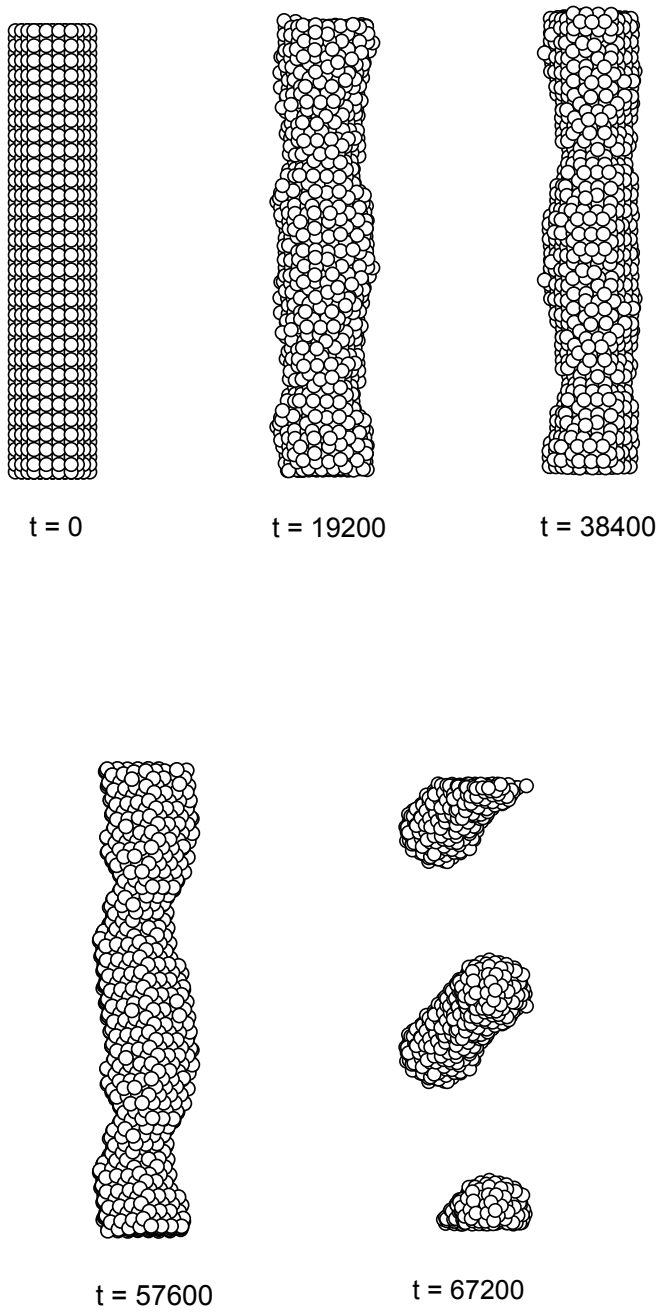

Fig. 5.6. Snapshots at different times of the nanowire with radius R = 3S, periodic section length L = 30dz and temperature T = 0.38. The distance $dz = \sqrt{2/3}S$ is the initial separation between two adjacent layers.

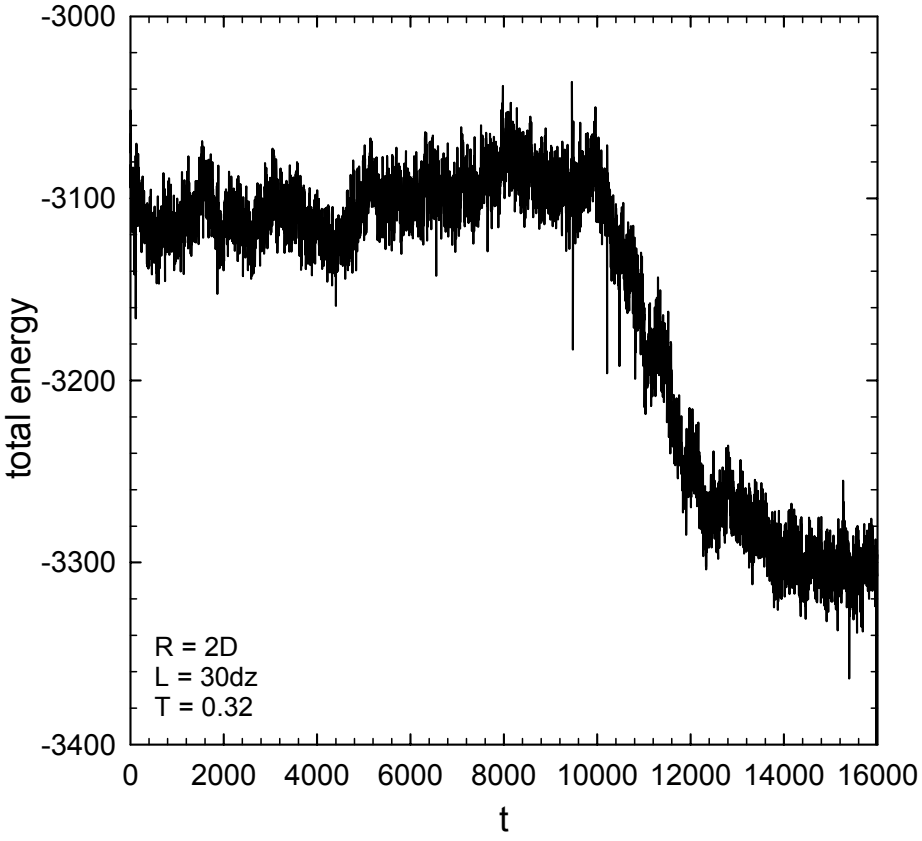

Fig. 5.7. Total energy versus time t for the nanowire with R = 2S, L = 30dz and T = 0.32.

R = 2D, L = 16dz, T = 0.14

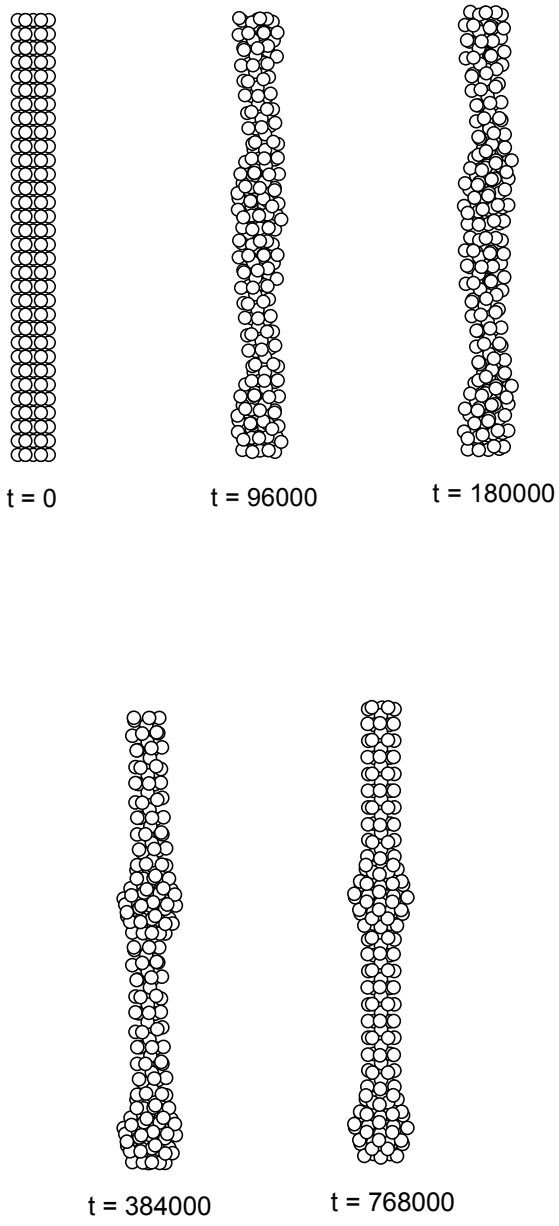

Fig. 5.8 Snapshots at different times of the nanowire with radius R = S, periodic section length L = 16dz and temperature T = 0.14. The distance $dz = \sqrt{2/3}S$ is the initial separation between two adjacent layers.

R = D, L = 12dz, T = 0.32

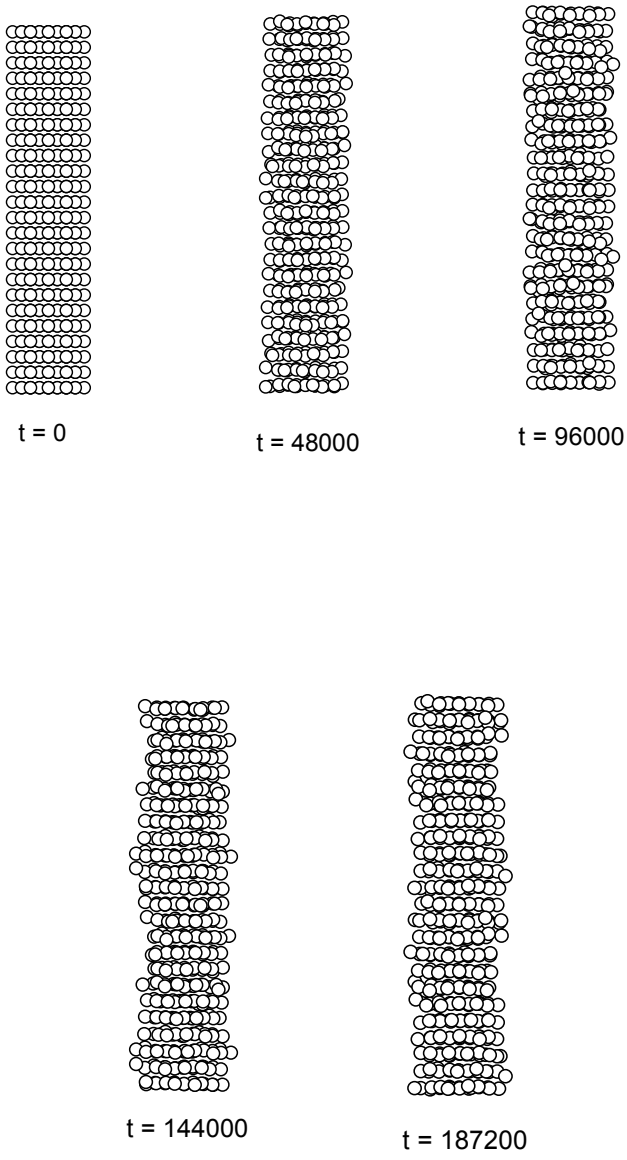

Fig. 5.9. Snapshots at different times of the nanowire with radius R = 2S, periodic section length L = 12dz and temperature T = 0.32. The distance $dz = \sqrt{2/3}S$ is the initial separation between two adjacent layers.

R = 3D, L =27dz, T = 0.38

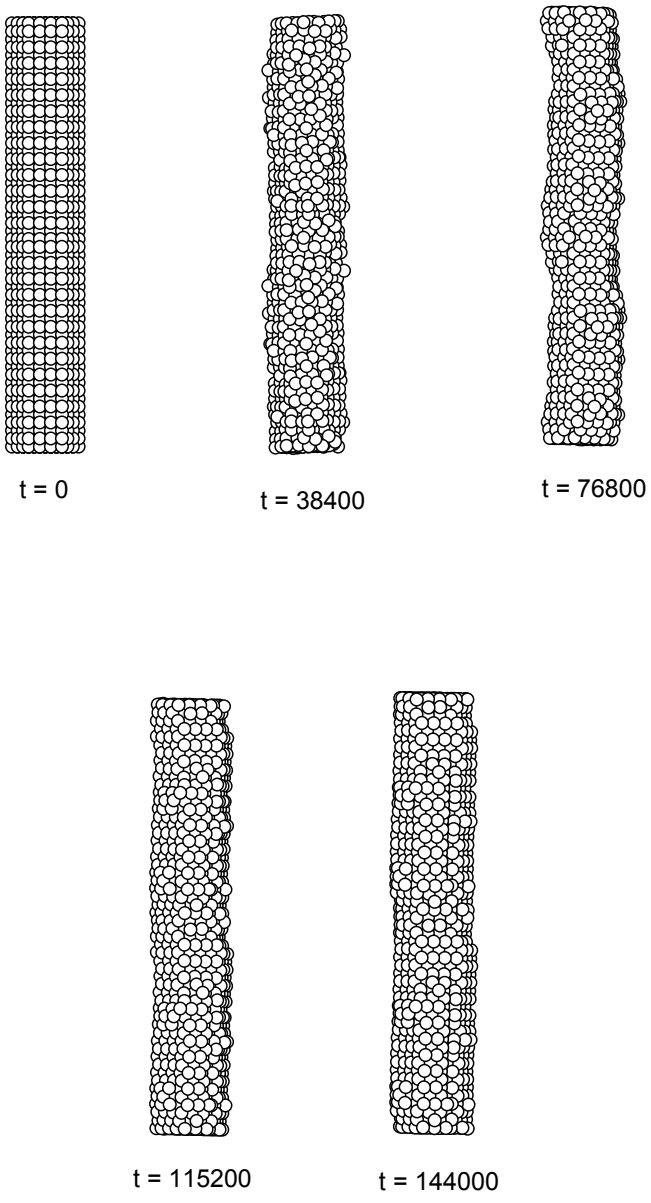

Fig. 5.10. Snapshots at different times of the nanowire with radius R = 3S, periodic section length L = 27dz and temperature T = 0.38. The distance $dz = \sqrt{2/3}S$ is the initial separation between two adjacent layers.

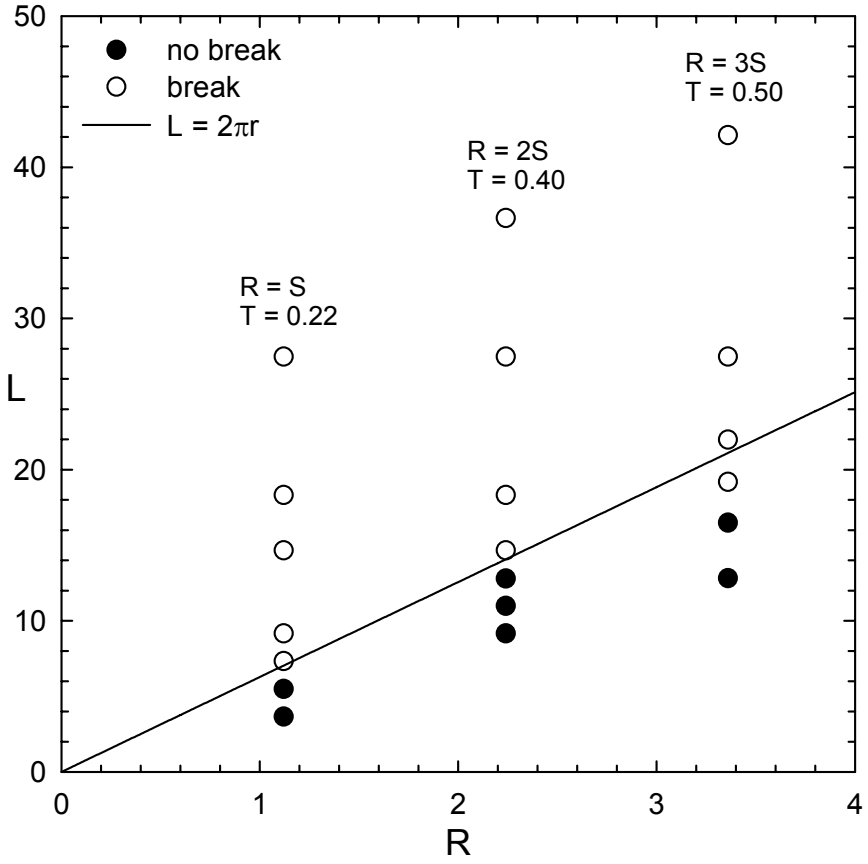

Fig. 5.11. Behavior of nanowires at different radius R, length of periodic section L and temperature T. At these temperatures, all the nanowires are liquid.

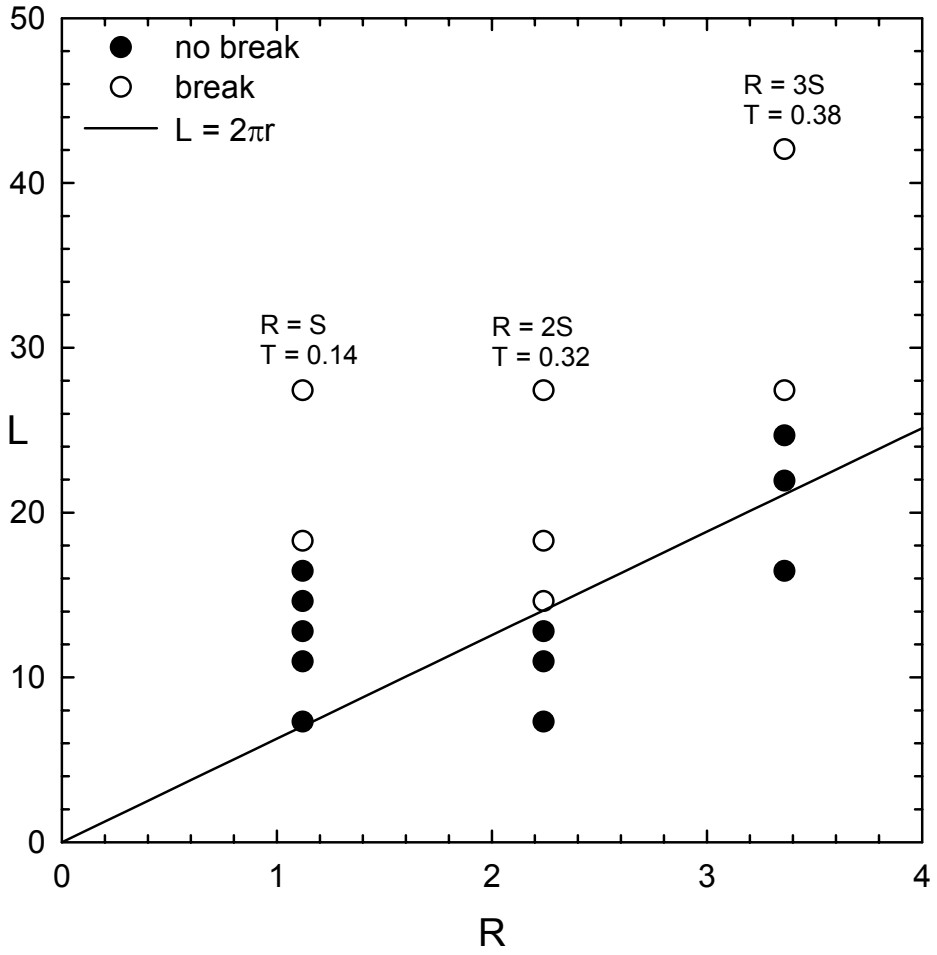

Fig. 5.12. Behavior of nanowires at different radius R, length of periodic section L and temperature T. At these temperatures, all the nanowires are solid.

5.5. Conclusion

This chapter investigates the Rayleigh's instability of nanometer scale wires by classic molecular dynamic simulations. The melting points of nanowires with different radius are found by computing the caloric curve and mean square displacement curve. Our results show that as the radius of the nanowires increases, the corresponding melting point will increase. For liquid nanowires, the ratios of wavelength of perturbation to radius of nanowire are very close to 2π. For solid nanowires, the ratios of wavelength of perturbation to radius of nanowire are higher than 2π, which shows that the instability behavior of nanowires at the atomic level is different from that of solid wires in continuum level.

CHAPTER 6 CONCLUSIONS

We study the diffusion-controlled growth of N compound layers in binary diffusion couples with the nonlinear Kirkendall effect included. The partial differential equations are nonlinear and are reduced to nonlinear ordinary differential equations by a self-similar transformation. The nonlinear ordinary differential equations are solved numerically by a fourth-order Runge-Kutta method. These nonlinear equations are coupled at the interfaces, the locations of which are unknown and are determined iteratively. We analyze a particular diffusion couple with two product layers in detail and find that when the diffusivity ratio is large the growth of one layer can suppress that of the other. The method of finding intrinsic diffusion coefficients from only the locations of interfaces for one layer in previous work has been extended to two layers in present work. The asymptotic analysis valid for small concentration gradients is applied to the "multi-foil" method, and yields an analytic solution for the displacement curve. We find that the intrinsic diffusion coefficients can be calculated from only two vertice positions of the displacement curve.

The three-dimensional instability of a retracting film edge on a substrate is studied. The retracting film profile is two dimensional with a straight contact line and a thickened edge followed by a valley. The two dimensional film is perturbed in three dimensions and the film evolves by capillarity-driven surface diffusion. One unstable mode of perturbation is found and the growth rate of the unstable mode depends on the velocity of the retracting edge and the wavenumber k of

the sinusoidal perturbation along the film edge. Our results show that the faster the film boundary moves, the more unstable the film is. When the wave number of the perturbation is less than a critical wavenumber k_c, the film is always unstable. While the film is always stable when the wave number of the perturbation is greater than k_c. We also derive an analytic expression for the growth rate σ and the critical wavenumber k_c as a function of k and b, respectively. Comparison between analytic expressions of σ and k_c and the numerical solutions show good agreement for small k and b, respectively.

The linear stability of solid wire or cavity with square and triangular cross sections has been studied. The stability of the wire or cavity depends on the equilibrium shape of the cross section, the radius of curvature of the corner and the wave number of the perturbation. When the radius of the curvature P = 1, the wire or cavity becomes a cylinder and is susceptible to Rayleigh's capillary instability. For the zeroth eigenmode, for both square and triangular cross sections, sharpening the corner between two adjacent facets will destabilize the wire or cavity. With a fixed radius of curvature, the growth rate σ = 0 when the wave number k = 0 (i.e. the wavelength is infinity). Increasing the wave number will distabilize the wire or until k reaches a critical wave number $k_{c,}$ after which the wire or cavity will be stabilized as wave number k increases. For the first eigenmode, for both square and triangular cross sections, sharpening the corner of the cross section will distabilize the wire or cavity. With fixed radius of curvature of P, increasing wave number k beyond a critical wavenumber k_{1c} will stabilize the wire or cavity. The second and higher eigenmodes are always

stable. For the triangular shape, with fixed radius curvature, increasing the wave number will stabilize the wire or cavity. Sharpening the corner of the cross section will distabilize the wire or cavity. Thus, the surface energy anisotropy is destabilizing.

We investigate Rayleigh's instability of nanometer scale wires by molecular dynamic simulations. The melting points of nanowires with different radius are found by computing the caloric curve and mean square displacement curve. Our results show that as the radii of the nanowires increases, the corresponding melting point will increase. When the nanowires are in liquid state, the ratios of wavelength of perturbation to radius of nanowires are very close to 2π. For liquid nanowires, the ratios of wavelength of perturbation to radius of nanowires are higher than 2π, in agreement with Rayleigh's prediction, which shows that the instability behavior of nanowires at atomic level is different from that of solid wires at continuum level.

REFERENCES

[1] Tu, K. N., Mayer, J. W. and Feldman, L. C., Electroic Thin Film Science, 1992 Macmillan, New York.

[2] Mayer JW, Lau SS. Electronic materials science: for intergrated circuits in Si and GaAs. New York: Macmillan, 1990.

[3] Munir, Z. A., High Temperature Science, 1990, 27, 279.

[4] Munir ZA. Metal. Trans. A 1992, 23A, 7.

[5] Srolovitz, D. J. and Safran, S. A., J. Appl. Phys., 1986, 60, 247.

[6] Blakely, J. M., Introduction to the Properties of Crystal Surfaces, Pergamon Press, New York, 1973.

[7] Ohnishi, H., Kondo, Y. and Takayanagi, K., Nature, 1998, 395, 780.

[8] Agrait, N., Rubio, G. and Vieira, S., Phys. Rev. Lett., 1995, 74, 3995.

[9] Krans, J. M., van Ruitenbeck, J., M., Fisun, V. V., Yanson, I. K. and de Jongh, L. J., Nature, 1995, 357, 767.

[10] Pascual, J. I., Mendex, J., Gomez-Herrero, J., Baro, A. M., Garcia, N., Landman, U., Luedtke, W. D. Bogachek, E. N. and Cheng, H. P., Science, 1995, 267, 1793.

[11] Diaz, M., Costa-Kramer, J. L., Escobar, A. L., Leon, N. and Coreria, A., Nanotechnology, 2002, 13, 43.

[12] Rubio, G, Agrait, N., Vieira, S., Phys. Rev. Lett., 1996, 76, 2302.

[13] Gulseren, O., Ercolessi, F. and Tosatti, E., Physical Review B, 1995, 51, 11, 7377.

[14] Bilalbegovic, G., Solid State Communications, 2000, 115, 73.

[15] Hwang, H. J. and Kang, J. W., Surface Science, 2003, 532, 536.

[16] Wang, B., Wang, G., Chen, X. and Zhao, Ji., Physical Review B 2003, 67, 193403.

[17] Zhang H, Wong H. Acta mater 2000, 48, 1371.

[18] Cheng JY, Chen LJ. J Appl Phys 1991, 69, 2161.

[19] Michaelsen C, Yan ZH. , Bormann R. J. Appl. Phys. 1993, 73, 2249.

[20] Lin JH, Chen LJ. J. Appl. Phys. 1995, 77, 4425.

[21] Shim JY, Kwak JS, Baik HK. Thin Solid Films 1996, 288, 309.

[22] Tu KN, Mayer JW, Feldman LC. Electronic thin film science. New York: Macmillan, 1992.

[23] Kidson GV. J. Nucl. Mater. 1961, 3, 21.

[24] Wagner C. Acta metall. 1969, 17, 99.

[25] Hickl AJ, Heckel RW. Metallurgical Trans. A 1975, 6A, 431.

[26] Sarkhel AK, Seigle LL. Metallurgical Trans. A 1976, 7A, 899.

[27] Shatynski SR, Hirth JP, Rapp RA. Acta metall. 1976, 24, 1071.

[28] Williams DS, Rappp RA, Hirth JP. Metallurgical Trans. A 1981, 12A, 639.

[29] Cornet JF, Calais D. J. Phys. Chem. Solids 1972, 33, 1675.

[30] Cornet JF. J Phys Chem Solids 1974, 5, 1247.

[31] Philibert J. Atom movements: diffusion and mass transport in solids. Les Ulis, France: Les Editions de Physique, 1991.

[32] van Dal MJH, Pleumeekers MCLP, Kodentsov AA, van Loo FJJ. Acta mater 2000, 48, 385.

[33] Shewmon PG. Diffusion in solids. New York: McGrawhill, 1963.

[34] Wohlert S, Bormann R. J Appl Phys 1999, 85, 825.

[35] Heumann T, Lohmann P. Z Elektrochem 1955, 59, 849.

[36] Ince EL. Ordinary differential equations. New York: Dover, 1956.

[37] Kennefick, C. M. and Raj, R., Acta metal., 1989, 37, 2947.

[38] Jiran, E. and Thompson, C. V., J. Electron. Mater., 1990, 19, 1153.

[39] Wong, H., Voorhees, P. W., Miksis, M. J. and Davis, S. H., Acta mater, 2000, 48, 1719.

[40] Wong, H., Miksis, M. J., Voorhees, P. W. and Davis, S. H., Acta mater., 1997, 46, 2477.

[41] Mullins WW. Solid surface morphologies governed by capillarity. In: Metal Surfaces. Metals Park, Ohio: Am Soc Metals, 1963. 17.

[42] Rayleigh, L., London Math. Soc., 1879, 10, 4.

[43] Nichols, F. A. and Mullins, W. W., Trans. Metall. Soc., AIME, 1965, 233, 1840.

[44] Rayleigh, L., London Math. Soc., 1879, 10, 4.

[45] Marr-Lyon, M. J., Thiessen, D. B. and Marston, P. L., Phys. Rev. Lett., 2001, 86, 2293, 209901.

[46] McCallum, M. S., Voorhees, P. W., Miksis, M. J., Davis, S. H. and Wong, H., J. Appl. Phys. 1996, 79, 7604.

[47] Gurski, K. F. and McFadden, G. B., Proceedings of the Royal Society (London), 2003, A 459, 2575.

[48] Evans, A. G. and Charles, E. A., Acta metall., 1977, 25, 919.

[49] Golovin A. A., Davis S. H., Nepomnyashchy A. A., Physica D, 1998, 122, 202.

[50] Xin T., Wong, H., Surface Science, 2001, 487, L529.

[51] Xin T., Wong H., 2003, submitted.

[52] Conrad, E. H., Engel, T., Surface Science, 1997, 299/300, 391.

[53] Nolden, I. M., van Beijeren, H., Physical Review, B, 1994, 49, 17224.

[54] Heyraud, J. C., Metois, J. J., Bermond, J. M., Surface Science, 1999, 425, 48.

APPENDIX A. SECOND-ORDER ASYMPTOTIC SOLUTION

The asymptotic expansion for the one-layer case starts by introducing a small parameter $\varepsilon = C_{10} - C_{12} << 1$ into the governing equation and boundary conditions [17]. In the limit $\varepsilon \to 0$, the concentration can be expanded in series of ε:

$$c(y) = f_0(y) + f_1(y)\varepsilon + f_2(y)\varepsilon^2 + \ldots \quad , \tag{A1}$$

$$f_0(y) = C_{10}$$

$$f_1(y) = S(y+1)$$

$$f_2(y) = E_3 y^3 + E_2 y^2 + E_1 y + E_0$$

$$S = -\frac{C_{10} - C_{21}}{C_{01} - C_{21}}$$

$$E_3 = \frac{(C_{10} - C_{21})^2}{6(C_{01} - C_{10})(C_{01} - C_{21})^2}$$

$$E_2 = \frac{-(C_{10} - C_{21})^2 (1 - R_{A1})}{2(C_{01} - C_{21})^2 [C_{10}(1 - R_{A1}) + R_{A1}]}$$

$$E_1 = \frac{(Q_1 R_{A1} + Q_0)}{6(C_{01} - C_{10})(C_{01} - C_{21})^2 [C_{10}(1 - R_{A1}) + R_{A1}]}$$

$$E_0 = \frac{(U_1 R_{A1} + U_0)}{6(C_{01} - C_{21})^2 [C_{10}(1 - R_{A1}) + R_{A1}]}$$

$$Q_1 = -3C_{10}^3 + 3(3C_{01} + C_{21} - 1)C_{10}^2 - [2(4C_{01} + C_{21} - 3)C_{21} + 5C_{01}^2]C_{10}$$
$$+ C_{01}^2(3C_{21} + 2) + C_{01}C_{21}(3C_{21} - 4) - C_{21}^2$$

$$Q_0 = 3C_{10}^3 - 3(3C_{01} + C_{21})C_{10}^2 + [5C_{01}^2 + 8C_{01}C_{21} + 2C_{21}^2]C_{10} - 3C_{01}C_{21}(C_{01} + C_{21})$$

$$U_1 = C_{10}^2 + (C_{21} - 5C_{01} + 2)C_{10} + 3C_{01}C_{21} - 4C_{21} + 2C_{01})$$

$$U_0 = -C_{10}^2 - C_{01}C_{21} + 5C_{01}C_{10} - 3C_{01}C_{21} \ .$$

Substitution of (A1) into (2.34) and (2.35) gives

$$\frac{dx}{dt} = \varepsilon^2 F_3 t^{-3/2} x^2 + \varepsilon^2 F_2 t^{-1} x + \varepsilon(F_1 + \varepsilon F_0) t^{-1/2} \qquad \text{(A2)}$$

$$F_3 = 3(D_{A1} - D_{B1}) E_3 (2D_1 D_{B1})^{-3/2}$$

$$F_2 = 2(D_{A1} - D_{B1}) E_2 (2D_1 D_{B1})^{-1}$$

$$F_1 = (D_{A1} - D_{B1}) S (2D_1 D_{B1})^{-1/2}$$

$$F_0 = (D_{A1} - D_{B1}) E_1 (2D_1 D_{B1})^{-1/2} \ .$$

Equation (A2) is a generalized Riccati equation [36]. A particular solution is found as

$$x = x_p = 2\varepsilon F_1 t^{1/2} + O(\varepsilon^3) \ .$$

To find the general solution, let

$$x = x_p + 1/u \ , \qquad \text{(A3)}$$

and u obeys

$$\frac{du}{dt} + \varepsilon^2 F_2 t^{-1} u + \varepsilon^2 F_3 t^{-3/2} = 0 \ . \qquad \text{(A4)}$$

Since $\varepsilon << 0$, u can be solved by successive substitution. When $\varepsilon = 0$, u = a_0, a constant. When this solution is substituted into the second term in (A4), we get

$$u = a_0 (1 - \varepsilon^2 F_2 \ln t) + 2\varepsilon^2 F_3 t^{-1/2} \ .$$

Transformation of u back to x and imposing the initial condition that $x = x_0$ at $t = t_0$ gives

$$a_0 = \frac{1}{x_0 - 2\varepsilon(F_1 + \varepsilon F_0) t_0^{1/2}} (1 + \varepsilon^2 F_2 \ln t_0) - 2\varepsilon^2 F_3 t_0^{-1/2} \ .$$

Substitution of u into (A3) followed by expansion in ε yields the displacement as

$$z = x - x_0 = 2\varepsilon(F_1 + \varepsilon F_0)t^{1/2}[1-(\frac{t_0}{t})^{1/2}] - \varepsilon^2 F_2 x_0 \ln(\frac{t_0}{t}) + 2\varepsilon^2 F_3 x_0^2 t^{-1/2}[(\frac{t}{t_0})^{1/2} - 1].$$

As explained in section 2.7, t_0 and x_0 are related by the interfacial positions. If $x_0 > 0$, then $x_0 = (2D_2 D_{B1} t_0)^{1/2}$ and $x_2 = (2D_2 D_{B1} t)^{1/2}$. Thus, $(t_0/t)^{1/2} = x_0/x_2$. If $x_0 < 0$, then $x_0 = -(2D_1 D_{B1} t_0)^{1/2}$ and $x_1 = (2D_1 D_{B1} t)^{1/2}$. This leads to $(t_0/t)^{1/2} = -x_0/x_1$. Thus, if $x_0 > 0$,

$$z = z_m[(1-\frac{x_0}{x_2}) - \varepsilon\frac{2E_2}{S}\frac{x_0}{x_1}\ln\frac{x_0}{x_2} + \varepsilon\frac{3E_3}{S}\frac{x_0}{x_1}(\frac{x_2}{x_1} - \frac{x_0}{x_1})], \qquad \text{(A5a)}$$

and if $x_0 < 0$

$$z = z_m[(1+\frac{x_0}{x_1}) - \varepsilon\frac{2E_2}{S}\frac{x_0}{x_1}x_0\ln(\frac{-x_0}{x_1}) + \varepsilon\frac{3E_3}{S}(-\frac{x_0}{x_1})(1+\frac{x_0}{x_1})], \qquad \text{(A5b)}$$

where

$$z_m = \frac{2\varepsilon(C_{10}-C_{21})(D_{B1}-D_{A1})}{(C_0-C_{21})}\frac{t}{x_1} - \frac{\varepsilon^2(D_{B1}-D_{A1})(D_{A1}Q_1 + D_{B1}Q_0)}{3(C_0-C_{21})^2(C_0-C_{10})[C_{10}(D_{B1}-D_{A1})+D_{A1}]}\frac{t}{x_1}$$

Figure 2.9 shows z/z_m versus x_0/x_1. In general, the displacement curve is not symmetric about $x_0 = 0$ for two reasons. First, $x_1 \neq x_2$ unless $D_{A1} = D_{B1}$, in which case $z_m = 0$ and the Kirkendall effect vanishes. Second, the second term on the right side of (A4a) is positive, whereas that of (A4b) is negative. The third term is negative for both equations. Thus, the displacement curve is always straighter on the right side ($x_0 > 0$) than on the left side($x_0 < 0$).

APPENDIX B. DERIVATION OF THE BOUNDARY CONDITIONS

The boundary conditions in (3.12) are imposed at the unknown contact line position $X = X_p$. Since the perturbation $\delta << 1$, the boundary conditions can be Taylor expanded about the position of the static contact line at X = 0. The first two-term expansion of (3.12a) is

$$Y_s + \delta + (Y_{sX} + \delta_X)X_p = 0, \tag{B1}$$

where X in the subscript denotes differentiation, and the functions in (B1) are evaluated at $X = 0$. At the static contact line $X = 0$,

$$Y_s = 0. \tag{B2}$$

Substitution of (B2) into (B1) gives

$$X_p = -\frac{\delta}{Y_{sX}}. \tag{B3}$$

Expansion of (3.12b) around $X = 0$ gets the following equation:

$$\frac{1}{[1+(Y_{sX}+\delta_X)^2+\delta_z^2]^{1/2}} - \frac{(Y_{sX}+\delta_X)(Y_{sXX}+\delta_{XX})+\delta_Z\delta_{ZX}}{[1+(Y_{sX}+\delta_X)^2+\delta_z^2]^{3/2}} X_p = \cos\alpha, \tag{B4}$$

where Z in the subscript denotes differentiation. Since (3.12b) holds at the static contact line $X = 0$,

$$\frac{1}{(1+Y_{sX}^2)^{1/2}} = \cos\alpha. \tag{B5}$$

Thus, to leading order in δ, (B4) becomes

$$Y_{sXX}\delta - Y_{sX}\delta_X = 0. \tag{B6}$$

Expansion of (3.12c) around $X = 0$ gives

$$[\mathbf{m} \cdot \nabla_s \kappa]_{X=0} + [\frac{\partial}{\partial X}(\mathbf{m} \cdot \nabla_s \kappa)]_{X=0} X_p = 0. \quad \text{(B7)}$$

Since $Y_X << 1$ and $Y_Z << 1$, the tangent unit vector **m**, the surface gradient ∇_s, and the curvature κ can be simplified from (3.12) as

$$\mathbf{m} = Y_X \mathbf{e}_X + Y_Z \mathbf{e}_Z \quad \text{(B8a)}$$

$$\nabla_s = \mathbf{e}_X \frac{\partial}{\partial X} + \mathbf{e}_Y (Y_X \frac{\partial}{\partial X} + Y_Z \frac{\partial}{\partial Z}) + \mathbf{e}_Z \frac{\partial}{\partial Z} \quad \text{(B8b)}$$

$$\kappa = -(Y_{XX} + Y_{ZZ}), \quad \text{(B8c)}$$

At the static contact line $X = 0$, (3.12c) holds:

$$Y_{sXXX} = 0. \quad \text{(B9)}$$

Thus, (B7) becomes

$$Y_{sX} \delta_{XXX} + Y_{sX} \delta_{ZZX} - Y_{sXXXX} \delta = 0. \quad \text{(B10)}$$

Substitution of the steady film profile in (3.6a) and the normal-mode expansion of δ in (3.10) into (B6) and (B10) gives the two boundary conditions in (3.13) at $X = 0$.

APPENDIX C. THE COEFFICIENTS c_i OF THE DIFFERENTTIAL EQUATIONS

The coefficients c_i in (4.19) are found by Maple V® as

$$c_4 = (R^2 + R_\theta^2)^{-1/2}(R^2 + 2R_\theta^2 - RR_{\theta\theta})^{-1}$$

$$c_3 = 2R^{-1}(R^2 + R_\theta^2)^{-3/2}(R^2 + 2R_\theta^2 - RR_{\theta\theta})^{-2}[(R_\theta^2 + R^2)R^2R_{\theta\theta\theta} + 2R^2R_\theta R_{\theta\theta}^2$$
$$-(9R_\theta^2 + 5R^2)RR_\theta R_{\theta\theta} + 2R_\theta(2R_\theta^4 - R^4)]$$

$$c_2 = -c(R^2 + R_\theta^2)^{-1}[c_{20}R_{\theta\theta\theta\theta} - c_{21}R_{\theta\theta\theta}^2 + c_{22}R_{\theta\theta\theta} + c_{23}R_{\theta\theta}^4 +$$
$$c_{24}R_{\theta\theta}^3 + c_{25}R_{\theta\theta}^2 - c_{26}R_{\theta\theta} + 8k^2RR_\theta^{10} + 8(4k^2R^2 + 9)RR_\theta^8$$
$$+ 2(25k^2R^2 + 29)R^3R_\theta^6 + (38k^2R^2 - 15)R^5R_\theta^4 + (14k^2R^2 - 17)R^7R_\theta^2$$
$$+ (2k^2R^2 - 1)R^9]$$

$$c_1 = -c[c_{10}R_{\theta\theta\theta\theta} + c_{11}R_{\theta\theta\theta}^2 + c_{12}R_{\theta\theta\theta} + c_{13}R_{\theta\theta}^5 +$$
$$c_{14}R_{\theta\theta}^4 + c_{15}R_{\theta\theta}^3 + c_{16}R_{\theta\theta}^2 + c_{17}R_{\theta\theta} + 16k^2R_\theta^{13}$$
$$+ 72k^2R^2R_\theta^{11} + 8(16k^2R^2 - 17)R^2R_\theta^9 + 16(7k^2R^2 - 6)R^4R_\theta^7 + 48(k^2R^2$$
$$+ 1)R^6R_\theta^5 + (k^2R^2 + 41)R^8R_\theta^3 + 3R^{10}R_\theta]$$

$$c_0 = c[c_{00}R_{\theta\theta\theta\theta} - c_{01}R_{\theta\theta\theta}^2 + c_{02}R_{\theta\theta\theta} - c_{03}R_{\theta\theta}^5 - c_{04}R_{\theta\theta}^4 - c_{05}R_{\theta\theta}^3$$
$$+ c_{06}R_{\theta\theta}^2 - c_{07}R_{\theta\theta} + 4k^4RR_\theta^{14} + 24k^2R(k^2R^2 - 1)R_\theta^{12} + (61k^4R^4 - 82k^2R^2$$
$$- 136)RR_\theta^{10} + (85k^4R^4 - 111k^2R^2 - 96)R^3R_\theta^8 + 2(35k^4R^4 - 40k^2R^2 + 24)R^5R_\theta^6$$
$$+ (34k^4R^4 - 36k^2R^2 + 41)R^7R_\theta^4 + (9k^4R^4 - 10k^2R^2 + 3)R^9R_\theta^2 + R^{13}k^2(k^2R^2 - 1)]$$

$$c = R^{-1}(R^2 + R_\theta^2)^{-7/2}(R^2 + 2R_\theta^2 - RR_{\theta\theta})^{-3}$$

$$c_{20} = R^2[RR_{\theta\theta}(R^2 + R_\theta^2)^2 - R_\theta^2(2R_\theta^4 + 5R^2R_\theta^2 + 4R^4) - R^6]$$

$$c_{21} = 2R^3(R^2 + R_\theta^2)^2$$

$$c_{22} = -RR_\theta[R^2R_{\theta\theta}^2(R^2 + R_\theta^2) - 2RR_{\theta\theta}(3R_\theta^2 + 2R^2)(R_\theta^2 + R^2) - (16R_\theta^6 + 50R^2R_\theta^4 + 51R^4R_\theta^2 + 17R^6)]$$

$$c_{23} = 3R^3(2R^2 - 3R_\theta^2)$$

$$c_{24} = 3R^2(19R_\theta^4 - 5R^2R_\theta^2 - 4R^4)$$

$$c_{25} = 2R[R_\theta^6(k^2R^2 - 60) + R^2R_\theta^4(3k^2R^2 + 1) + R^4R_\theta^2(3k^2R^2 + 16) + k^2R^8]$$

$$c_{26} = 8R_\theta^8(k^2R^2 - 6) + 2R^2R_\theta^6(14k^2R^2 + 71) + 12R^4R_\theta^4(3k^2R^2 + 14) + R^6R_\theta^2(20k^2R^2 + 31) + R^8(4k^2R^2 - 7)$$

$$c_{10} = -4RR_\theta[RR_{\theta\theta}(R_\theta^2 + R^2)^3 - (2R_\theta^8 + 7R^2R_\theta^6 + 9R^4R_\theta^4 + 5R^6R_\theta^2 + R^8)]$$

$$c_{11} = 8R^2R_\theta(R_\theta^2 + R^2)^3$$

$$c_{12} = 3R^3R_{\theta\theta}^3(R^4 - R_\theta^4) + R^2R_{\theta\theta}^2(18R_\theta^6 + 5R^2R_\theta^4 - 26R^4R_\theta^2 - 13R^6) + RR_{\theta\theta}[-2R_\theta^8(k^2R^2 + 40) - 2R^2R_\theta^6(4k^2R^2 + 81) - R^4R_\theta^4(12k^2R^2 + 95) - 2R^6R_\theta^2(4k^2R^2 + 3) - R^8(2k^2R^2 - 7)] + R_\theta^2[4R_\theta^8(k^2R^2 + 4) + 2R^2R_\theta^6(9k^2R^2 - 10) + 4R^4R_\theta^4(8k^2R^2 - 29) + R^6R_\theta^2(28k^2R^2 - 111) + 4R^8(3k^2R^2 - 7)] + R^{10}(2k^2R^2 + 3)$$

$$c_{13} = 3R^3R_\theta(R_\theta^2 - 7R^2)$$

$$c_{14} = -3R^2R_\theta(19R_\theta^4 - 39R^2R_\theta^2 - 8R^4)$$

$$c_{15} = RR_\theta(138R_\theta^6 - 197R^2R_\theta^4 + 32R^4R_\theta^2 + 67R^6)$$

$$c_{16} = R_\theta[2R_\theta^8(5k^2R^2 - 24) + 2R^2R_\theta^6(20k^2R^2 + 207) + R^4R_\theta^4(60k^2R^2 - 1) +$$

$$4R^6R_\theta^2(10k^2R^2 - 53) + R^8(10k^2R^2 - 49)]$$

$$c_{17} = -RR_\theta[28k^2R_\theta^{10} + 2R_\theta^8(61k^2R^2 + 74) + 4R^2R_\theta^6(52k^2R^2 - 83) + R^4R_\theta^4(172k^2R^2 - 427) + R^6R_\theta^2(68k^2R^2 - 73) + 2R^8(5k^2R^2 + 12)]$$

$$c_{00} = RR_{\theta\theta}[R_\theta^8(k^2R^2 - 2) + R^2R_\theta^6(4k^2R^2 - 5) + 3R^4R_\theta^4(2k^2R^2 - 1) + R^6R_\theta^2(4k^2R^2 + 1) + R^8(k^2R^2 + 1)] - 2R_\theta^{10}(k^2R^2 - 2) - 3R^2R_\theta^8(3k^2R^2 - 4) - R^4R_\theta^4(16k^2R^2 - 11) - R^6R_\theta^4(14k^2R^2 - 1) - 3R^8R_\theta^2(2k^2R^2 + 1) - R^{10}(k^2R^2 + 1)$$

$$c_{01} = 2R[R_\theta^8(k^2R^2 - 2) + R^2R_\theta^6(4k^2R^2 - 5) + 3R^4R_\theta^4(2k^2R^2 - 1) + R^6R_\theta^2(4k^2R^2 + 1) + R^8(R^2k^2 + 1)]$$

$$c_{02} = 6R^4R_\theta R_{\theta\theta}^3(R^2 + R_\theta^2) + RR_\theta R_{\theta\theta}^2[R_\theta^6(k^2R^2 - 2) + 3R^2R_\theta^4(k^2R^2 - 15) + 3R^4R_\theta^2(k^2R^2 - 22) + R^6(k^2R^2 - 23)] + 2R_\theta R_{\theta\theta}[R_\theta^8(7k^2R^2 - 10) + R^2R_\theta^6(29k^2R^2 + 15) + 3R^4R_\theta^4(15k^2R^2 + 22) + R^6R_\theta^2(31k^2R^2 + 56) + R^8(8k^2R^2 + 15)] - RR_\theta[8k^2R_\theta^{10} + 30R_\theta^8(k^2R^2 + 2) + R^2R_\theta^6(39k^2R^2 + 140) + R^4R_\theta^4(17k^2R^2 + 99) - 3R^6R_\theta^2(k^2R^2 - 4) - R^8(3k^2R^2 + 7)]$$

$$c_{03} = 6R^4(4R_\theta^2 + R^2)$$

$$c_{04} = R^3[R_\theta^4(2k^2R^2 - 159) + R^2R_\theta^2(4k^2R^2 + 3) + 2R^4(k^2R^2 + 6)]$$

$$c_{05} = R_\theta^2[R_\theta^6(17k^2R^2 - 18) + R^2R_\theta^4(43k^2R^2 + 315) + R^4R_\theta^2(35k^2R^2 - 66) + 9R^6(k^2R^2 - 11)]$$

$$c_{06} = R[k^2R_\theta^{10}(k^2R^2 + 20) + R_\theta^8(5k^4R^4 + 18k^2R^2 + 320) + R^2R_\theta^6(10k^4R^4 - 54k^2R^2 - 311) + R^4R_\theta^4(10k^4R^4 - 82k^2R^2 - 411) + R^6R_\theta^2(5k^4R^4 -$$

$$30k^2R^2 - 73) + R^8(k^4R^4 + 7)]$$

$$c_{07} = 4k^2R_\theta^{12}(2 + k^2R^2) + 2R_\theta^{10}(11k^4R^4 - 13k^2R^2 + 38) + 2R^2R_\theta^8(25k^4R^4 -$$

$$61k^2R^2 - 231) + R^4R_\theta^6(60k^4R^4 - 141k^2R^2 - 470) + R^6R_\theta^4(40k^4R^4 -$$

$$63k^2R^2 - 41) + R^8R_\theta^2(14k^4R^4 - 13k^2R^2 + 42) + R^{10}(2k^2R^2 - 1)(k^2R^2 - 1)$$

APPENDIX D. EXPRESSION FOR $R_{\theta\theta}$, $R_{\theta\theta\theta}$, AND $R_{\theta\theta\theta\theta}$

The derivatives $R_{\theta\theta}$, $R_{\theta\theta\theta}$, and $R_{\theta\theta\theta\theta}$ can be determined following the procedure for R_θ as

$$R_{\theta\theta} = -S^2R^3/HU^3 - R^3/HU + R(R^2+S^2)/U^2 \ , \tag{D1}$$

$$R_{\theta\theta\theta} = -3R^5S^3/H^2U^5 - H_\varphi R^5S^2/H^3U^4 - R^3S(4R^2+5S^2)/HU^4 + 3R^5S/H^2U^3$$

$$+ H_\varphi R^5/H^3U^2 + RS(5R^2+S^2)/U^3 - 5R^3S/HU^2 , \tag{D2}$$

$$R_{\theta\theta\theta\theta} = 15R^7S^4/H^3U^7 + 10H_\varphi R^7S^3/H^4U^6 + 3(H_\varphi)^2R^7S^2/H^5U^5 + R^7S^2(2H_\varphi - H_{\varphi\varphi})/H^4U^5$$

$$+ R^5S^2(7R^2+5S^2)/H^2U^6 + R^7S(6H_\varphi + 12S)/H^3U^5 - 3R^7(H_\varphi)^2/H^5U^3 + R^7H_{\varphi\varphi}/H^4U^3$$

$$- R^3(18S^4 + 50R^2S^2 + 4R^4)/HU^5 + R^5(7R^2+37S^2)/H^2U^4 + R^5(10SH_\varphi - 3R^2)/H^3U^3$$

$$+ R(S^4 + 18R^2S^2 + 5R^4)/U^4 - R^3(10R^2+18S^2)/HU^3 + 5R^5/H^2U^2 \ , \tag{D3}$$

where

$$S = y\cos\varphi - x\sin\varphi ,$$

$$U = x\cos\varphi + y\sin\varphi ,$$

and $H = ds/d\varphi$ is the radius of curvature given in (4.6). The above expressions are obtained by using Maple V®.

APPENDIX E. DETAILS OF THE ASYMPTOTIC SOLUTION

The coefficients b_{ij} in (4.31) are found by Maple V® as

$$b_4 = \varepsilon^2 b_{42} + \varepsilon b_{41} + b_{40}$$

$$= \varepsilon^2[A_1 + A_2\cos(4\theta) + A_3\cos^2(4\theta)] + \varepsilon[A_4 + A_5\cos(4\theta)] + A_6, \qquad \text{(E1)}$$

$$b_3 = \varepsilon^2 b_{32} + \varepsilon b_{31} + b_{30}$$

$$= \varepsilon^2[D_1\sin(4\theta) + D_2\sin(4\theta)\cos(4\theta)] + \varepsilon D_3\sin(4\theta), \qquad \text{(E2)}$$

$$b_2 = \varepsilon^2 b_{22} + \varepsilon b_{21} + b_{20}$$

$$= \varepsilon^2[E_1 + E_2\cos(4\theta) + E_3\cos^2(4\theta)] + \varepsilon[E_4 + E_5\cos(4\theta)] + E_6, \qquad \text{(E3)}$$

$$b_1 = \varepsilon^2 b_{12} + \varepsilon b_{11} + b_{10}$$

$$= \varepsilon^2[G_1\sin(4\theta) + G_2\sin(4\theta)\cos(4\theta)] + \varepsilon G_3\sin(4\theta), \qquad \text{(E4)}$$

$$b_0 = \varepsilon^2 b_{02} + \varepsilon b_{01} + b_{00}$$

$$= \varepsilon^2[K_1 + K_2\cos(4\theta) + K_3\cos^2(4\theta)] + \varepsilon[K_4 + K_5\cos(4\theta)] + K_6, \qquad \text{(E5)}$$

in which $b_{30} = b_{10} = 0$ and

$$A_1 = 40\alpha^2 - 6,\ A_2 = 76\alpha,\ A_3 = -366\alpha^2,\ A_4 = 3,\ A_5 = -19\alpha,\ A_6 = -1, \qquad \text{(E6a-f)}$$

$$D_1 = -576\alpha, D_2 = 5824\alpha^2,\ D_3 = 144\alpha, \qquad \text{(E7a-c)}$$

$$E_1 = -8\alpha^2(1585 + 6k^2) + 2(k^2 - 3),\ E_2 = -4\alpha(17k^2 + 317),$$

$$E_3 = 2\alpha^2(313k^2 + 12993), \quad E_4 = 3 - 2k^2,$$

$$E_5 = \alpha(34k^2 + 317),\ E_6 = 2k^2 - 1, \qquad \text{(E8a-f)}$$

$$G_1 = 16\alpha(6k^2 + 45),\ G_2 = -16\alpha^2(312k^2 + 1385),\ G_3 = -4(45\alpha + 35k^2), \qquad \text{(E9a-c)}$$

$$K_1 = k^2(1+8968\alpha^2+8\alpha^2k^2)+9936\alpha^2, K_2 = 30\alpha(32+17k^2),$$

$$K_3 = -20112\alpha^2 - \alpha^2k^2(18439+264\alpha k^2),\ K_4 = -k^2(1+k^2),$$

$$K_5 = -15\alpha(k^4+17k^2+16),\ K_6 = k^2(1-k^2). \qquad \text{(E10a-f)}$$

The second-order eigenvalue Σ_2 is found following the same procedure as that for Σ_1. Multiplying both side of (4.34c) by $d^2F_0/d\theta^2$, and integrating from 0 to 2π leads to

$$\Sigma_2 = -\int_0^{2\pi} T_2 \frac{d^2F_0}{d\theta^2}d\theta \Big/ \int_0^{2\pi} F_0 \frac{d^2F_0}{d\theta^2}d\theta\ . \qquad \text{(E11)}$$

Similar to F_0, Σ_1, and F_1, Σ_2 also has two branches. Substitution of $F_0 = F_0^1 = \sin n\theta$, $\Sigma_1 = \Sigma_1^1$, and $F_1 = F_1^1$ into (E11) yields two cases. If $n \neq 0$ or 2, then

$$\Sigma_2^1 = L_6 + (L_7\int_0^{2\pi}\sin^2 n\theta\cos 4\theta\, d\theta + L_8\int_0^{2\pi}\sin^2 n\theta\cos^2 4\theta\, d\theta - L_9\int_0^{2\pi}\sin n\theta\cos n\theta\sin 4\theta\, d\theta$$

$$- L_{10}\int_0^{2\pi}\sin n\theta\cos n\theta\sin 4\theta\cos 4\theta\, d\theta)\Big/\int_0^{2\pi}\sin^2 n\theta\, d\theta$$

$$+ Q_1[(L_{11}-L_1)\int_0^{2\pi}\sin(n+4)\theta\sin n\theta\, d\theta + L_{12}\int_0^{2\pi}\sin(n+4)\theta\sin n\theta\cos 4\theta\, d\theta$$

$$- L_{13}\int_0^{2\pi}\cos(n+4)\theta\sin n\theta\sin 4\theta\, d\theta]\Big/\int_0^{2\pi}\sin^2 n\theta\, d\theta$$

$$+ Q_2[(L_{14}-L_1)\int_0^{2\pi}\sin(n-4)\theta\sin n\theta\, d\theta + L_{15}\int_0^{2\pi}\sin(n-4)\theta\sin n\theta\cos 4\theta\, d\theta$$

$$- L_{16}\int_0^{2\pi}\cos(n-4)\theta\sin n\theta\sin 4\theta\, d\theta]\Big/\int_0^{2\pi}\sin^2 n\theta\, d\theta\ . \qquad \text{(E12a)}$$

If n =2, then

$$\Sigma_2^1 = L_6 + (L_7 \int_0^{2\pi} \sin^2 n\theta \cos 4\theta \, d\theta + L_8 \int_0^{2\pi} \sin^2 n\theta \cos^2 4\theta \, d\theta - L_9 \int_0^{2\pi} \sin n\theta \cos n\theta \sin 4\theta \, d\theta$$

$$- L_{10} \int_0^{2\pi} \sin n\theta \cos n\theta \sin 4\theta \cos 4\theta \, d\theta \Big/ \int_0^{2\pi} \sin^2 n\theta \, d\theta$$

$$+ Q_1[(L_{11} - L_1 + \frac{1}{2}L_2 + \frac{1}{2}L_3) \int_0^{2\pi} \sin(n+4)\theta \sin n\theta \, d\theta + L_{12} \int_0^{2\pi} \sin(n+4)\theta \sin n\theta \cos 4\theta \, d\theta$$

$$- L_{13} \int_0^{2\pi} \cos(n+4)\theta \sin n\theta \sin 4\theta \, d\theta] \Big/ \int_0^{2\pi} \sin^2 n\theta \, d\theta \, . \qquad \text{(E12b)}$$

where Q_1, Q_2, L_1, L_2 and L_3 are listed in (4.46) and (4.51), and

$$L_6 = A_1 n^4 - E_1 n^2 + K_1,$$

$$L_7 = A_2 n^4 - E_2 n^2 + K_2,$$

$$L_8 = A_3 n^4 - E_3 n^2 + K_3,$$

$$L_9 = D_1 n^3 - G_1 n,$$

$$L_{10} = D_3 n^3 - G_3 n,$$

$$L_{11} = A_4 (n+4)^4 - E_4 (n+4)^2 + K_4,$$

$$L_{12} = A_5 (n+4)^4 - E_5 (n+4)^2 + K_5,$$

$$L_{13} = D_3 (n+4)^3 - G_3 (n+4),$$

$$L_{14} = A_4 (n-4)^4 - E_4 (n-4)^2 + k_4,$$

$$L_{15} = A_5 (n-4)^4 - E_5 (n-4)^2 + K_5,$$

$$L_{16} = D_3(n-4)^3 - G_3(n-4).$$

Equation (E12) gives

$$\Sigma_2^1 = S_1 + S_2, \text{ if } n \neq 0, 2, 4, \tag{E13a}$$

$$\Sigma_2^1 = S_3 + S_4, \text{ if } n = 4, \tag{E13b}$$

$$\Sigma_2^1 = S_1 + S_5, \text{ if } n = 2, \tag{E13c}$$

where

$$S_1 = L_5 + \frac{1}{2}L_3 + \frac{1}{2}Q_1(L_{10} + L_{12}), \tag{E14a}$$

$$S_2 = \frac{1}{2}Q_2(L_{14} - L_{16}), \tag{E14b}$$

$$S_3 = L_5 + \frac{1}{2}Q_1(L_{10} + L_{12}), \tag{E14c}$$

$$S_4 = \frac{1}{4}(L_3 - L_7), \tag{E14d}$$

$$S_5 = -\frac{1}{2}(L_4 + L_8). \tag{E14e}$$

The second branch Σ_2^2 is found by substitution of $F_0 = F_0^2 = \cos n\theta$, $\Sigma_1 = \Sigma_1^2$, and $F_1 = F_1^2$ into (E11). This branch also has two cases. If $n \neq 2$, then

$$\Sigma_2^2 = L_6 + (L_7 \int_0^{2\pi} \cos^2 n\theta \cos 4\theta \, d\theta + L_8 \int_0^{2\pi} \cos^2 n\theta \cos^2 4\theta \, d\theta + L_9 \int_0^{2\pi} \sin n\theta \cos n\theta \sin 4\theta \, d\theta$$
$$+ L_{10} \int_0^{2\pi} \sin n\theta \cos n\theta \sin 4\theta \cos 4\theta \, d\theta) \Big/ \int_0^{2\pi} \cos^2 n\theta \, d\theta$$

$$+ Q_1[(L_{11} - L_1) \int_0^{2\pi} \cos(n+4)\theta \cos n\theta \, d\theta + L_{12} \int_0^{2\pi} \cos(n+4)\theta \cos n\theta \cos 4\theta \, d\theta$$

$$+ L_{13}\int_0^{2\pi}\sin(n+4)\theta\,\cos n\theta\,\sin 4\theta\,d\theta\,]\Big/\int_0^{2\pi}\cos^2 n\theta\,d\theta$$

$$+ Q_2[(L_{14}-L_1)\int_0^{2\pi}\cos(n-4)\theta\,\cos n\theta\,d\theta + L_{15}\int_0^{2\pi}\cos(n-4)\theta\,\cos n\theta\,\cos 4\theta\,d\theta$$

$$+ L_{16}\int_0^{2\pi}\sin(n-4)\theta\,\cos n\theta\,\sin 4\theta\,d\theta]\Big/\int_0^{2\pi}\cos^2 n\theta\,d\theta\ . \qquad \text{(E15a)}$$

If n =2, then

$$\Sigma_2^2 = L_6 + (L_7\int_0^{2\pi}\cos^2 n\theta\,\cos 4\theta\,d\theta + L_8\int_0^{2\pi}\cos^2 n\theta\,\cos^2 4\theta\,d\theta + L_9\int_0^{2\pi}\cos n\theta\,\sin n\theta\,\sin 4\theta\,d\theta$$
$$+ L_{10}\int_0^{2\pi}\sin n\theta\,\cos n\theta\,\sin 4\theta\,\cos 4\theta\,d\theta)\Big/\int_0^{2\pi}\cos^2 n\theta\,d\theta$$

$$+ Q_1[(L_{11}-L_1-\frac{1}{2}L_2-\frac{1}{2}L_3)\int_0^{2\pi}\cos(n+4)\theta\,\cos n\theta\,d\theta + L_{12}\int_0^{2\pi}\cos(n+4)\theta\,\cos n\theta\,\cos 4\theta\,d\theta$$
$$+ L_{13}\int_0^{2\pi}\sin(n+4)\theta\,\cos n\theta\,\sin 4\theta\,d\theta\,]\Big/\int_0^{2\pi}\cos^2 n\theta\,d\theta\ . \qquad \text{(E15b)}$$

Equation (E15) gives

$\Sigma_2^2 = S_1 + S_2$, if n $\neq$ 2, 4, (E16a)

$\Sigma_2^2 = S_3 - S_6$, if n = 4, (E16b)

$\Sigma_2^2 = S_1 - S_5$, if n = 2, (E16c)

where

$$S_6 = \frac{1}{2}(L_{10} - L_8)\,.$$

Thus, the second-order eigenvalue Σ_2 has two branches, and each branch is divided into three different cases depending on n.

The second-order eigenfunction F_2 obeys (4.34c) and can be determined similar to F_1. The first branch has three cases depending on n. If n $\neq$ 0, 2 or 4, then the source term is

$$\Sigma_2 F_0 + T_2 = -[Q_1(L_{11} - L_1) + \frac{1}{2}L_7 - \frac{1}{4}L_9]\sin(n+4)\theta - \frac{1}{2}[(L_{12} - L_{13}) + \frac{1}{4}(L_8 - L_{10})]\sin(n+8)\theta$$
$$-[L_{14} + \frac{1}{2}(L_7 + L_9)]\sin(n-4)\theta - [\frac{1}{2}(L_{15} + L_{16}) + \frac{1}{4}(L_8 + L_{10})]\sin(n-8)\theta \quad \text{(E17a)}$$

If n = 4, then

$$\Sigma_2 F_0 + T_2 = -[Q_1(L_{11} - L_1) + \frac{1}{2}L_7 - \frac{1}{4}L_9]\sin(n+4)\theta - \frac{1}{2}[(L_{12} - L_{13}) + \frac{1}{4}(L_8 - L_{10})]\sin(n+8)\theta \quad \text{(E17b)}$$

If n= 2, then

$$\Sigma_2 F_0 + T_2 = -\{Q_1[L_{11} - L_1 + \frac{1}{2}(L_2 + L_3)] + \frac{1}{2}L_7 - \frac{1}{4}(L_8 + L_{10} + L_9)\}\sin(n+4)\theta$$

$$-\frac{1}{2}[L_8 - L_{10} + L_{12} - L_{13}]\sin(n+8)\theta\,. \quad \text{(E17c)}$$

Thus,

$$F_2^1 = Q_3\sin[(n+4)\theta] + Q_4\sin[(n+8)\theta] + Q_5\sin[(n-4)\theta] + Q_6\sin[(n-8)\theta], \text{ if } n \neq 0, 2, 4, \quad \text{(E18a)}$$

$$F_2^1 = Q_3\sin[(n+4)\theta] + Q_4\sin[(n+8)\theta], \text{ if } n = 4, \quad \text{(E18b)}$$

$$F_2^1 = Q_7\sin[(n+4)\theta] + Q_8\sin[(n+8)\theta], \text{ if } n = 2, \quad \text{(E18c)}$$

where

$$Q_3 = (L_{11} - L_1) + \frac{1}{2}L_7 - \frac{1}{4}L_9,$$

$$Q_4 = \frac{1}{2}(L_{12} - L_8) + \frac{1}{4}(L_8 - L_{10}),$$

$$Q_5 = (L_{14} - L_1) + \frac{1}{2}(L_7 + L_9)\,,$$

$$Q_6 = \frac{1}{2}(L_6 + L_{16}) + \frac{1}{4}(L_8 + L_{10})\,,$$

$$Q_7 = -\{Q_1[L_{11} - L_1 + \frac{1}{2}(L_2 + L_3)] + \frac{1}{2}L_7 - \frac{1}{4}(L_8 + L_{10} + L_9)\}/L_4\,,$$

$$Q_8 = -\frac{1}{2}[L_8 - L_{10} + L_{12} - L_{13}]/L_{17}\,,$$

with

$$L_{17} = A_6(n+8)^4 - E_6(n+8)^2 + k - \Sigma_0\,.$$

The second branch also has three cases. If n $\neq$ 2 or 4, then the source term in (4.34c) is

$$\Sigma_2 F_0 + T_2 = -[Q_1(L_{11} - L_1) + \frac{1}{2}L_7 - \frac{1}{4}L_9]\cos(n+4)\theta - \frac{1}{2}[(L_{12} - L_{13}) + \frac{1}{4}(L_8 - L_{10})]\cos(n+8)\theta$$
$$-[L_{14} + \frac{1}{2}(L_7 + L_9)]\cos(n-4)\theta - [\frac{1}{2}(L_{15} + L_{16}) + \frac{1}{4}(L_8 + L_{10})]\cos(n-8)\theta\,. \quad \text{(E19a)}$$

If n = 4, then

$$\Sigma_2 F_0 + T_2 = -[Q_1(L_{11} - L_1) + \frac{1}{2}L_7 - \frac{1}{4}L_9]\cos(n+4)\theta - \frac{1}{2}[(L_{12} - L_{13}) + \frac{1}{4}(L_8 - L_{10})]\cos(n+8)\theta$$
$$-Q_2(L_{11} - L_1) - \frac{1}{2}(L_7 + L_9)\,. \quad \text{(E19b)}$$

If n= 2, then

$$\Sigma_2 F_0 + T_2 = -\{Q_1(L_{11} - L_1) - \frac{1}{2}(L_2 + L_3 + L_9 - L_7) - \frac{1}{4}(L_8 + L_{10})\}\cos(n+4)\theta$$
$$-[\frac{1}{2}(L_8 - L_{10}) + \frac{1}{2}(L_{12} - L_{13})]\cos(n+8)\theta\,. \quad \text{(E19c)}$$

Thus,

$$F_2^2 = Q_3\cos[(n+4)\theta\,] + Q_4\cos[(n+8)\theta\,] + Q_5\cos[(n-4)\theta\,] + Q_6\cos[(n-8)\theta\,],\ \text{if } n \neq 2,$$

4, (E20a)

$$F_2^2 = Q_3\cos[(n+4)\theta\,] + Q_4\cos[(n+8)\theta\,] + Q_9,\ \text{if } n = 4, \quad \text{(E20b)}$$

$$F_2^2 = Q_{10}\cos[(n+4)\theta\,] + Q_8\cos[(n+8)\theta\,],\ \text{if } n = 2, \quad \text{(E20c)}$$

where

$$Q_9 = -[Q_2(L_{11} - L_1) + \frac{1}{2}(L_7 + L_9)]/(k - \Sigma_0),$$

$$Q_{10} = -[Q_1(L_{11} - L_1) - \frac{1}{2}(L_2 + L_3 + L_9 - L_7) - \frac{1}{4}(L_8 + L_{10})]/L_4.$$

This complete the second-order expansions.

APPENDIX F. COMPUTER PROGRAMS

F1. Program for solving the ODE of interdiffuision for N-layer compounds.

```
C BELOW IS THE DEFINING PROCESS
REAL*8 H, A1,B1, E1,E2, Y,C,Z, K1,K2,K3,K4, L1,L2,L3,L4
INTEGER N,M,N1,N2,LA, I,J,K,Q
DIMENSION Y(0:30000),C(0:30000),Z(0:30000), A(30000),B(30000),E(30000)
DIMENSION K1(30000),K2(30000),K3(30000),K4(30000)
DIMENSION L1(30000),L2(30000),L3(30000),L4(30000)
DIMENSION D(3),DF(3),DIF(3), R(1:100),P(1:100),CC(1:200)
DIMENSION YY(1:100),ZZ(1:100),MII(1:100)
REAL*8 D,DF,DIF,G,F,GG,FF, R,P,CC, YY,ZZ,MII, A,B,E
REAL*8  C1,C2,C3,C4, Y1,Y2,Y3,Y4, Z1,Z2,Z3,Z4

C BELOW  IS THE GIVING VALUE PROCESS
LA=3
R(1)=0
R(2)=5
R(3)=10
P(1)=1
P(2)=10
P(3)=5
CC(1)=0.9
CC(2)=0.8
CC(3)=0.7
CC(4)=0.6
CC(5)=0.5
CC(6)=0.4
CC(7)=0.3
CC(8)=0.2
A1=2.4
B1=3
H=0.01
YY(1)=-1
N1=30000
N2=50000
E1=1.0E-8
E2=1.0E-8
N=3000
M=3000
C1=0
C2=0
C3=0
C4=0
```

```
Y1=0
Y2=0
Y3=0
Y4=0
Z1=0
Z2=0
Z3=0
Z4=0

C BELOW IS THE ITERATION PROCESS
A(1)=A1
B(1)=B1

DO 20 K=1,N

DO 30 J=1,3

D(1)=A(K)
D(2)=B(K)
C(0)=CC(2)
Y(0)=YY(1)

DO 10 I=1,N1

Z(0)=D(J)*(C(0)-CC(1))/(C(0)*(1-R(1))+R(1))
Y(I)=Y(0)+H*I
K1(I)=Z(I-1)
L1(I)=((R(1)-1)*Z(I-1)**2-D(J)*Y(I-1)*Z(I-1))/(C(I-1)*(1-R(1))+R(1))
K2(I)=Z(I-1)+H/2*L1(I)
L2(I)=((R(1)-1)*(Z(I-1)+H/2*L1(I))**2-D(J)*(Y(I-1)+H/2)*(Z(I-1)+H/
*2*L1(I)))/((C(I-1)+H/2*K1(I))*(1-R(1))+R(1))
K3(I)=Z(I-1)+H/2*L2(I)
L3(I)=((R(1)-1)*(Z(I-1)+H/2*L2(I))**2-D(J)*(Y(I-1)+H/2)*(Z(I-1)+H/
*2*L2(I)))/((C(I-1)+H/2*K2(I))*(1-R(1))+R(1))
K4(I)=Z(I-1)+H*L3(I)
L4(I)=((R(1)-1)*(Z(I-1)+H*L3(I))**2-D(J)*(Y(I-1)+H)*(Z(I-1)+H*L3(I
*)))/((C(I-1)+H*K3(I))*(1-R(1))+R(1))
C(I)=C(I-1)+H/6*(K1(I)+2*K2(I)+2*K3(I)+K4(I))
Z(I)=Z(I-1)+H/6*(L1(I)+2*L2(I)+2*L3(I)+L4(I))
C1=C2
C2=C3
C3=C4
C4=C(I)
Y1=Y2
Y2=Y3
Y3=Y4
```

```
Y4=Y(I)
Z1=Z2
Z2=Z3
Z3=Z4
Z4=Z(I)

IF(C(I-1).LT.CC(3)) GOTO 60

10 CONTINUE

60 YY(2)=Y1*(CC(3)-C2)*(CC(3)-C3)*(CC(3)-C4)/(C1-C2)/(C1-C3)/(C1-C4)+
*Y2*(CC(3)-C1)*(CC(3)-C3)*(CC(3)-C4)/(C2-C1)/(C2-C3)/(C2-C4)+Y3*(CC
*(3)-C1)*(CC(3)-C2)*(CC(3)-C4)/(C3-C1)/(C3-C2)/(C3-C4)+Y4*(CC(3)-C1
*)*(CC(3)-C2)*(CC(3)-C3)/(C4-C1)/(C4-C2)/(C4-C3)
ZZ(2)=Z1*(CC(3)-C2)*(CC(3)-C3)*(CC(3)-C4)/(C1-C2)/(C1-C3)/(C1-C4)+
*Z2*(CC(3)-C1)*(CC(3)-C3)*(CC(3)-C4)/(C2-C1)/(C2-C3)/(C2-C4)+Z3*(CC
*(3)-C1)*(CC(3)-C2)*(CC(3)-C4)/(C3-C1)/(C3-C2)/(C3-C4)+Z4*(CC(3)-C1
*)*(CC(3)-C2)*(CC(3)-C3)/(C4-C1)/(C4-C2)/(C4-C3)
MII(1)=I-1

IF(LA.EQ.1) GOTO 42

C(MII(1))=CC(4)
Y(MII(1))=YY(2)
Z(MII(1))=((CC(3)*(1-R(1))+R(1))*ZZ(2)-YY(2)*D(J)*(CC(4)-CC(3)))/(
*CC(4)*(P(2)-R(2))+R(2))

DO 41 Q=2,LA

C1=0
C2=0
C3=0
C4=0
Y1=0
Y2=0
Y3=0
Y4=0
Z1=0
Z2=0
Z3=0
Z4=0

DO 40 I=MII(Q-1)+1,N2

Y(I)=Y(MII(Q-1))+H*(I-MII(Q-1))
K1(I)=Z(I-1)
```

```
L1(I)=((R(Q)-P(Q))*Z(I-1)**2-D(J)*Y(I-1)*Z(I-1))/(C(I-1)*(P(Q)-R(Q
*))+R(Q))
K2(I)=Z(I-1)+H/2*L1(I)
L2(I)=((R(Q)-P(Q))*(Z(I-1)+H/2*L1(I))**2-D(J)*(Y(I-1)+H/2)*(Z(I-1)
*+H/2*L1(I)))/((C(I-1)+H/2*K1(I))*(P(Q)-R(Q))+R(Q))
K3(I)=Z(I-1)+H/2*L2(I)
L3(I)=((R(Q)-P(Q))*(Z(I-1)+H/2*L2(I))**2-D(J)*(Y(I-1)+H/2)*(Z(I-1)
*+H/2*L2(I)))/((C(I-1)+H/2*K2(I))*(P(Q)-R(Q))+R(Q))
K4(I)=Z(I-1)+H*L3(I)
L4(I)=((R(Q)-P(Q))*(Z(I-1)+H*L3(I))**2-D(J)*(Y(I-1)+H)*(Z(I-1)+H*L
*3(I)))/((C(I-1)+H*K3(I))*(P(Q)-R(Q))+R(Q))
C(I)=C(I-1)+H/6*(K1(I)+2*K2(I)+2*K3(I)+K4(I))
Z(I)=Z(I-1)+H/6*(L1(I)+2*L2(I)+2*L3(I)+L4(I))
C1=C2
C2=C3
C3=C4
C4=C(I)
Y1=Y2
Y2=Y3
Y3=Y4
Y4=Y(I)
Z1=Z2
Z2=Z3
Z3=Z4
Z4=Z(I)

IF(C(I-1).LT.CC(2*(Q+1)-1)) GOTO 70

40 CONTINUE

70 YY(Q+1)=Y1*(CC(2*(Q+1)-1)-C2)*(CC(2*(Q+1)-1)-C3)*(CC(2*(Q+1)-1)-C4
*)/(C1-C2)/(C1-C3)/(C1-C4)+Y2*(CC(2*(Q+1)-1)-C1)*(CC(2*(Q+1)-1)-C3)
**(CC(2*(Q+1)-1)-C4)/(C2-C1)/(C2-C3)/(C2-C4)+Y3*(CC(2*(Q+1)-1)-C1)*
*(CC(2*(Q+1)-1)-C2)*(CC(2*(Q+1)-1)-C4)/(C3-C1)/(C3-C2)/(C3-C4)+Y4*
*(CC(2*(Q+1)-1)-C1)*(CC(2*(Q+1)-1)-C2)*(CC(2*(Q+1)-1)-C3)/(C4-C1)/(
*C4-C2)/(C4-C3)
ZZ(Q+1)=Z1*(CC(2*(Q+1)-1)-C2)*(CC(2*(Q+1)-1)-C3)*(CC(2*(Q+1)-1)-C4
*)/(C1-C2)/(C1-C3)/(C1-C4)+Z2*(CC(2*(Q+1)-1)-C1)*(CC(2*(Q+1)-1)-C3)
**(CC(2*(Q+1)-1)-C4)/(C2-C1)/(C2-C3)/(C2-C4)+Z3*(CC(2*(Q+1)-1)-C1)*
*(CC(2*(Q+1)-1)-C2)*(CC(2*(Q+1)-1)-C4)/(C3-C1)/(C3-C2)/(C3-C4)+Z4*(
*CC(2*(Q+1)-1)-C1)*(CC(2*(Q+1)-1)-C2)*(CC(2*(Q+1)-1)-C3)/(C4-C1)/(C
*4-C2)/(C4-C3)
MII(Q)=I-1

IF(Q.EQ.LA) GOTO 42
```

```
C(MII(Q))=CC(2*(Q+1))
Y(MII(Q))=YY(Q+1)
Z(MII(Q))=((CC(2*(Q+1)-1)*(P(Q)-R(Q))+R(Q))*ZZ(Q+1)-YY(Q+1)*D(J)*(
*CC(2*(Q+1))-CC(2*(Q+1)-1)))/(CC(2*(Q+1))*(P(Q+1)-R(Q+1))+R(Q+1))

41 CONTINUE

42  DF(J)=(R(LA)+CC(2*(LA+1)-1)*(P(LA)-R(LA)))*ZZ(LA+1)/YY(LA+1)/(CC(2
* *(LA+1))-CC(2*(LA+1)-1))
DIF(J)=D(J)-DF(J)

IF(J.EQ.2) THEN

E(K)=A(K)+ABS(DIF(1))*(B(K)-A(K))/(ABS(DIF(1))+ABS(DIF(2)))
D(3)=E(K)

ELSE

ENDIF

30 CONTINUE

IF(ABS(DIF(3)).LE.E1) GOTO 80

IF(DIF(1)*DIF(3).LT.0) THEN

A(K+1)=A(K)
B(K+1)=E(K)

ELSEIF(DIF(1)*DIF(3).GT.0) THEN

A(K+1)=E(K)
B(K+1)=B(K)

ENDIF

IF(ABS(A(K+1)-B(K+1)).LE.E2) GOTO 50

20  CONTINUE

C     BELOW IS THE PROCESS OF PRINTING IN THE SCREEN
80   WRITE(*,500) K,E(K)
500 FORMAT(3X,'K=',I3,1X,'E(K)=',F10.8)
50 WRITE(*,600) K,A(K+1)
600 FORMAT(3X,'K=',I3,1X,'D=',F12.8)
DD=A(K+1)
```

```
G=YM*YM*DD
F=YE*YE*DD
DDD=E(K)
GG=YY(2)*YY(2)*DDD
FF=YY(3)*YY(3)*DDD

DO 5000 I=1,LA+1

WRITE(*,5001) YY(I)
5001 FORMAT(3X,'YY','(','I',')',F12.8)

5000 CONTINUE

WRITE(*,6000) DD,G,F
6000 FORMAT(3X,'D=',F12.8,1X,'E=',F12.8,1X,'F=',F12.8)
WRITE(*,7000) DDD,GG,FF
7000 FORMAT(3X,'DD=',F12.8,1X,'EE=',F12.8,1X,'FF=',F12.8)

END
```

F2. Program for computing growth rate of perturbation of retracting films.

```
program main

implicit complex(8) (a-z)
complex(8) a(1:4),m(1:4,1:4), s,det
double precision k,b,srp,sip,drp,dip, lf1,lf2,rt1,rt2
integer ri,mi,j,cn1,cned1,cn2,cned2,cn3,cned3, cn4,cned4, n1,n2
double precision srp0(1:20000),sip0(1:20000), srp1(1:20000),sip1(1:20000)
double precision srp2(1:20000),sip2(1:20000), srp3(1:20000),sip3(1:20000)
double precision detr(1:20000),deti(1:20000), drpr,dipr, a3(1:20000),a4(1:20000)

drpr=0d0
dipr=0d0
n1=1000
lf1=4.4100d-5
rt1=4.4300d-5
k=0.04d0
b=0.1d0
cn4=0
sip=0d0

do 10 ri=0,n1

srp=lf1+ri*(rt1-lf1)/n1
s=cmplx(srp,sip,8)
a(3)=a3f(k,b,s)
a(4)=a4f(k,b,s)

if(dreal(a(2)).ge.0d0.and.dreal(a(3)).le.0d0) then

m(1,1)=b**2d0-6d0*b-6d0*a(3)
m(1,2)=b**2d0-6d0*b-6d0*a(4)
m(2,1)=b**3d0+k**2d0*a(3)-a(3)**3d0
m(2,2)=b**3d0+k**2d0*a(4)-a(4)**3d0

endif

det=detf(m)
drp=dreal(det)
dip=dimag(det)
drpr=drp
dipr=dip

cn4=cn4+1
srp0(cn4)=srp
```

```
sip0(cn4)=sip
detr(cn4)=drp
deti(cn4)=dip

10      enddo

cned4=cn4
open(23,file='detr.dat',status='unknown')

do cn4=1,cned4

write(23,*) srp0(cn4),detr(cn4)

enddo

close(23)

open(24,file='deti.dat',status='unknown')

do cn4=1,cned4

write(24,*) srp0(cn4),abs(deti(cn4))

enddo

close(24)

end

complex(8) function a3f(k,b,s)

implicit complex(8) (a-z)
complex(8) s
double precision k,b

t1=sqrt(-768*s**3-768*s**2*k**4+864*k**2*s*b**6+
#768*k**6*b**6+81*b**12)
t2=576d0*k**2d0*s+512d0*k**6d0+108d0*b**6d0+12d0*t1
t3=cmplx(0d0,0d0)+((8d0*k**2d0*t2**(1d0/3d0)+t2**(2d0/3d0)+
#48d0*s+64d0*k**4d0)/t2**(1d0/3d0))**(0.5d0)
t41=((-1d0)*(-96d0*k**2d0*t2**(1d0/3d0)*t3+6d0*t3*t2**(2d0/3d0
#)+288d0*s*t3+384d0*k**4d0*t3-
#72d0*dsqrt(6d0)*b**3d0*t2**(1d0/3d0))/t2**(1d0/3d0)/t3)**(0.5d0)
t42=((-1d0)*(-96d0*k**2d0*t2**(1d0/3d0)*t3+6d0*t3*t2**(2d0/3d0
#)+288d0*s*t3+384d0*k**4d0*t3+
#72d0*dsqrt(6d0)*b**3d0*t2**(1d0/3d0))/t2**(1d0/3d0)/t3)**(0.5d0)
```

```
a3=-dsqrt(6d0)/12d0*t3+1d0/12d0*t42
a3f=a3

return

end

complex(8) function a4f(k,b,s)

implicit complex(8) (a-z)
complex(8) s
double precision k,b

t1=sqrt(-768*s**3-768*s**2*k**4+864*k**2*s*b**6+
#768*k**6*b**6+81*b**12)
t2=576d0*k**2d0*s+512d0*k**6d0+108d0*b**6d0+12d0*t1
t3=cmplx(0d0,0d0)+((8d0*k**2d0*t2**(1d0/3d0)+t2**(2d0/3d0)+
#48d0*s+64d0*k**4d0)/t2**(1d0/3d0))**(0.5d0)
t41=((-1d0)*(-96d0*k**2d0*t2**(1d0/3d0)*t3+6d0*t3*t2**(2d0/3d0
#)+288d0*s*t3+384d0*k**4d0*t3-
#72d0*dsqrt(6d0)*b**3d0*t2**(1d0/3d0))/t2**(1d0/3d0)/t3)**(0.5d0)
t42=((-1d0)*(-96d0*k**2d0*t2**(1d0/3d0)*t3+6d0*t3*t2**(2d0/3d0
#)+288d0*s*t3+384d0*k**4d0*t3+
#72d0*dsqrt(6d0)*b**3d0*t2**(1d0/3d0))/t2**(1d0/3d0)/t3)**(0.5d0)
a4=-dsqrt(6d0)/12d0*t3-1d0/12d0*t42

a4f=a4

return

end

complex(8) function detf(m)

implicit complex(8) (a-z)
complex(8) m(1:4,1:4)
integer i,j

detf=m(1,1)*m(2,2)-m(1,2)*m(2,1)

return

end
```

F3. Program to compute the equilibrium shape of solid wires

```
PROGRAM MAIN

IMPLICIT DOUBLE PRECISION (A-Z)
EXTERNAL F1,F2
DOUBLE PRECISION A,B,F1,F2,S1,R,L,H,M1,M2,XJ
DOUBLE PRECISION PI
DOUBLE PRECISION C,D,X1,Y1,REE
INTEGER I,J,N,COTESN,K
DOUBLE PRECISION S(0:10000),RE(0:2000),XX(0:2000),YY(0:2000)
DOUBLE PRECISION F(0:10000),E,SV,ST,X,Y ,PH(0:2000)
DOUBLE PRECISION ROTATEANGLE,PHT,FT,DSDPH

PI=2D0*DASIN(1D0)
A=0.0D0/2D0
B=PI/2D0
ROTATEANGLE=PI/4D0
R=0.05D0
N=1142
COTESN=5000

CALL COTES(A,B,F2,COTESN,S1)

L=(1D0-R)/S1
PRINT*,'L',L

DO J=0,N

XJ=DCOS(PI*J/N)
S(J)=(XJ+1)*PI/4D0

ENDDO

DO 20 J=N,N/2,-1

PRINT*,'POINT',J

SV=S(J)-ROTATEANGLE
C=0D0-ROTATEANGLE

IF(J.EQ.N) THEN
PHT=C
ELSE
PHT=PH(J+1)-ROTATEANGLE
ENDIF
```

```
E=1D-14
I=0
K=0

10 CALL COTES(0D0,PHT,F1,COTESN,M1)
CALL COTES(0D0,PHT,F2,COTESN,M2)

I=I+1
PRINT*,'I=',I
X=1D0-R*(1-DCOS(PHT))-L*M1
Y=R*DSIN(PHT)+L*M2
REE=(X**2D0+Y**2D0)**(0.5D0)

IF(X.GT.0.0D0.AND.Y.GE.0.0D0) THEN
ST=DATAN(Y/X)
ELSEIF(X.LT.0.0D0.AND.Y.GE.0.0D0) THEN
ST=PI+DATAN(Y/X)
ELSEIF(X.LT.0.AND.Y.LT.0) THEN
ST=PI+DATAN(Y/X)
ELSEIF(X.GT.0.0D0.AND.Y.LT.0.0D0) THEN
ST=DATAN(Y/X)
ELSEIF(X.EQ.0.0D0.AND.Y.GT.0.0D0) THEN
ST=PI/2D0
ELSEIF(X.EQ.0.0D0.AND.Y.LT.0.0D0) THEN
ST=-PI/2D0
ENDIF

FT=R+L*F3(PHT)
DSDPH=FT*(X*COS(PHT)+Y*SIN(PHT))/REE**2
PHT=PHT+(SV-ST)/DSDPH
WRITE(*,*) PHT+ROTATEANGLE,ST+ROTATEANGLE,SV+ROTATEANGLE

IF(DABS(ST-SV).GT.E.AND.I.LT.45) GOTO 10
RE(J)=REE
PH(J)=PHT+ROTATEANGLE

20      CONTINUE

DO I=0,N/2

RE(I)=RE(N-I)
PH(I)=PI/2D0-PH(N-I)

ENDDO
DO K=0,N
```

```
XX(K)=RE(K)*COS(S(K))
YY(K)=RE(K)*SIN(S(K))

ENDDO

OPEN(67,FILE='R005.DAT',STATUS='UNKNOWN')

DO I=0,N
WRITE(67,6003) RE(I)
ENDDO
6003 FORMAT(3X,F20.16)

CLOSE(67)

OPEN(68,FILE='XYR005.DAT',STATUS='UNKNOWN')

DO I=0,N
WRITE(68,6004) XX(I),YY(I)
ENDDO
6004 FORMAT(3X,F20.16,3X,F20.16)

CLOSE(68)

OPEN(69,FILE='PHR005.DAT',STATUS='UNKNOWN')

DO I=0,N
WRITE(69,6005) PH(I)
ENDDO
6005   FORMAT(3X,F20.16)

CLOSE(69)

END

DOUBLE PRECISION FUNCTION F1(X)

IMPLICIT DOUBLE PRECISION (A-Z)
DOUBLE PRECISION X,FUN,M,TEMP,PI,EPS
INTEGER IST,IED,I

PI=DASIN(1D0)*2D0
FUN=0D0
IST=-12D0
IED=14D0
EPS=0.05D0
```

```
DO 1 I=IST,IED

M=(X+I*PI/2D0)/EPS

IF(M.LE.0D0) THEN
TEMP=2D0*DEXP(M)/(DEXP(2D0*M)+1D0)
ELSE
TEMP=2D0*DEXP(-M)/(DEXP(-2D0*M)+1D0)
ENDIF

FUN=FUN+TEMP

1    CONTINUE

FUN=FUN*DSIN(X)

F1=FUN

RETURN

END

DOUBLE PRECISION FUNCTION F2(X)

IMPLICIT DOUBLE PRECISION (A-Z)
DOUBLE PRECISION X,FUN,M,EPS,PI
INTEGER I,IST,IED

PI=DASIN(1D0)*2D0
FUN=0D0
IST=-12D0
IED=14D0
EPS=0.05D0

DO 1 I=IST,IED

M=(X+I*PI/2D0)/EPS

IF(M.LE.0D0) THEN
FUN=FUN+2D0*DEXP(M)/(DEXP(2D0*M)+1D0)
ELSE
FUN=FUN+2D0*DEXP(-M)/(DEXP(-2D0*M)+1D0)
ENDIF

1    CONTINUE
```

```
FUN=FUN*DCOS(X)
F2=FUN

RETURN

END

DOUBLE PRECISION FUNCTION F3(X)

IMPLICIT DOUBLE PRECISION (A-Z)
DOUBLE PRECISION X,FUN,M,PI,EPS
INTEGER IST,IED,I

PI=ASIN(1D0)*2D0
FUN=0D0
IST=-12D0
IED=14D0
EPS=0.05D0

DO 1 I=IST,IED

M=(X+I*PI/2D0)/EPS

IF(M.LE.0D0) THEN
FUN=FUN+2D0*EXP(M)/(EXP(2D0*M)+1D0)
ELSE
FUN=FUN+2D0*EXP(-M)/(EXP(-2D0*M)+1D0)
ENDIF

1 CONTINUE

F3=FUN

RETURN

END

SUBROUTINE COTES(A,B,F,N,T)

IMPLICIT DOUBLE PRECISION (A-Z)
DOUBLE PRECISION  A,B,F,T,H,TEMP1,TEMP2,TEMP3,TEMP4
DOUBLE PRECISION X1,X2,X3,X4
INTEGER N,I

H=(B-A)/N
```

```
TEMP1=0D0
TEMP2=0D0
TEMP3=0D0
TEMP4=0D0

DO I=0,N-1

X1=A+(I+0.25D0)*H
X2=A+(I+0.5D0)*H
X3=A+(I+0.75D0)*H
TEMP1=TEMP1+F(X1)
TEMP2=TEMP2+F(X2)
TEMP3=TEMP3+F(X3)

ENDDO

DO I=1,N-1

X4=A+I*H
TEMP4=TEMP4+F(X4)

ENDDO

T=H/90D0*(7D0*F(A)+32D0*TEMP1+12D0*TEMP2+32D0*TEMP3
#+14D0*TEMP4+7D0*F(B))

RETURN

END
```

F4. Program to solve the eigenvalue problem of solid wire.

```
PROGRAM MAIN

IMPLICIT REAL*16 (A-Z)
EXTERNAL F2
REAL*16 XJ(0:1142),C(0:1142),TEMP(1:1142),RE(0:1142)
REAL*16 S(0:1142),PI,PHH(0:1142)
REAL*16 D1(0:1142,0:1142),D2(0:1142,0:1142)
REAL*16 D3(0:1142,0:1142),D4(0:1142,0:1142)
REAL*16 D1RE(0:1142),D2RE(0:1142)
REAL*16 D3RE(0:1142),D4RE(0:1142)
REAL*16 C1(0:1142,0:1142),C2(0:1142,0:1142)
REAL*16 C3(0:1142,0:1142),C4(0:1142,0:1142)
REAL*16 C0(0:1142,0:1142)
REAL*16 A1(0:1142,0:1142),A2(0:1142,0:1142)
REAL*16 A3(0:1142,0:1142),A4(0:1142,0:1142)
REAL*16 A(0:1142,0:1142),AM(1142,1142)
REAL*16 WR(1142),WI(1142),Z(1142,1142),FV1(1142)
REAL*16 AA,BB,R,L,S1,w
REAL*16 TEMP1(1:1142),TEMP2(1:1142),TEMP3(1:1142),TEMP4(1:1142)
REAL*16 TEMP5(1:1142),TEMP6(1:1142),TEMP7(1:1142),TEMP8(1:1142)
REAL*16 TEMP9(1:1142),TEMP10(1:1142),TEMP11(1:1142)
INTEGER N,MATZ,IV1(1142),IERR,I,J,COTESN

N=1142
R=0.05Q0
w=1.060Q0
PI=2Q0*ASIN(1Q0)
AA=0.0Q0/2Q0
BB=PI/2Q0
COTESN=5000

CALL COTES(AA,BB,F2,COTESN,S1)

L=(1Q0-R)/S1

CALL XJC(N,XJ,C)
CALL CREATD1(N,XJ,C,D1)

DO J=0,N
S(J)=(XJ(J)+1)*PI/4Q0
ENDDO

CALL READFROMFILE(N,RE,PHH)
CALL CALCULATEDIFF(N,L,R,RE,S,PHH,D1RE,D2RE,D3RE,D4RE)
CALL MATRIXPRODUCT(N,D1,D1,D2)
```

```
CALL MATRIXPRODUCT(N,D1,D2,D3)
CALL MATRIXPRODUCT(N,D1,D3,D4)
CALL CALCULATECOEFF(N,w,RE,D1RE,D2RE,D3RE,D4RE,C0,C1,C2,C3,C4)
CALL MATRIXPRODUCT(N,C1,D1,A1)
CALL MATRIXPRODUCT(N,C2,D2,A2)
CALL MATRIXPRODUCT(N,C3,D3,A3)
CALL MATRIXPRODUCT(N,C4,D4,A4)
CALL COEFFMATRIX(N,C0,A1,A2,A3,A4,A)
CALL IMPOSEBOUNDARYCONDITION(N,A,D1,D2,D3,AM)

MATZ=1

CALL RG(1142,N-3,AM,WR,WI,MATZ,Z,IV1,FV1,IERR)

DO I=1,N-3

 TEMP1(I)=Z(I,N-3)
 TEMP2(I)=Z(I,N-4)
 TEMP3(I)=Z(I,N-5)
 TEMP4(I)=Z(I,N-6)
 TEMP5(I)=Z(I,N-7)
 TEMP6(I)=Z(I,N-8)
 TEMP7(I)=Z(I,N-9)
 TEMP8(I)=Z(I,N-10)
 TEMP9(I)=Z(I,N-11)
 TEMP10(I)=Z(I,N-12)
 TEMP11(I)=Z(I,N-13)

 ENDDO

CALL PRINTTOFILE(11,'F1.DAT',N-3,S,TEMP1)
CALL PRINTTOFILE(12,'F2.DAT',N-3,S,TEMP2)
CALL PRINTTOFILE(13,'F3.DAT',N-3,S,TEMP3)
CALL PRINTTOFILE(14,'F4.DAT',N-3,S,TEMP4)
CALL PRINTTOFILE(15,'F5.DAT',N-3,S,TEMP5)
CALL PRINTTOFILE(16,'F6.DAT',N-3,S,TEMP6)
CALL PRINTTOFILE(17,'F7.DAT',N-3,S,TEMP7)
CALL PRINTTOFILE(18,'F8.DAT',N-3,S,TEMP8)
CALL PRINTTOFILE(19,'F9.DAT',N-3,S,TEMP9)
CALL PRINTTOFILE(20,'F10.DAT',N-3,S,TEMP10)
CALL PRINTTOFILE(21,'F11.DAT',N-3,S,TEMP11)

OPEN(UNIT=28,FILE='EIVALUE.DAT',STATUS='UNKNOWN')

DO I=1,N-3
write(28,*) WR(I),WI(I)
```

```
ENDDO

CLOSE(28)

END

SUBROUTINE READFROMFILE(N,ARRAY1,ARRAY2)

IMPLICIT REAL*16 (A-Z)
REAL*16 ARRAY1(0:1142),ARRAY2(0:1142)
INTEGER N

OPEN(UNIT=7,FILE='R005.DAT',STATUS='UNKNOWN')

DO I=0,N
READ(7,*) ARRAY1(I)
ENDDO

CLOSE(7)

OPEN(UNIT=8,FILE='PHR005.DAT',STATUS='UNKNOWN')

DO I=0,N
READ(8,*) ARRAY2(I)
ENDDO

CLOSE(8)

END

SUBROUTINECALCULATECOEFF(N,w,RE,D1RE,D2RE,D3RE,D4RE,C0,C1,
#C2,C3,C4)

IMPLICIT REAL*16 (A-Z)
REAL*16 D1RE(0:1142),D2RE(0:1142)
REAL*16 D3RE(0:1142),D4RE(0:1142)
REAL*16 RE(0:1142),w
REAL*16 C1(0:1142,0:1142),C2(0:1142,0:1142)
REAL*16 C3(0:1142,0:1142),C4(0:1142,0:1142)
REAL*16 C0(0:1142,0:1142)
INTEGER N,I

DO 100 I=0,N

t1 = RE(I)
t2 = t1**2
```

```
t3 =D1RE(I)
t4 = t3**2
t6 = sqrt(t2+t4)
t9 = D2RE(I)
t13 = 1/t6/(t2+2*t4-t1*t9)
C4(I,I)=t13

 t1 = RE(I)
 t2 = t1**2
 t3 = D1RE(I)
 t4 = t3**2
 t6 = sqrt(t2+t4)
 t7 = t6**2
 t11 = D2RE(I)
 t14 = (t2+2*t4-t1*t11)**2
 t17 = t4**2
 t24 = D3RE(I)
 t31 = t2**2
 t35 = t11**2
 t43 = 2/t7/t6/t14*(4*t17*t3-9*t1*t4*t3*t11+t2*t24*t4-5*t3*t2*t1*t1
 #1-2*t3*t31+2*t3*t2*t35+t31*t24)/t1
 C3(I,I)=t43

 t1 = RE(I)
 t2 = t1**2
 t3 = D1RE(I)
 t4 = t3**2
 t6 = sqrt(t2+t4)
 t7 = t6**2
 t8 = t7**2
 t11 = t2*t1
 t12 = t4**2
 t13 = t12*t4
 t14 = t11*t13
 t16 = t2**2
 t17 = t16*t2
 t18 = t4*t17
 t19 = D2RE(I)
 t22 = t16*t1
 t23 = t4*t22
 t24 = D3RE(I)
 t25 = t24**2
 t28 = t12**2
 t30 = w**2
t33 = t13*t2
t34 = D4RE(I)
```

```
t37 = t19**2
t41 = t16**2
t46 = t16*t11
t53 = t41*t1
t57 = t4*t3
t62 = t37*t19
t65 = 58*t14-31*t18*t19-4*t23*t25+32*t28*t11*t30-2*t33*t34-120*t13
#*t37*t1-4*t41*t2*t30*t19+t46*t34*t19+72*t1*t28+48*t28*t19+14*t4*t5
#3*t30+51*t57*t22*t24-15*t4*t16*t62
t67 = t37**2
t70 = t22*t12
t76 = t12*t16
t79 = t12*t3
t83 = t46*t4
t94 = t12*t11
t99 = -9*t4*t11*t67-15*t70+8*t1*t30*t28*t4-168*t76*t19+50*t79*t11*
#t24-17*t83-t53-5*t76*t34+7*t41*t19-t41*t34+16*t1*t24*t12*t57-2*t94
#*t25-142*t33*t19
t114 = t37*t24
t134 = 2*t94*t37-12*t17*t62+6*t22*t67+50*t13*t22*t30+57*t12*t2*t62
#-t57*t11*t114+17*t3*t46*t24+38*t12*t46*t30+2*t41*t11*t30-2*t46*t25
#+2*t53*t30*t37-4*t18*t34+32*t23*t37
t136 = t24*t19
t143 = t30*t19
t146 = t30*t37
t152 = t34*t19
t171 = 6*t79*t2*t136+10*t57*t16*t136-28*t13*t16*t143+6*t70*t146-36
#*t12*t17*t143+t94*t152-8*t28*t2*t143+2*t14*t146-t3*t22*t114-20*t4*
#t41*t143+4*t17*t3*t136+6*t83*t146+2*t23*t152
t178 = t2+2*t4-t1*t19
t179 = t178**2
t184 = -1/t8/t6*(t65+t99+t134+t171)/t1/t179/t178
C2(I,I)=t184

t1 = RE(I)
t2 = t1**2
t3 = D1RE(I)
t4 = t3**2
t6 = sqrt(t2+t4)
t7 = t6**2
t9 = t7**2
t12 = t2**2
t13 = t12*t2
t14 = D2RE(I)
t15 = D3RE(I)
t16 = t15**2
```

```
t18 = t4*t3
t21 = t12**2
t24 = t21*t2
t28 = t4**2
t29 = t28*t3
t32 = t28**2
t33 = t32*t3
t38 = t32*t18
t39 = w**2
t43 = t28*t18
t49 = t32*t4*t15
t51 = t14**2
t55 = t33*t51
t57 = t2*t1
t63 = t28*t4
t67 = D4RE(I)
t69 = t18*t14
t72 = t2*t39
t76 = t4*t15
t84 = t51*t14
t86 = t28*t15
t89 = 24*t13*t16*t18+41*t18*t21+3*t24*t15+24*t12*t16*t29-136*t33*t
#2+3*t3*t24+72*t38*t39*t2-96*t12*t43+48*t13*t29+16*t49-13*t21*t51*t
#15-48*t55-2*t57*t39*t32*t14*t15-116*t12*t63*t15-12*t13*t67*t69+10*
#t72*t55-26*t13*t51*t76+4*t72*t49-148*t33*t1*t14-3*t57*t84*t86
t90 = t21*t57
t92 = t14*t15
t95 = t21*t1
t96 = t95*t39
t100 = t12*t57
t101 = t100*t39
t102 = t29*t14
t115 = t24*t39
t119 = t12*t39
t120 = t32*t15
t123 = t21*t39
t126 = t1*t14
t136 = t13*t39
t152 = t12*t1
t153 = t152*t39
t154 = t43*t14
t157 = t63*t15
t160 = t51**2
t161 = t160*t14
t168 = -68*t96*t69-122*t33*t39*t57*t14+60*t136*t29*t51-10*t3*t90*t
#39*t14-12*t12*t67*t102+12*t115*t76+40*t123*t18*t51-208*t153*t154+3
```

```
#2*t136*t157-21*t152*t161*t3-4*t2*t67*t154
t233 = 36*t152*t67*t29+40*t119*t43*t51-28*t1*t39*t38*t14+18*t2*t51
#*t157+9*t57*t161*t18+16*t32*t29*t39-8*t153*t63*t14*t15-20*t2*t32*t
#15+138*t43*t84*t1-6*t100*t14*t76-162*t57*t63*t92+48*t123*t29-12*t1
#01*t28*t14*t15-95*t152*t28*t92+2*t21*t12*t39*t15-111*t13*t28*t15+2
#0*t100*t67*t18-28*t21*t4*t15+4*t95*t67*t3-t12*t29*t51
t295 = 128*t119*t33+8*t16*t2*t43-24*t3*t95*t14-57*t2*t160*t29+112*
#t136*t43+427*t152*t29*t14+73*t18*t100*t14+32*t152*t18*t84-197*t57*
#t29*t84+67*t3*t100*t84+332*t57*t43*t14
t302 = t2+2*t4-t126
t303 = t302**2
t308 = -1/t9/t7/t6*(t89-2*t90*t39*t92-8*t96*t92*t4-172*t101*t102-4
#*t21*t67*t3*t14+7*t95*t14*t15+5*t12*t51*t86+10*t115*t51*t3+18*t119
#*t120+28*t123*t86-80*t120*t126+t168+t233+8*t21*t16*t3+8*t115*t18+1
#17*t12*t160*t18+3*t100*t84*t15-212*t13*t18*t51-49*t21*t3*t51+24*t1
#3*t160*t3+28*t57*t67*t43+414*t2*t43*t51+8*t1*t67*t33+t295)/t1/t303
#/t302
C1(I,I)=t308

t1 = RE(I)
t2 = t1**2
t3 = D1RE(I)
t4 = t3**2
t6 = sqrt(t2+t4)
t7 = t6**2
t9 = t7**2
t12 = t2**2
t13 = t12**2
t14 = t13*t1
t15 = w**2
t16 = t14*t15
t17 = D2RE(I)
t18 = D3RE(I)
t19 = D4RE(I)
t20 = t19*t4
t24 = t12*t15
t25 = t4*t3
t26 = t4**2
t27 = t26*t25
t32 = t2*t1
t33 = t32*t15
t34 = t17**2
t35 = t27*t34
t38 = t26*t4
t39 = t34*t17
t43 = t26**2
```

```
t44 = t43*t19
t47 = t13*t15
t48 = t19*t26
t51 = t13*t2
t53 = t15**2
t54 = t53*t17
t57 = t43*t4
t61 = t51*t15
t64 = t18**2
t65 = t43*t64
t68 = t12*t2
t69 = t68*t15
t73 = t12*t32
t75 = t53*t34
t78 = t12*t1
t79 = t78*t15
t83 = t1*t17
t86 = t2*t15
t87 = t43*t3
t89 = t17*t87*t18
t92 = t57*t17
t94 = 4*t16*t20*t17+58*t24*t27*t17*t18+t33*t35*t18-43*t24*t38*t39-
#9*t24*t44-14*t47*t48-40*t26*t51*t54-22*t12*t57*t54-6*t61*t20-2*t33
#*t65-35*t69*t39*t26+10*t38*t73*t75-8*t79*t38*t64-2*t44*t83+14*t86*
#t89-76*t92
t99 = t39*t18
t102 = t38*t19
t110 = t13*t78
t114 = t13*t12
t115 = t114*t15
t136 = -60*t38*t13*t54+6*t25*t12*t99-16*t69*t102-8*t16*t64*t4-2*t1
#4*t64+9*t4*t110*t53-t115*t19-t51*t17+122*t24*t43*t17-t51*t19-t110*
#t15+t33*t44*t17+61*t57*t78*t53+4*t65*t1-96*t32*t43+41*t73*t26+48*t
#78*t38
t161 = t1*t15
t176 = t34**2
t177 = t176*t17
t180 = t73*t15
t192 = 20*t57*t15*t34*t1+5*t43*t78*t75-50*t43*t68*t54+6*t3*t68*t99
#+10*t26*t14*t75-9*t13*t39*t4*t15-2*t35*t18*t1-8*t161*t43*t25*t18+3
#*t14*t4-39*t79*t18*t27-30*t33*t87*t18+t13*t73*t53+6*t177*t68-4*t18
#0*t4*t176-2*t79*t26*t176+7*t14*t34+6*t180*t48*t17
t193 = t26*t3
t194 = t193*t17
t202 = t25*t17
t206 = t39*t43
```

```
t210 = t19*t57
t212 = t18*t3
t236 = t13*t32
t237 = t236*t15
t238 = t19*t17
t246 = 90*t69*t194*t18+3*t180*t25*t34*t18+62*t47*t202*t18+18*t206-
#136*t1*t57+4*t210+16*t61*t212*t17+3*t79*t193*t34*t18+t3*t14*t15*t3
#4*t18+4*t79*t102*t17-12*t73*t176+112*t68*t18*t202-17*t86*t206-2*t8
#6*t210+t237*t238-14*t4*t114*t54+5*t4*t236*t75
t249 = t43*t26
t262 = t18*t17
t272 = t4*t17
t282 = t43*t34
t285 = t32*t38
t288 = t78*t26
t299 = -4*t249*t2*t54+t57*t32*t75-12*t180*t64*t26+3*t16*t18*t25+30
#*t2*t27*t262-30*t16*t4*t34-82*t180*t26*t34+t73*t19*t272+63*t47*t26
#*t17+26*t86*t92+132*t12*t18*t194+18*t33*t282-5*t285*t238-3*t288*t2
#38-54*t79*t38*t34+141*t69*t38*t17+13*t61*t272
t301 = t34*t18
t323 = t2*t43
t345 = t12*t38
t348 = -45*t32*t193*t301-23*t3*t73*t301-66*t25*t78*t301+30*t3*t13*
#t262-2*t237*t64+3*t237*t212-17*t180*t18*t193+99*t68*t39*t4+462*t32
#3*t17-99*t78*t18*t193-80*t180*t38+7*t18*t14*t3-3*t13*t19*t4+159*t3
#2*t176*t26-24*t177*t12*t4+3*t115*t17+470*t345*t17
t394 = -20*t89+34*t26*t236*t53+12*t323*t19+24*t249*t32*t53-12*t73*
#t18*t25-73*t73*t34*t4-10*t237*t4-315*t2*t39*t38-140*t32*t18*t27-60
#*t1*t87*t18-8*t249*t15*t17+t68*t19*t26+t110*t53*t34-24*t161*t249+6
#6*t12*t39*t26-2*t13*t68*t53*t17+11*t345*t19
t438 = t14*t19*t17-2*t73*t64*t4+320*t282*t1-42*t13*t17*t4+70*t38*t
#14*t53-311*t285*t34-3*t78*t176*t4+6*t288*t64-2*t176*t14*t15-111*t7
#9*t43-411*t288*t34+10*t285*t64-36*t16*t26+4*t1*t53*t43*t38-82*t33*
#t57+85*t43*t73*t53+41*t68*t26*t17
t445 = t2+2*t4-t83
t446 = t445**2
t450 = 1/t9/t7/t6*(t94+t136+t192+t246+t299+t348+t394+t438)/t1/t446
#/t445
C0(I,I)=t450

100     CONTINUE

END

SUBROUTINE XJC(N,XJ,C)
```

```
IMPLICIT REAL*16 (A-Z)
INTEGER N,I
REAL*16 XJ(0:1142),C(0:1142),PI

PI=ASIN(1Q0)*2Q0

DO I=0,N

XJ(I)=COS(PI*I/N)
C(I)=1Q0

ENDDO

C(0)=2Q0
C(N)=2Q0

END

SUBROUTINE PRINTVECTOR(N,ARRAY)

IMPLICIT REAL*16 (A-Z)
INTEGER N,I
REAL*16 ARRAY(1142)

DO I=1,N
WRITE(*,*) ARRAY(I)
ENDDO

END

SUBROUTINE CREATD1(N,XJ,C,D1)

IMPLICIT REAL*16 (A-Z)
INTEGER N,I,J
REAL*16 XJ(0:1142),C(0:1142),D1(0:1142,0:1142)
REAL*16 PI

PI=ASIN(1Q0)*2Q0

DO J=0,N

DO I=0,N

IF(I.NE.J) THEN
D1(I,J)=C(I)*(-1Q0)**(I+J)/C(J)/(XJ(I)-XJ(J))
ELSE
```

```
IF((I.EQ.0Q0 ).AND.( J.EQ.0Q0)) THEN
D1(I,J)=(2Q0*N*N+1Q0)/6Q0
ELSE IF((I.EQ.N).AND.(J.EQ.N)) THEN
D1(I,J)=-(2Q0*N*N+1Q0)/6Q0
ELSE
D1(I,J)=-XJ(J)/2Q0/(1Q0-XJ(J)*XJ(J))
ENDIF

ENDIF

ENDDO

ENDDO

DO J=0,N

DO I=0,N
D1(I,J)=(4Q0/PI)*D1(I,J)
ENDDO

ENDDO

RETURN

END

SUBROUTINE MATRIXPRODUCT(N,DA,DB,DC)

IMPLICIT REAL*16 (A-Z)
INTEGER N,M,J,I
REAL*16 DA(0:1142,0:1142),DB(0:1142,0:1142)
REAL*16 DC(0:1142,0:1142),T

DO J=0,N

DO I=0,N

T=0Q0

DO M=0,N
T=T+DA(I,M)*DB(M,J)
ENDDO

DC(I,J)=T

ENDDO
```

```
ENDDO

END

SUBROUTINE MATRIXVECTORPRODUCT(N,DA,DB,DC)

IMPLICIT REAL*16 (A-Z)
INTEGER N,M,J,I
REAL*16 DA(0:1142,0:1142),DB(0:1142),DC(0:1142),T

DO J=0,N

DO I=0,N

T=0Q0

DO M=0,N
T=T+DA(I,M)*DB(M)
ENDDO

DC(I)=T

ENDDO

ENDDO

END

SUBROUTINE COEFFMATRIX(N,C0,A1,A2,A3,A4,A)

IMPLICIT REAL*16 (A-Z)
REAL*16 C0(0:1142,0:1142)
REAL*16 A1(0:1142,0:1142),A2(0:1142,0:1142)
REAL*16 A3(0:1142,0:1142),A4(0:1142,0:1142)
REAL*16 A(0:1142,0:1142)
INTEGER N,I,J

DO I=0,N

DO J=0,N
A(I,J)=C0(I,J)+A1(I,J)+A2(I,J)+A3(I,J)+A4(I,J)
ENDDO

ENDDO
```

```
END

SUBROUTINE IMPOSEBOUNDARYCONDITION(N,A,D1,D2,D3,AM)

IMPLICIT REAL*16 (A-Z)
REAL*16 A(0:1142,0:1142),AM(1142,1142)
REAL*16 D1(0:1142,0:1142),D2(0:1142,0:1142)
REAL*16 D3(0:1142,0:1142)
INTEGER N,I,J
REAL*16 F1,F2,F3,S1,S2,T1

F1=(D1(0,0)-D1(N,0))+(D1(0,N)-D1(N,N))
F2=(D2(0,0)-D2(N,0))+(D2(0,N)-D2(N,N))
F3=(D3(0,0)-D3(N,0))+(D3(0,N)-D3(N,N))


S1=(D2(0,1)-D2(N,1))*F1/F2-(D1(0,1)-D1(N,1))
S2=(D3(0,1)-D3(N,1))*F1/F3-(D1(0,1)-D1(N,1))

T1=((D3(0,N-1)-D3(N,N-1))*F1/F3-(D1(0,N-1)-D1(N,N-1)))*S1/S2-
#((D2(0,N-1)-D2(N,N-1))*F1/F2-(D1(0,N-1)-D1(N,N-1)))

DO I=0,N
A(I,0)=A(I,0)+A(I,N)
ENDDO

DO I=1,N-1

DO J=1,N-1
A(I,J)=A(I,J)+A(I,0)/(-F1)*(D1(0,J)-D1(N,J))
ENDDO

ENDDO

DO I=2,N-1

DO J=2,N-1
A(I,J)=A(I,J)+A(I,1)/(-S1)*((D2(0,J)-D2(N,J))*F1/F2
#-(D1(0,J)-D1(N,J)))
ENDDO

ENDDO

DO I=2,N-2
DO J=2,N-2
A(I,J)=A(I,J)+A(I,N-1)/(-T1)*(((D3(0,J)-D3(N,J))*F1/F3
```

```
#-(D1(0,J)-D1(N,J)))*S1/S2-((D2(0,J)-D2(N,J))
#*F1/F2-(D1(0,J)-D1(N,J))))
ENDDO

ENDDO

DO I=1,N-3

DO J=1,N-3
AM(I,J)=-A(I+1,J+1)
ENDDO

ENDDO

END

REAL*16 FUNCTION F2(X)

IMPLICIT REAL*16 (A-Z)
REAL*16 X,FUN,M,EPS,PI
INTEGER I,IST,IED

PI=ASIN(1Q0)*2Q0
FUN=0Q0
IST=-12Q0
IED=14Q0
EPS=0.05Q0

DO 1 I=IST,IED

M=(X+I*PI/2Q0)/EPS

IF(M.LE.0Q0) THEN
FUN=FUN+2Q0*EXP(M)/(EXP(2Q0*M)+1Q0)
ELSE
FUN=FUN+2Q0*EXP(-M)/(EXP(-2Q0*M)+1Q0)
ENDIF

1 CONTINUE

FUN=FUN*COS(X)
F2=FUN

RETURN

END
```

```
REAL*16 FUNCTION F3(X)

IMPLICIT REAL*16 (A-Z)
REAL*16 X,FUN,M,PI,EPS
INTEGER IST,IED,I

PI=ASIN(1Q0)*2Q0
FUN=0Q0
IST=-12Q0
IED=14Q0
EPS=0.05Q0

DO 1 I=IST,IED

M=(X+(I-0.5Q0)*PI/2Q0)/EPS

IF(M.LE.0Q0) THEN
FUN=FUN+2Q0*EXP(M)/(EXP(2Q0*M)+1Q0)
ELSE
FUN=FUN+2Q0*EXP(-M)/(EXP(-2Q0*M)+1Q0)
ENDIF

1    CONTINUE

F3=FUN

RETURN

END

REAL*16 FUNCTION DF3(X)

IMPLICIT REAL*16 (A-Z)
REAL*16 X,FUN,M,PI,EPS
INTEGER IST,IED,I

PI=ASIN(1Q0)*2Q0
FUN=0Q0
IST=-12Q0
IED=14Q0
EPS=0.05Q0

DO 1 I=IST,IED
M=(X+(I-0.5Q0)*PI/2Q0)/EPS
```

```
IF(M.LE.0Q0) THEN
FUN=FUN+2Q0*EXP(M)*(EXP(2Q0*M)-1Q0)
#/(EXP(2Q0*M)+1Q0)**2
ELSE
FUN=FUN+2Q0*EXP(-M)*(1Q0-EXP(-2Q0*M))
#/(EXP(-2Q0*M)+1Q0)**2
ENDIF

1      CONTINUE

DF3=FUN*(-1.0Q0/EPS)

RETURN

END

SUBROUTINE COTES(A,B,F,N,T)

IMPLICIT REAL*16 (A-Z)
REAL*16  A,B,F,T,H,TEMP1,TEMP2,TEMP3,TEMP4
REAL*16 X1,X2,X3,X4
INTEGER N,I

H=(B-A)/N
TEMP1=0Q0
TEMP2=0Q0
TEMP3=0Q0
TEMP4=0Q0

DO I=0,N-1

X1=A+(I+0.25Q0)*H
X2=A+(I+0.5Q0)*H
X3=A+(I+0.75Q0)*H
TEMP1=TEMP1+F(X1)
TEMP2=TEMP2+F(X2)
TEMP3=TEMP3+F(X3)

ENDDO

DO I=1,N-1

X4=A+I*H
TEMP4=TEMP4+F(X4)
ENDDO
```

```
T=H/90Q0*(7Q0*F(A)+32Q0*TEMP1+12Q0*TEMP2+32Q0*TEMP3
#+14Q0*TEMP4+7Q0*F(B))

RETURN

END

REAL*16 FUNCTION DDF3(X)

IMPLICIT REAL*16 (A-Z)
REAL*16 X,FUN,M,PI,EPS
INTEGER IST,IED,I

PI=ASIN(1Q0)*2Q0
FUN=0Q0
IST=-12Q0
IED=14Q0
EPS=0.05Q0

DO 1 I=IST,IED

M=(X+(I-0.5Q0)*PI/2Q0)/EPS

IF(M.LE.0Q0) THEN

FUN=FUN-4Q0*EXP(M)*(EXP(2Q0*M)-1Q0)**2
#/(EXP(2Q0*M)+1Q0)**3+2Q0*EXP(M)/(1+EXP(2Q0*M))

ELSE
FUN=FUN-4Q0*EXP(-M)*(EXP(-2Q0*M)-1Q0)**2
#/(EXP(-2Q0*M)+1Q0)**3+2Q0*EXP(-M)/(1+EXP(-2Q0*M))

ENDIF

1      CONTINUE

DDF3=FUN*(-1Q0/EPS**2Q0)

RETURN

END

SUBROUTINE CALCULATEDIFF(N,L,R,RE,S,PHH,D1RE,D2RE,D3RE,D4RE)
          IMPLICIT REAL*16 (A-Z)
INTEGER N,I
REAL*16 RE(0:1142),S(0:1142),PHH(0:1142)
```

```
REAL*16 D1RE(0:1142),D2RE(0:1142)
REAL*16 D3RE(0:1142),D4RE(0:1142)
REAL*16 L,R,xt,yt,ph,Dfph,DDfph
REAL*16 F3,DF3,DDF3

DO 10 I=0,N

xt=RE(I)*COS(S(I))
yt=RE(I)*SIN(S(I))
ph=PHH(I)
ft=R+L*F3(ph)
Dfph=L*DF3(ph)
DDfph=L*DDF3(ph)
t44 = sin(ph)
t46 = cos(ph)
t49 = xt**2
t50 = yt**2
t52 = sqrt(t49+t50)
t59 = -(xt*t44-yt*t46)*t52/(t46*xt+yt*t44)
D1RE(I)=t59

t44 = xt**2
t45 = yt**2
t47 = sqrt(t44+t45)
t48 = t47**2
t49 = t48*t47
t50 = cos(ph)
t52 = sin(ph)
t54 = t50*xt+yt*t52
t55 = t54**2
t56 = 1/t55
t58 = 1/ft
t65 = (xt*t52-yt*t50)**2
t73 = t49*t56-t49*t58/t54+t65*t47*t56-t65*t49/t55/t54*t58

D2RE(I)=t73

 t44 = xt**2
 t45 = yt**2
 t47 = sqrt(t44+t45)
 t48 = t47**2
 t49 = t48*t47
 t50 = cos(ph)
 t51 = t50*xt
t52 = sin(ph)
t53 = yt*t52
```

```
t54 = t51+t53
t55 = t54**2
t57 = 1/t55/t54
t61 = -xt*t52+yt*t50
t64 = t48**2
t65 = t64*t47
t66 = t65*t61
t67 = t55**2
t68 = 1/t67
t69 = 1/ft
t70 = t68*t69
t74 = 1/t55
t79 = ft**2
t81 = 1/t79/ft
t84 = 1/t79
t88 = -ft+t51+t53
t93 = t61**2
t94 = t93*t61
t114 = 3*t49*t57*t61-2*t66*t70-3*t49*t69*t74*t61+t65*Dfph*t81*t74+
#t66*t84*t57-2*t61*t49*t88*t57*t69+t94*t47*t57-5*t94*t49*t70+2*t66*
#t88*t68*t84+3*t94*t65/t67/t54*t84+t93*t65*Dfph*t68*t81
D3RE(I)=t114

t44 = sin(ph)
t45 = xt*t44
t46 = cos(ph)
t47 = yt*t46
t48 = t45-t47
t49 = t48**2
t50 = t49**2
t51 = xt**2
t52 = yt**2
t53 = t51+t52
t54 = sqrt(t53)
t56 = t46*xt
t57 = yt*t44
t58 = t56+t57
t59 = t58**2
t60 = t59**2
t61 = 1/t60
t64 = t54**2
t65 = t64*t54
t66 = t65*t49
t69 = -ft+t56+t57
t70 = t65*t69
t72 = 1/t59/t58
```

```
t75 = t49*t54
t76 = 1/t59
t79 = t48*t65
t81 = ft**2
t82 = 1/t81
t87 = t64**2
t88 = t87*t54
t89 = t48*t88
t90 = Dfph+t45-t47
t95 = t88*t69
t98 = 1/ft
t99 = t72*t98
t116 = 1/t60/t58
t117 = t98*t116
t120 = t69**2
t125 = t61*t82
t132 = Dfph**2
t134 = t81**2
t135 = 1/t134
t139 = -18*t50*t54*t61-19*t66*t61-3*t70*t72-9*t75*t76-2*t79*t69*Df
#ph*t82*t72+2*t89*t90*t61*t82-t95*t82*t72+11*t66*t99-15*t50*t88/t60
#/t59*t82-9*t75*t69*t72+9*t75*ft*t72+35*t50*t65*t117+2*t120*t65*t99
#-2*t120*t88*t125+t50*ft/t54*t72-3*t88*t132*t135*t76
t142 = 1/t81/ft
t145 = t88*t49
t154 = t49*t48
t156 = Dfph*t61
t157 = t156*t82
t201 = t88*DDfph*t142*t76+8*t145*t117+2*t95*t61*t98+3*t70*t98*t76-
#10*t154*t65*t157+6*t89*t69*t156*t142-8*t65*Dfph*t82*t48*t76+t145*D
#Dfph*t61*t142+4*t89*Dfph*t142*t72-2*t89*t157-17*t145*t69*t116*t82+
#31*t66*t69*t61*t98-3*t145*t125-3*t145*t132*t61*t135+10*t154*t88*Df
#ph*t116*t142-2*t79*t90*t72*t98
t210 = (t139+t201)*t53/(ft*t46*xt+yt*ft*t44)
D4RE(I)=t210

10 CONTINUE

END

SUBROUTINE PRINTTOFILE(UNIT,FILENAME,N,ARRAY1,ARRAY2)

IMPLICIT REAL*16 (A-Z)
REAL*16 ARRAY1(0:1142),ARRAY2(1142)
INTEGER N,UNIT
CHARACTER*8 FILENAME
```

```
OPEN(UNIT,FILE=FILENAME,STATUS='UNKNOWN')

DO I=1,N
WRITE(UNIT,6000) ARRAY1(I+1)*360D0/2D0/3.1415926D0,ARRAY2(I)
6000      FORMAT(3X,F20.8,1X,F20.8)
ENDDO

CLOSE(UNIT)

END
```

F5. Program for molecular dynamic simulation of nanowires

```
program main

implicit double precision (a-z)
external pot,kin,force
double precision x(0:7200,0:1),y(0:7200,0:1),z(0:7200,0:1)
double precision e,s,m(0:7200),dt
double precision xa(0:20,0:20,0:60)
double precision ya(0:20,0:20,0:60)
double precision za(0:20,0:20,0:60)
double precision sitax(0:7200),sitay(0:7200),r(0:7200)
double precision fx(0:7200,0:1),fy(0:7200,0:1),fz(0:7200,0:1)
double precision vx(0:7200,0:1),vy(0:7200,0:1),vz(0:7200,0:1)
double precision tem,en,ki,po
double precision upx,upy,lowx,lowy,upz,lowz
integer n,qcut,num,num2,num3,i,j,k,q,nx,ny,nz,zi
integer count,itemp,jtemp
double precision Pi
double precision x01,x02,y01,y02,z01,z02,xtot,ytot,ztot
double precision fxt,fyt,fzt
character(10) filename(1:20)
integer nfile,nfilei

filename(1)="1.dat"
filename(2)="2.dat"
filename(3)="3.dat"
filename(4)="4.dat"
filename(5)="5.dat"
filename(6)="6.dat"
filename(7)="7.dat"
filename(8)="8.dat"
filename(9)="9.dat"
filename(10)="10.dat"
filename(11)="11.dat"
filename(12)="12.dat"
filename(13)="13.dat"
filename(14)="14.dat"
filename(15)="15.dat"
filename(16)="16.dat"
filename(17)="17.dat"
filename(18)="18.dat"
filename(19)="19.dat"
filename(20)="20.dat"

nfile=20

open(22,file='energy.dat',status='unknown')
```

```
open(31,file='kinetic.dat',status='unknown')
open(32,file='potential.dat',status='unknown')
open(24,file='position1.dat',status='unknown')
open(25,file='position2.dat',status='unknown')
open(28,file='posin.dat',status='unknown')
open(29,file='posend.dat',status='unknown')
open(26,file='velocity1.dat',status='unknown')
open(27,file='velocity2.dat',status='unknown')
open(30,file='temperature.dat',status='unknown')
open(33,file='posinwhole.dat',status='unknown')
open(34,file='posendwhole.dat',status='unknown')
open(35,file='result.dat',status='unknown')

Pi=2d0*dasin(1d0)
e=1d0
s=1d0
nfilei=1
t=24000d0
dt=0.01d0
n=t/dt
qcut=23900d0/dt
ti=0.32d0
tscale=0.32d0
tw=0.32d0

lattice=2d0**(1d0/6d0)
dx=lattice
dy=lattice*sin(Pi/3d0)
dz=sqrt(6d0)/3d0*lattice
nx=3
nz=30
upx=6d0*dx
lowx=-6d0*dx
upy=6d0*dx
lowy=-6d0*dx
upz=nz/2d0*dz
lowz=-nz/2d0*dz

count=0

do k=0,nz-1
do j=0,2*nx-2

if(j.le.nx-1) then
itemp=nx-1+j
jtemp=j
```

```
else
itemp=2*nx-2-(j-(nx-1))
jtemp=(nx-1)-(j-(nx-1))
endif

do i=0,itemp
xa(i,j,k)=i*dx-jtemp*dx/2d0
if(mod(k,2).eq.0) then
ya(i,j,k)=j*dy
else
ya(i,j,k)=j*dy+dy/2d0
endif

za(i,j,k)=k*dz

x(count,0)=xa(i,j,k)
y(count,0)=ya(i,j,k)
z(count,0)=za(i,j,k)

count=count+1

enddo
enddo
enddo

num=count-1
num2=2*num+1
num3=3*num+2

xtot=0d0
ytot=0d0
ztot=0d0

do k=0,num

xtot=x(k,0)+xtot
ytot=y(k,0)+ytot
ztot=z(k,0)+ztot

enddo

x01=xtot/(num+1)
y01=ytot/(num+1)
z01=ztot/(num+1)

do k=0,num
```

```
x(k,0)=x(k,0)-x01
y(k,0)=y(k,0)-y01
z(k,0)=z(k,0)-z01

enddo

@@@@@@@@@@@@@@@@@@@@@@@@@@@@@@@@@@@@
c     set original velocities

vxtot=0d0
vytot=0d0
vztot=0d0

do 100 k=0,num

m(k)=1d0
vx(k,0)=sqrt(ti)*(2d0*rand()-1d0)
vy(k,0)=sqrt(ti)*(2d0*rand()-1d0)
vz(k,0)=sqrt(ti)*(2d0*rand()-1d0)

vxtot=vxtot+vx(k,0)
vytot=vytot+vy(k,0)
vztot=vztot+vz(k,0)

100     continue

vxaver=vxtot/(1+num)
vyaver=vytot/(1+num)
vzaver=vztot/(1+num)

do k=0,num

vx(k,0)=vx(k,0)-vxaver
vy(k,0)=vy(k,0)-vyaver
vz(k,0)=vz(k,0)-vzaver

enddo

ki=kin(vx,vy,vz,num,0)
tactual=2d0/3d0*ki/(num+1)
ratio=sqrt(tscale/tactual)

do k=0,num

vx(k,0)=vx(k,0)*ratio
```

```
vy(k,0)=vy(k,0)*ratio
vz(k,0)=vz(k,0)*ratio

enddo

c@@@@@@@@@@@@@@@@@@@@@@@@@@@@@@@@@@@@

do k=num+1,num2

x(k,0)=x(k-num-1,0)
y(k,0)=y(k-num-1,0)
z(k,0)=z(k-num-1,0)-(upz-lowz)
vx(k,0)=vx(k-num-1,0)
vy(k,0)=vy(k-num-1,0)
vz(k,0)=vz(k-num-1,0)

enddo

do k=num2+1,num3

x(k,0)=x(k-num2-1,0)
y(k,0)=y(k-num2-1,0)
z(k,0)=z(k-num2-1,0)+(upz-lowz)
vx(k,0)=vx(k-num2-1,0)
vy(k,0)=vy(k-num2-1,0)
vz(k,0)=vz(k-num2-1,0)

enddo

do k=0,num
write(28,1000) x(k,0),y(k,0),z(k,0)
enddo

do k=0,num3
write(33,1000) x(k,0),y(k,0),z(k,0)
enddo

i=0
ttot=0d0

ki=kin(vx,vy,vz,num,0)
po=pot(x,y,z,num,0)
en=ki+po
tem=2d0/3d0*ki/(num+1)
ttot=tem+ttot
```

```
do 10 q=0,n-1

qfile=n/nfile*nfilei
 i=0

do 20 k=0,num

call force(k,x,y,z,num3,i,fxt,fyt,fzt)

fx(k,i)=fxt
fy(k,i)=fyt
fz(k,i)=fzt
x(k,i+1)=x(k,i)+dt*vx(k,i)+1d0/2d0*dt**2d0*fx(k,i)/m(k)
y(k,i+1)=y(k,i)+dt*vy(k,i)+1d0/2d0*dt**2d0*fy(k,i)/m(k)
z(k,i+1)=z(k,i)+dt*vz(k,i)+1d0/2d0*dt**2d0*fz(k,i)/m(k)

20    continue

do k=num+1,num2

x(k,i+1)=x(k-num-1,i+1)
y(k,i+1)=y(k-num-1,i+1)
z(k,i+1)=z(k-num-1,i+1)-(upz-lowz)

enddo

do k=num2+1,num3

x(k,i+1)=x(k-num2-1,i+1)
y(k,i+1)=y(k-num2-1,i+1)
z(k,i+1)=z(k-num2-1,i+1)+(upz-lowz)

enddo

xtot=0d0
ytot=0d0
ztot=0d0

do k=0,num

xtot=x(k,i+1)+xtot
ytot=y(k,i+1)+ytot
ztot=z(k,i+1)+ztot

enddo
```

```
vxtot=0d0
vytot=0d0
vztot=0d0

do 120 k=0,num

call force(k,x,y,z,num3,i+1,fxt,fyt,fzt)

fx(k,i+1)=fxt
fy(k,i+1)=fyt
fz(k,i+1)=fzt

vx(k,i+1)=vx(k,i)+1d0/2d0*dt*(fx(k,i)+fx(k,i+1))/m(k)
vy(k,i+1)=vy(k,i)+1d0/2d0*dt*(fy(k,i)+fy(k,i+1))/m(k)
vz(k,i+1)=vz(k,i)+1d0/2d0*dt*(fz(k,i)+fz(k,i+1))/m(k)

vxtot=vx(k,i+1)+vxtot
vytot=vy(k,i+1)+vytot
vztot=vz(k,i+1)+vztot

120    continue

xaver=vxtot/(1+num)
vyaver=vytot/(1+num)
vzaver=vztot/(1+num)

do k=0,num

vx(k,i+1)=vx(k,i+1)-vxaver
vy(k,i+1)=vy(k,i+1)-vyaver
vz(k,i+1)=vz(k,i+1)-vzaver

enddo

ki=kin(vx,vy,vz,num,i+1)
tactual=2d0/3d0*ki/(num+1)
ratio=sqrt(tscale/tactual)

if(mod(q,10).eq.0) then

do k=0,num

vx(k,i+1)=vx(k,i+1)*ratio
vy(k,i+1)=vy(k,i+1)*ratio
vz(k,i+1)=vz(k,i+1)*ratio
```

```
enddo

else

endif

do k=0,num

if(x(k,i+1).ge.upx) then

x(k,i+1)=2d0*upx-x(k,i+1)
vx(k,i+1)=-vx(k,i+1)

ki1=1d0/2d0*(vx(k,i+1)**2d0+vy(k,i+1)**2d0+vz(k,i+1)**2d0)
ki2=3d0/2d0*tw

ratio=sqrt(ki2/ki1)
vx(k,i+1)=vx(k,i+1)*ratio
vy(k,i+1)=vy(k,i+1)*ratio
vz(k,i+1)=vz(k,i+1)*ratio

elseif(x(k,i+1).le.lowx) then

x(k,i+1)=2d0*lowx-x(k,i+1)
vx(k,i+1)=-vx(k,i+1)

ki1=1d0/2d0*(vx(k,i+1)**2d0+vy(k,i+1)**2d0+vz(k,i+1)**2d0)
ki2=3d0/2d0*tw

ratio=sqrt(ki2/ki1)
vx(k,i+1)=vx(k,i+1)*ratio
vy(k,i+1)=vy(k,i+1)*ratio
vz(k,i+1)=vz(k,i+1)*ratio

else
endif

if(y(k,i+1).ge.upy) then

y(k,i+1)=2d0*upy-y(k,i+1)
vy(k,i+1)=-vy(k,i+1)

ki1=1d0/2d0*(vx(k,i+1)**2d0+vy(k,i+1)**2d0+vz(k,i+1)**2d0)
ki2=3d0/2d0*tw
ratio=sqrt(ki2/ki1)
```

```
vx(k,i+1)=vx(k,i+1)*ratio
vy(k,i+1)=vy(k,i+1)*ratio
vz(k,i+1)=vz(k,i+1)*ratio

elseif(y(k,i+1).le.lowy) then

y(k,i+1)=2d0*lowy-y(k,i+1)
vy(k,i+1)=-vy(k,i+1)

ki1=1d0/2d0*(vx(k,i+1)**2d0+vy(k,i+1)**2d0+vz(k,i+1)**2d0)
ki2=3d0/2d0*tw

ratio=sqrt(ki2/ki1)

vx(k,i+1)=vx(k,i+1)*ratio
vy(k,i+1)=vy(k,i+1)*ratio
vz(k,i+1)=vz(k,i+1)*ratio

else

endif

if(z(k,i+1).ge.upz) then

z(k,i+1)=z(k,i+1)-(upz-lowz)

elseif(z(k,i+1).le.lowz) then

z(k,i+1)=z(k,i+1)+(upz-lowz)

else

endif
enddo

do k=num+1,num2

x(k,i+1)=x(k-num-1,i+1)
y(k,i+1)=y(k-num-1,i+1)
z(k,i+1)=z(k-num-1,i+1)-(upz-lowz)
vx(k,i+1)=vx(k-num-1,i+1)
vy(k,i+1)=vy(k-num-1,i+1)
vz(k,i+1)=vz(k-num-1,i+1)

enddo
```

```
do k=num2+1,num3

x(k,i+1)=x(k-num2-1,i+1)
y(k,i+1)=y(k-num2-1,i+1)
z(k,i+1)=z(k-num2-1,i+1)+(upz-lowz)
vx(k,i+1)=vx(k-num2-1,i+1)
vy(k,i+1)=vy(k-num2-1,i+1)
vz(k,i+1)=vz(k-num2-1,i+1)

enddo

f(q.le.qcut) then
ttot=0d0
else
endif

ki=kin(vx,vy,vz,num,i+1)
po=pot(x,y,z,num,i+1)
en=ki+po
tem=2d0/3d0*ki/(num+1)

ttot=tem+ttot

if(mod(q,200).eq.0) then
write(22,*) dt*q,en
write(30,*) dt*q,tem
write(31,*) dt*q,ki
write(32,*) dt*q,po
else
endif

if(q.eq.qfile) then

open(40+nfilei,file=filename(nfilei),status='unknown')

do k=0,num3

write(40+nfilei,1000) x(k,i+1),y(k,i+1),z(k,i+1),vx(k,i+1),vy(k,i+1),vz(k,i+1)

enddo

close(40+nfilei)
1000   format(1x,f26.16,2x,f26.16,2x,f26.16,2x,f26.16,2x,f26.16,2x,f26.16)

nfilei=nfilei+1
```

```
else

endif

if (q.eq.n-1) then

do k=0,num
write(29,1000) x(k,i+1),y(k,i+1),z(k,i+1)
enddo

do k=0,num3
write(34,1000) x(k,i+1),y(k,i+1),z(k,i+1)
enddo

else
endif

do k=0,num3

x(k,i)=x(k,i+1)
y(k,i)=y(k,i+1)
z(k,i)=z(k,i+1)

vx(k,i)=vx(k,i+1)
vy(k,i)=vy(k,i+1)
vz(k,i)=vz(k,i+1)

enddo

10 continue

tevar=ttot/(n-qcut)

close(25)
close(24)
close(22)
close(26)
close(27)
close(28)
close(29)
close(30)
close(35)

end
double precision function pot(x,y,z,num,tn)
```

```
implicit double precision (a-z)
double precision x(0:7200,0:1),y(0:7200,0:1),z(0:7200,0:1)
double precision e,s,r,po,potem
integer k,l,tn,num

e=1d0
s=1d0
po=0d0

do k=0,num
do l=k+1,num

r2=(x(k,tn)-x(l,tn))**2d0+(y(k,tn)-y(l,tn))**2d0+(z(k,tn)-z(l,tn))**2d0

if(r2.gt.25d0) then
potem=0d0
else
r=sqrt(r2)
potem=4d0*e*((s/r)**12d0-(s/r)**6d0
endif

po=potem+po

enddo
enddo

pot=po

end

double precision function kin(vx,vy,vz,num,tn)

implicit double precision (a-z)
double precision vx(0:7200,0:1),vy(0:7200,0:1),vz(0:7200,0:1)
double precision ki
integer k,tn,num

ki=0d0

do k=0,num
ki=1d0/2d0*(vx(k,tn)**2d0+vy(k,tn)**2d0+vz(k,tn)**2d0)+ki
enddo

kin=ki

end
```

```
subroutine force(k,x,y,z,num,tn,fxt,fyt,fzt)

implicit double precision (a-z)
double precision x(0:7200,0:1),y(0:7200,0:1),z(0:7200,0:1)
double precision fxt,fyt,fzt
integer num,tn,k,l

e=1d0
s=1d0

fxt=0d0
fyt=0d0
fzt=0d0

do 30 l=0,num

if(k.eq.l) goto 30

r2=(x(k,tn)-x(l,tn))**2d0+(y(k,tn)-y(l,tn))**2d0+(z(k,tn)-z(l,tn))**2d0

if(r2.gt.25d0) then
fxtt=0d0
fytt=0d0
fztt=0d0
else
r=sqrt(r2)
f=24d0*e/r*(2d0*(s/r)**12d0-(s/r)**6d0)
fxtt=(x(k,tn)-x(l,tn))/r*f
fytt=(y(k,tn)-y(l,tn))/r*f
fztt=(z(k,tn)-z(l,tn))/r*f
endif

fxt=fxtt+fxt
fyt=fytt+fyt
fzt=fztt+fzt

30      continue

end
```

VITA

The author, Wanxi Kan, was born in February, 1975, in Hubei, People's Republic of China. He graduated from high school of Xianning in July 1993.

In September 1993, the author attended University of Science and Technology Beijing (USTB) with a major in mechanical engineering. He obtained a bachelor of engineering degree in mechanical engineering in July 1997. He continued his graduate study in USTB, and obtained his master of science degree in mechanical engineering in March 2000.

The author continued his further graduate study in the Department of Mechanical Engineering, Louisiana State University since August, 2000, and in December of 2004, the degree of Doctor of Philosophy in engineering science will be conferred